

DISLOCATION MOBILITY AND DENSITY
IN ZINC SINGLE CRYSTALS

Thesis by
Kenneth Hoyt Adams

In Partial Fulfillment of the Requirements
For the Degree of
Doctor of Philosophy

California Institute of Technology
Pasadena, California

1965

(Submitted May 21, 1965)

TABLE OF CONTENTS

<u>PART</u>	<u>TITLE</u>	<u>PAGE</u>
	ACKNOWLEDGEMENTS	
	ABSTRACT	
	LIST OF TABLES	
	LIST OF FIGURES	
I.	INTRODUCTION	1
II.	ETCHING OF ZINC TO REVEAL DISLOCATIONS	14
III.	MATERIAL AND TEST SPECIMEN PREPARATION	22
IV.	EQUIPMENT AND TEST PROCEDURES	29
	Static Test Fixture	29
	Dynamic Test Fixture	36
	Pulse Tests	49
V.	EXPERIMENTAL RESULTS	63
	Static Tests	63
	A. Basal Slip System	63
	B. Nonbasal Slip System	66
	Dynamic Tests	68
	A. Basal Slip System	68
	Pulse Tests	78
	A. Basal Slip System	78
	B. Nonbasal Slip System	85
	Strain-Rate Sensitivity of the Flow Stress	89
	A. Basal Slip System	89
	B. Nonbasal Slip System	95

<u>PART</u>	<u>TITLE</u>	<u>PAGE</u>
	Influence of Impurity and Strain on Dislocation Substructure	96
	Dislocation Pile-Ups	102
VI.	DISCUSSION OF RESULTS	107
	Basal Slip System	107
	A. Dislocation Orientations	107
	B. Dislocation Multiplication and Density Changes	110
	C. Thermally Activated Dislocation Motion	113
	D. Dislocation Mobility in Other Materials	116
	E. Lattice Resistance to Dislocation Motion	118
	F. Nature of Long-Range Internal Stresses	120
	G. Strain-Rate Sensitivity of the Flow Stress	127
	H. Stress-Strain Behavior	133
	Nonbasal Slip System	136
	A. Dislocation Orientations and Dislocation Multiplication	136
	B. Dislocation Mobility	140
	C. Strain-Rate Sensitivity of the Flow Stress	142
	Stress-Strain Behavior as Related to Dislocation Properties	143
VII.	SUMMARY AND CONCLUSIONS	144
	REFERENCES	150

ACKNOWLEDGEMENTS

The author wishes to express his thanks and appreciation to Professor T. Vreeland, Jr. for his continued interest and support during the course of this research. Appreciation is expressed to Professor D. S. Wood for many interesting discussions on the theoretical aspects of this research. Thanks are expressed to Mr. R. C. Blish and Mr. A. P. L. Turner for their assistance in specimen preparation and testing.

The author is indebted to the Ford Foundation, Kaiser Aluminum and Chemical Corporation and the Gillette-Paper Mate Company for fellowship grants. The testing program was conducted under a contract with the U. S. Atomic Energy Commission. Appreciation is extended to this agency for support of this work.

ABSTRACT

Experimental measurements of dislocation mobility and density, and the strain-rate sensitivity of the flow stress have been made on 99.999 per cent pure zinc crystals. Dislocation density and the strain-rate sensitivity of the flow stress were also measured on zone refined crystals and crystals containing 0.0025 and 0.02 wt per cent aluminum. Dislocation mobilities in the $\langle 11\bar{2}0 \rangle$ $\{0001\}$ (basal), and $\langle 1\bar{2}1\bar{3} \rangle$ $\{1\bar{2}12\}$ (nonbasal) slip systems were measured by observing slip band growth produced by load pulses of controlled amplitude and duration. The results of the experimental measurements of dislocation mobility are discussed in relation to current theories. A comparison of the strain-rate sensitivity and the mobility measurements shows that a significant change in the density of moving dislocations is associated with a change in strain-rate. This change in density has generally been ignored by previous investigators. A dislocation model is proposed to explain the observed strain-rate sensitivity.

Observations were also made of the change of substructure and in particular the change of nonbasal dislocation density accompanying impurity additions of aluminum to the zinc. The effect of the aluminum on the basal stress-strain behavior is explained in terms of changes in nonbasal dislocation density which determines

the separation distance of attractive and repulsive junctions between basal and nonbasal dislocations. The onset of basal slip is associated with the breaking of attractive junctions.

The change in basal dislocation density produced by plastic shear strain is shown to obey the relation $\Delta\rho = C \gamma_p^{\frac{1}{3}}$, and is independent of purity. A markedly different relation is indicated for the nonbasal dislocation density vs. strain. These results are explained by a significant difference in the average glide distance of dislocations in the basal and nonbasal slip systems.

LIST OF TABLES

<u>TABLE</u>	<u>TITLE</u>	<u>PAGE</u>
I	Resolved Shear Stress Uncertainty Resulting from Orientation Uncertainty	27
II	Summary of Tests	30
III	Dislocation Density Changes Produced by Plastic Strain	76
IV	Summary of Variable Strain-Rate Data	92
V	Summary of Effect of Purity on Substructure and Nonbasal Dislocation Density	101
VI	Summary of τ_0 and n for Various Materials	117

LIST OF FIGURES

<u>FIG. NO.</u>	<u>TITLE</u>	<u>PAGE</u>
1.	Several Crystallographic Planes and Directions in Zinc Crystals.	11
2.	Polar Stereographic Projection for Zinc Showing Crystallographic Dependence of Etch.	15
3.	Crystallographic Dependence of Etch.	16
4.	Etch Figures on Zinc Crystal Surface 10° to $[0001]$ and 80° to $[11\bar{2}0]$, 100X.	18
5.	Etched Zinc Surface near $[0001]$, 100X.	20
6.	Pyrex Mold, a Section of a Crystal and a 1/2 in. Cube Specimen Trepanned from a Section of the Crystal.	24
7.	Crystallographic Orientation of Test Specimens.	25
8.	Kink Damage from Spark Machining, 100X.	28
9.	Test Specimen and Parallel Capacitor Plates.	31
10.	Static Test Fixture.	34
11.	Schematic of Dynamic Test Fixture.	37
12.	Dynamic Test Fixture.	39
13.	Load Seats and Alignment Sleeve of Dynamic Test Fixture.	40
14.	Circuits Used in Dynamic System.	42
15.	General View of Test Equipment.	43
16.	Tracing of Oscillograph Record.	45
17.	Strain Gage Circuit.	48
18.	Dynamometer Strain Gage Circuit.	50
19.	Tracing of Rapid Load Records.	51

<u>FIG. NO.</u>	<u>TITLE</u>	<u>PAGE</u>
20.	Schematic of Compression Fixture for Rapid Load Machine.	52
21.	Specimen Alignment Equipment.	54
22.	Rapid Load Testing Fixture.	56
23.	Spherical Seats and Alignment Sleeve.	57
24.	Air Supply System for Bearings.	58
25.	Damage from Scratches and Cold Tool, 100X.	62
26.	Resolved Shear Stress vs. Resolved Shear Strain for Basal Slip. Specimen 17-1, Zone Refined Purity.	64
27.	Compressive Stress vs. Compressive Strain for Nonbasal Slip. Specimen 26-6T1, 99.999 Per Cent Purity.	67
28.	Dislocation Density Resulting from Compressive Strain of 900×10^{-6} in./in. along c-Axis. Specimen 26-1T1, 99.999 Per Cent Purity, 50X.	69
29.	Influence of Purity on Basal Stress-Strain Curves.	70
30.	Influence of Prior Strain on Basal Stress-Strain Curves.	72
31.	Dislocation Density Changes Resulting from Basal Shear Strain of 1 Per Cent. Specimen 22-1T2, Zn-0.0025Al Purity, 100X.	73
32.	Dislocation Density Resulting from Basal Shear Strain of 6.3 Per Cent. Specimen 16-1T3, 99.999 Per Cent Purity, 100X.	75
33.	Change in Dislocation Density vs. Shear Strain for Basal Slip.	77
34.	Basal Dislocations before and after a Pulse of 9.9 lb/in. ² . Specimen 17-3T3, Zone Refined Purity. 1 Min Pulse Duration, 100X.	79

<u>FIG. NO.</u>	<u>TITLE</u>	<u>PAGE</u>
35.	Basal Dislocations before and after a Pulse of 15.5 lb/in. ² . Specimen 17-4T1, Zone Refined Purity. 17×10^{-3} Sec Pulse Duration, 100X.	82
36.	Basal Dislocation Velocity vs. Resolved Shear Stress for 99.999 Per Cent Purity Zn Specimens.	84
37.	Basal Dislocation Velocity vs. $\tau - \tau_c$.	86
38.	Nonbasal Slip Bands Resulting from c-Axis Compressive Stress of 970 lb/in. ² . Specimen 16-4T6, 99.999 Per Cent Purity. 31.4 Sec Pulse Duration, 100X.	88
39.	Nonbasal Dislocation Velocity vs. Resolved Shear Stress for 99.999 Per Cent Purity Specimens.	90
40.	Schematic Load-Time Curve.	94
41.	Dislocation Substructure in Zn-0.02Al Specimens. Specimen 19-1, 100X.	97
42.	Impurity Segregation in Zn-0.02Al Specimens. Specimen 19-3, 25X.	99
43.	Dislocation Substructure and Impurity Segregation in Zn-0.0025Al Specimens. Specimen 22-1, 25X.	100
44.	Nonbasal Dislocation Density Revealed on the Basal Plane of a Zn-0.02Al Purity Specimen. Density = 2.1×10^5 cm ⁻² , 100X.	103
45.	Dislocation Substructure after 30 Per Cent Shear Strain and Anneal. Specimen 16-3, 99.999 Per Cent Purity, 100X.	104
46.	Effect of Stress Unloading on Basal Dislocation Pile-Ups. Shear Stress = 12.1 lb/in. ² . Specimen 18-1, 99.999 Per Cent Purity, 100X.	106
47.	Possible \bar{c} and \bar{a} Type Vectors.	123

<u>FIG. NO.</u>	<u>TITLE</u>	<u>PAGE</u>
48.	Variation in Shear Stress Along a Slip Plane.	130
49.	Cross-Slip Mechanism.	138
50.	First and Second Order Pyramid Planes.	139

I. INTRODUCTION

Since the advent of the theory of dislocations in the late 1930's, a great number of mechanical and physical properties of crystalline solids have been shown to be dependent on dislocations and their behavior. In recent years, dislocation theory and models based upon dislocation theory have been applied to such phenomena as plastic deformation, work-hardening, internal friction, creep and fracture. In general, there has been an abundance of theories or dislocation models covering almost all deformation processes and a conspicuous lack of good experiments to test the validity of the theoretical treatments. This lack of experimental evidence has been a result of the fact that the experimental tools required for the direct study of dislocations were not available more than ten years ago and also the critical experiments needed to verify some theories are sometimes tedious experiments to conduct. The purpose of this experimental investigation was an attempt to bridge the gap between the theoretical and experimental approaches and to shed some light on the critical subject of dislocation behavior as related to the plastic deformation and work-hardening of crystalline solids.

A well-known result of dislocation theory is that the plastic shear strain, γ_p , resulting from dislocation motion in a single slip system is given by

$$\gamma_p = Ab \quad (1)$$

where

A = slip plane area swept over by all moving dislocations/unit volume

b = magnitude of the Burgers vector of glide dislocations.

The plastic shear strain-rate is dependent on the average velocity of the moving dislocations, v , and is given by

$$\dot{\gamma}_p = \dot{A}b = Nbv \quad (2)$$

where N is the total length of moving dislocation per unit volume. If it is assumed that all the moving dislocation lines are straight and parallel, then

$$N = \rho_M$$

where

ρ_M = density of moving dislocations/unit area normal to the dislocation lines

and Eq. 2 can be written as

$$\dot{\gamma}_p = \rho_M b v. \quad (3)$$

The velocity of moving dislocations and the rate of generation of mobile dislocations govern the dynamic stress-strain behavior of a single crystal through Eq. 3. The density of moving dislocations will generally be less than the total dislocation density of the crystal. Work-hardening results from interactions which tend to impede dislocation motion or lower the number of mobile dislocations. Therefore the general subject of mobility of dislocations which involves the velocity of dislocations is of considerable importance as it relates to the dynamic properties of crystalline solids.

Equation 3 expresses the fundamental relation between a macroscopic quantity, $\dot{\gamma}_p$, and the microscopic dislocation properties, ρ_m and v . The relation is equally valid for all crystalline solids including ionic and semiconducting materials as well as metals. With suitable orientation factors, Eq. 3 also applies to polycrystalline material. If the number of moving dislocations and the velocity of dislocation motion are known for a given material as functions of stress, strain and temperature, the plastic stress-strain behavior of the material can be predicted under any conditions of temperature, rate of loading or strain-rate. Equations 1 and 3 then

comprise the "equations of state" for the material from which the creep, and static and dynamic stress-strain behavior of the material can be predicted. From an engineering standpoint, an understanding of the factors which control the density and velocity of moving dislocations is necessary before a rational design of materials to control their plastic deformation properties is possible.

The velocity at which a dislocation can move is limited due to the way its kinetic energy increases as the velocity approaches the speed of sound waves. For a moving screw dislocation, \bar{b} parallel to the dislocation line, the kinetic energy approaches infinity as the dislocation velocity approaches the speed of shear waves. The same result is true for an edge dislocation, \bar{b} perpendicular to the dislocation line, in zinc single crystals according to Teutonico (1)*. This result puts an upper bound on dislocation velocities equal to the shear wave speed. Other factors, however, may limit a dislocation to speeds far below the shear wave speed.

The subject of dislocation mobility at speeds below the shear wave speed has been approached theoretically in several ways. One way has been to consider the

*Numbers appearing in parentheses refer to references listed at the end of the thesis.

motion of a dislocation through a perfect lattice and consider the various ways that energy can be transferred from the moving dislocation to the lattice. Energy transferred to the lattice results in a drag stress on the dislocation which limits the velocity to a level where the applied stress equals the drag stress. Two sources of drag have been considered theoretically. Liebfried (2) has considered the interaction of phonons with a moving screw dislocation and Eshelby (3) has considered thermoelastic damping as a source of drag. Both treatments assume a linear dependence of dislocation velocity on applied stress or a viscous type of drag.

A second line of approach to the problem of dislocation mobility has been to consider various interactions between dislocations and point defects as being the primary obstacles to the moving dislocations. Models of this type are somewhat more realistic because crystalline solids are rarely perfect and most often contain high densities of dislocations and impurity atoms. Theoretical treatments of the interaction of dislocations with obstacles assume that the moving dislocations spend most of their time at the obstacle and move rapidly to another obstacle once the first one is overcome. The resulting dislocation velocity

depends on the rate at which obstacles are overcome which is usually considered to be a thermally activated process. The various obstacles to dislocation motion which have been considered theoretically include substitutional impurity atoms (4), the Peierls barrier (5) and forest dislocations (6). Impurity atoms act as obstacles when they are a different size than the solvent atoms of the lattice. The size difference produces an associated stress field which causes a resistance to the motion of nearby dislocations. The Peierls barrier to dislocation motion is a result of the change in dislocation energy with position as a dislocation moves one atom distance. Forest dislocations are dislocations which thread the slip plane of a glide dislocation and provide a resistance to motion because dislocation "jogs" are produced as the glide dislocation cuts through the forest dislocation. The jogs produced represent extra dislocation line energy which is provided by the applied stress with the aid of thermal energy. In general, all the proposed models which depend on thermally activated motion predict an exponential dependence of the dislocation velocity or strain-rate on the applied stress. The strain-rate dependence is related to the velocity by Eq. 3. From theoretical considerations the possible variables which

might influence dislocation mobility include temperature, forest dislocation density and point defect concentration where point defects include impurity atoms as well as vacancies.

Various experimental tools exist for the direct and indirect study of dislocation mobility. Experiments which have been used to deduce dislocation mobility indirectly in single crystals include internal friction measurements (7), instantaneous creep rates resulting from a rapidly applied stress (8), and strain-rate sensitivity of the flow stress (9). The first two types of experiments depend on dislocation models for an interpretation of the experimental results and both suffer from an uncertainty as to the number or density of moving dislocations taking part in the deformation process. In addition, internal friction models such as the one of Granato and Lucke (10) assume a linearized equation of dislocation motion where the damping force is linearly dependent on the applied stress. Such an a priori assumption may indeed be incorrect. Strain-rate sensitivity experiments can be used to determine the mobility relation if assumptions are made about the change in density of moving dislocations accompanying a strain-rate change and if the general form for the mobility relation is assumed.

In general, the indirect type of experiment is relatively easy to conduct and hence offers attractive possibilities for a study of dislocation mobility. However, the validity of the various assumptions and models used must ultimately be checked against direct experimental measurements. Many investigators have drawn conclusions from the results of strain-rate sensitivity experiments in which the assumptions made about the density of moving dislocations were not verified.

Various experimental tools are presently available for the direct study of dislocations. Dislocations have been observed directly with a field ion microscope. The technique is limited to materials with high melting points such as tungsten and uses small specimens in the form of needles. Transmission electron microscopy is a widely used technique for studying dislocations in materials with dislocation densities up to about 10^{12} cm^{-2} . The technique suffers from several disadvantages for experimental determinations of dislocation mobility. The primary disadvantages are the small specimen size which limits observable dislocation displacements, the fact that thin foil specimens are not always representative of the bulk material from which they were prepared and the inherent difficulty in accurately controlling the stress state applied to a

specimen in the microscope. The technique can be used to determine the Burgers vector of the observed dislocations. X-ray methods such as the Berg-Barrett technique can be used to study dislocations near the surface of bulk material. The technique is limited to material with dislocation densities less than about 10^5 cm^{-2} and offers the advantage that the Burgers vector of the dislocations can be established. A disadvantage of the Berg-Barrett technique is the relatively long X-ray film exposure times required.

Another method available for the study of dislocations involves etching by chemical, electrolytic or thermal means to reveal dislocation intersection sites on the specimen surface as etch pits. The etch pit technique is limited to those materials for which a specific technique has been developed since no one method has been found to work for all materials. In addition, a technique is usually good only for certain low index crystallographic planes of a crystal. Disadvantages of this general technique include limited resolution corresponding to densities of approximately 10^7 cm^{-2} and uncertainties as to the slip plane and character of the dislocations revealed as etch pits. However, the etch pit technique is particularly useful for studies on bulk material and can be used to follow

dislocation motion over relatively large distances for mobility studies. Chemical etch pit techniques have been used to study dislocation mobility in a number of materials. The basic technique involves scratching to introduce fresh or unpinned dislocations which is followed by the application of a constant stress pulse for a specific length of time. The etched specimen reveals how far the dislocations have moved during the duration of the test. The average dislocation velocity produced by the stress level of the test is calculated from the distance of motion and time of stress application. Experiments of this type have been performed on single crystal specimens of lithium fluoride (11), silicon-iron (12), germanium (13, 14), silicon (13), sodium chloride (15) and tungsten (16).

The purpose of this investigation was to determine through experimental means the validity of various theories of dislocation mobility. [A testing program on zinc single crystals was undertaken because the crystallography of the various slip systems is known and because zinc has only one system of easy slip.] The basal or easy slip system is shown in Fig. 1 along with the twinning system and the second order pyramidal system which is one of the nonbasal slip systems. Rosenbaum (17) has shown, from observations of slip

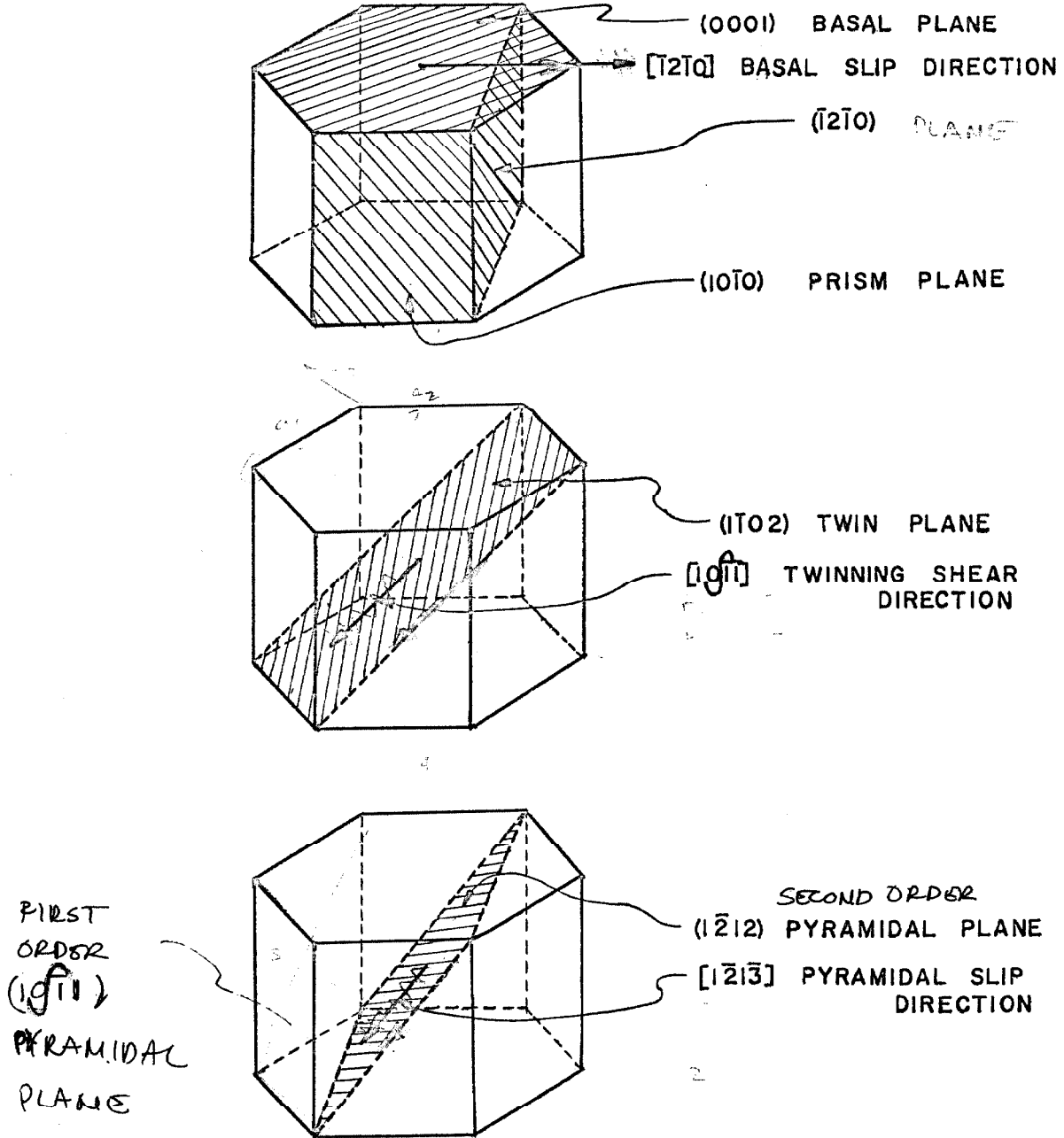


Fig. 1 Several Crystallographic Planes and Directions in Zinc Crystals.

line markings on crystals deformed at room temperature by nonbasal slip, that the $\langle 1\bar{2}1\bar{3} \rangle \{1\bar{2}12\}$ slip system is the nonbasal slip system which confirms the results of Bell and Cahn (18).

An experimental program involving the etch pit method for determining dislocation positions was chosen for the direct measurement of basal and nonbasal dislocation mobility in zinc single crystals. Previously reported etchants for zinc included one for cadmium-doped zinc crystals which requires an aging treatment to precipitate cadmium at dislocation sites (19) and one which reveals nonbasal dislocation intersections with the basal plane (20). Since neither etchant was suitable for a study of the mobility of basal dislocations in high purity material, a technique for revealing dislocation sites on prism planes (see Fig. 1) was developed as part of the experimental program. This technique has been reported elsewhere (21, 22). Additional observations on the etching procedure are included in Part II of this thesis.

Single crystals of several purities of zinc were grown and test specimens were prepared by techniques described in Part III. Purity was chosen as a variable in the direct study of dislocation mobility. Compression tests were conducted to determine the stress-strain

behavior for basal and nonbasal slip, compression pulse tests were conducted to determine dislocation mobility and compression tests were conducted at variable strain-rates to relate the strain-rate sensitivity of the flow stress to the direct mobility data. The orientation of the test specimens which varied between the tests on the basal and nonbasal slip system is described in Part III. The experimental methods used to determine dislocation mobility, stress-strain behavior and strain-rate sensitivity are described in Part IV.

The results of the testing program are presented in Part V along with observations on the dislocation density of deformed specimens and the effect of purity on dislocation density. In Part VI the experimental results are related to various theories of dislocation mobility, the fundamental mechanism governing the initiation of plastic flow and the process of work-hardening in zinc single crystals.

II. ETCHING OF ZINC TO REVEAL DISLOCATIONS

An etching procedure which reveals etch figures corresponding to dislocation intersections with $\{10\bar{1}0\}$ planes of zinc single crystals has been reported elsewhere by Brandt, Adams and Vreeland (21, 22). The etching procedure involves the introduction of a very small amount of mercury onto the surface of a zinc crystal by etching in a weak acid solution of mercuric nitrate. Subsequent polishing with a chromic acid solution results in the formation of etch figures or "etch pits"* at dislocation intersections with the crystal surface.

Additional observations have been made on the dependence of the etch on the crystallographic orientation of the specimen surface by etching a 2 in. diameter hemispherical crystal of 99.999 per cent purity. A new crystal surface orientation has been found where etch pits are revealed. The new surface orientation is located between 3° and 12.2° to the $[0001]$ and is axially symmetric about this axis. Figure 2 shows on a polar stereographic projection all the regions of good etching as well as those regions where the etched surface is of marginal and poor quality. Figure 3

*The figures will be referred to as "etch pits" although they actually are "etch pips" or hillocks.

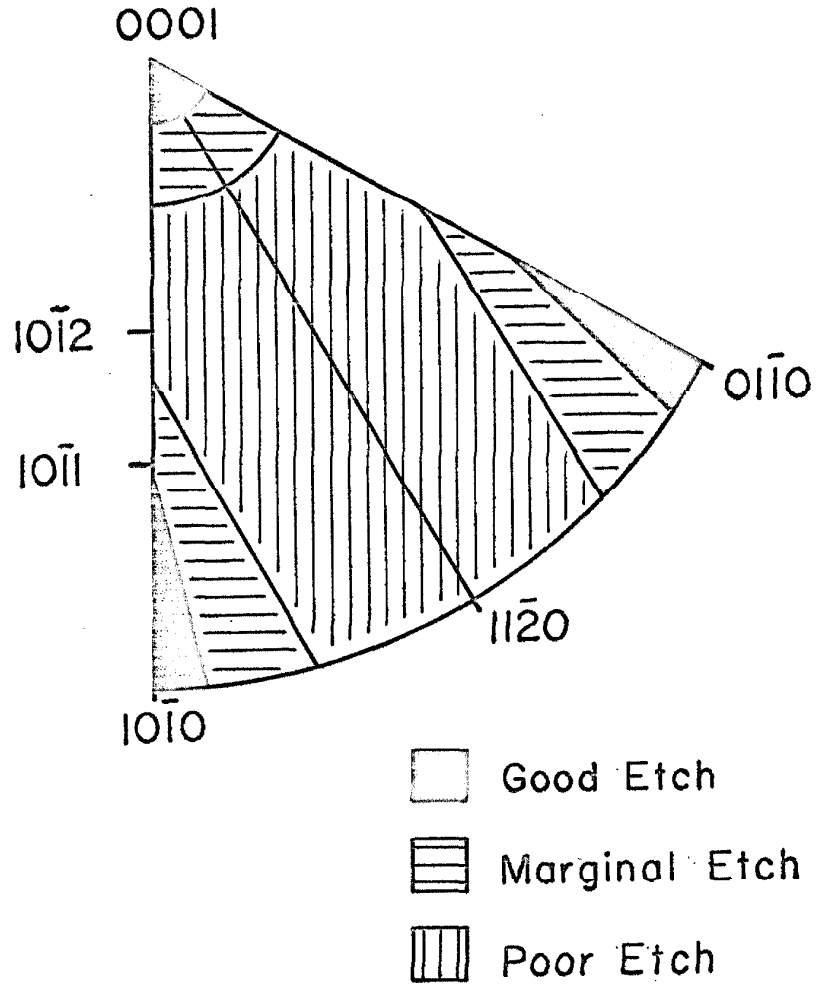


Fig. 2 Polar Stereographic Projection for Zinc Showing Crystallographic Dependence of Etch.

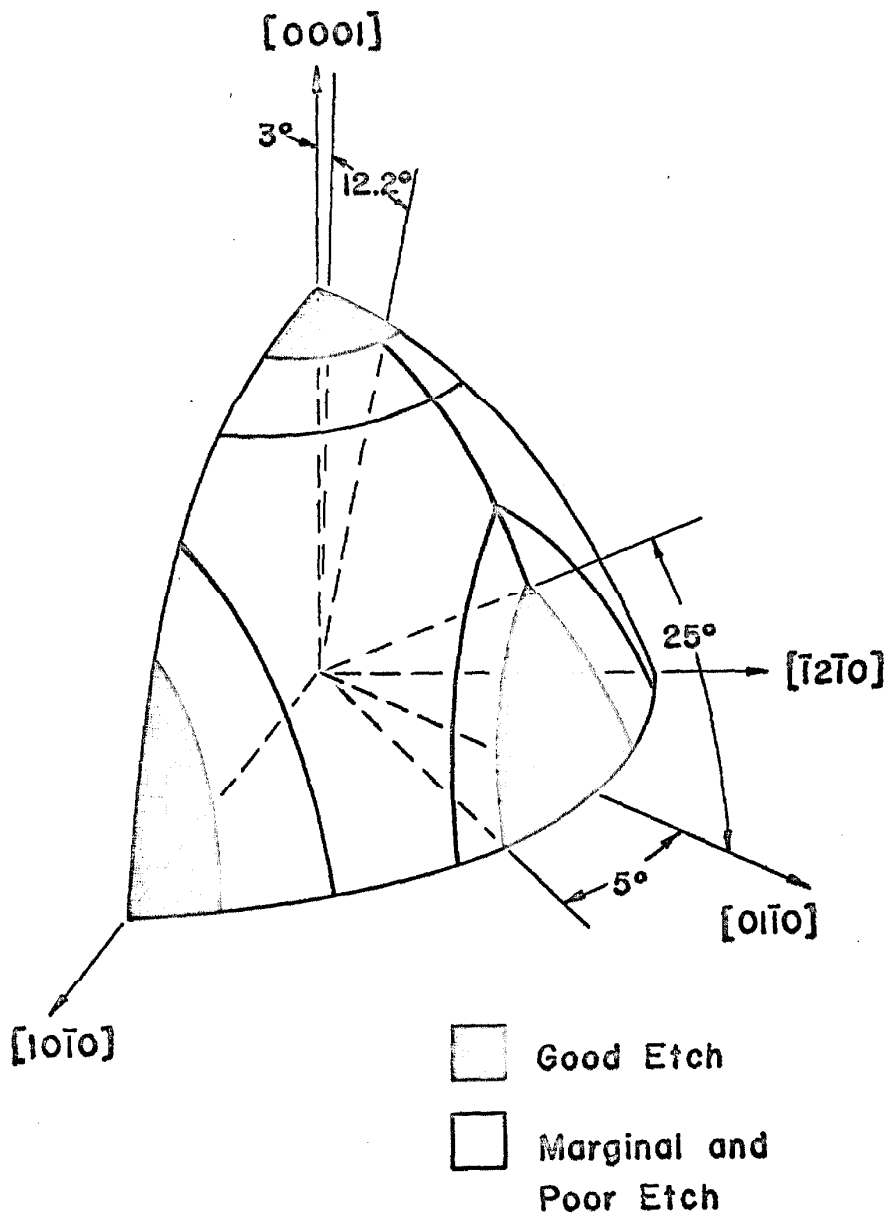
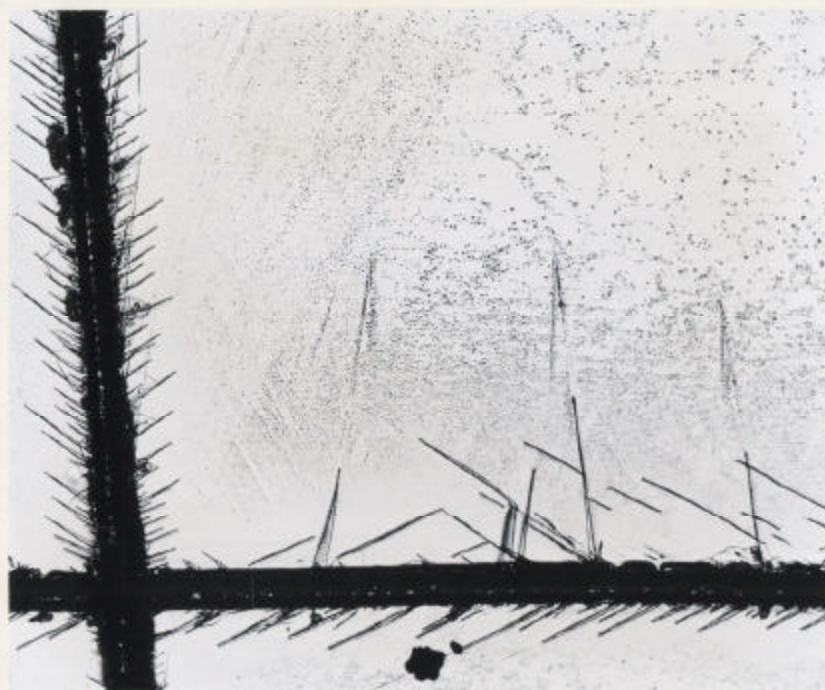


Fig. 3 Crystallographic Dependence of Etch.

shows the same regions on a perspective drawing. Attempts to etch the (0001) surface were generally unsuccessful although it was found that by using a much lower mercury concentration on freshly cleaved surfaces some etch pits were revealed that were obviously associated with twinning damage. A fresh surface was produced by quenching the specimen in methanol after cleaving in liquid nitrogen. No further attempts were made to etch (0001) planes because it is generally undesirable to subject large specimens to the thermal strains involved in the quenching process.

Figure 4 shows etch pits produced on a crystal surface whose normal is oriented 10° from the [0001] and 80° from the $[11\bar{2}0]$ axes as a result of heavy razor blade scratches. The arrows indicate the basal plane trace on this surface and etch pits can be seen lined-up in the general direction of the $\{1\bar{2}12\}$ second order pyramidal slip plane traces as indicated by the dashed lines. Nonbasal $\{1\bar{2}12\}$ type dislocations are therefore assumed to be revealed on planes within 3° to 12.2° to the [0001]. The dark lines emanating from the scratches in Fig. 4 are twins that were produced by the razor blade scratches.

Experiments were conducted to establish whether basal dislocations are revealed in the region between



|
Razor
Scratch

←→
Basal
Plane
Trace



{1 $\bar{2}$ 12} Traces

Fig. 4 Etch Figures on Zinc Crystal Surface 10° to $[0001]$ and 80° to $[11\bar{2}0]$, 100X.

3° and 12.2° to the $[0001]$. Several 1/2 in. cube compression specimens oriented for basal slip and containing a pair of surfaces oriented 10° to the $[0001]$ as well as a pair of $(10\bar{1}0)$ surfaces were etched, deformed and re-etched to reveal changes in the dislocation configuration. Basal deformation on 10° surfaces was not indicated even though extensive basal deformation was indicated on $(10\bar{1}0)$ surfaces. The general condition of the re-etched 10° surfaces was usually rather poor. Areas of general background pitting resulted which caused difficulty in determining whether changes in the dislocation density and configuration had actually occurred as a result of the basal deformation. An additional experiment was conducted on the 2 in. diameter hemispherical crystal previously mentioned. A 1/4 in. diameter flat area was exposed at the $[0001]$ pole by cleaving the crystal. A brass rod was glued to the surface with Eastman 910 adhesive. The crystal was held stationary while the rod was twisted 10° about the $[0001]$ thus causing basal slip. The etched specimen revealed pile-ups of dislocations along the circular basal plane traces near the $[0001]$ pole as shown in Fig. ^{III} 5. The exact orientation of the region showing dislocation pile-ups is not known. The observations lead to the conclusion that at least for some surface

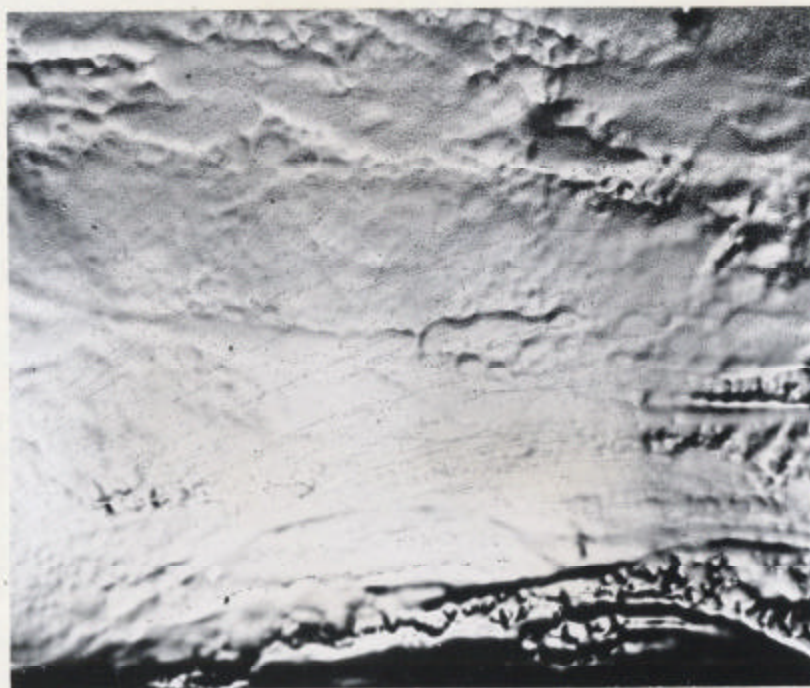


Fig. 5 Etched Zinc Surface near $[0001]$, 100X.

orientations near the $[0001]$ axis, basal dislocations can be revealed as etch figures. However, the quality of the re-etched surfaces was too poor to be useful for the study of dislocation mobility. The investigation was therefore limited to observations made on specimen surfaces with a $(10\bar{1}0)$ orientation since these surfaces can be re-etched with minor changes in surface quality.

III. MATERIAL AND TEST SPECIMEN PREPARATION

Compression test specimens of four different purities of zinc were prepared to investigate the influence of purity on dislocation mobility and the mechanical properties of zinc single crystals. A quantity of C. P. grade zinc of 99.999 per cent purity was obtained from the New Jersey Zinc Company. An analysis of this material furnished by the supplier indicated the following impurities in weight per cent:

Lead	0.0002
Iron	0.0002
Cadmium	0.00005
Other	< 0.00015

A quantity of material of this grade was further purified by zone refining. Zone refining was carried out under a helium atmosphere by passing a double zone furnace over a 6 ft long charge at the rate of 2 in./hr. A total of 10 double zone passes were made before the charge was removed from the furnace. The first 1/3 of each charge was used to grow single crystals. Quantities of two additional purities of zinc were made by doping 99.999 per cent purity zinc with 0.02 and 0.0025 weight per cent aluminum.

Single crystals of each of the four different purities were grown by the Bridgeman technique in graphite

coated Pyrex molds. The preparation of the molds and the details of the growing procedure have been described by Stofel (23). Cylindrical single crystals $7/8$ in. in diameter and 8 in. long were grown. Figure 6 shows a Pyrex mold and the single crystal grown in the mold. The orientation of a crystal was found by cleaving an end section that had been acid sawed from the crystal with 8N HNO_3 on a stainless steel wire 0.005 in. in diameter. The cleaving was done in liquid nitrogen with a needle struck by a light hammer. Crystals were cooled and heated at rates less than $5^\circ\text{F}/\text{min}$ to prevent damage due to thermal stresses. The cleavage surface established the orientation of the (0001) basal slip plane and the direction of large cleavage steps on the surface which correspond to the twin traces determined the $[\bar{1}1\bar{2}0]$ slip direction in the basal plane.

Compression test specimens in the form of $1/2$ in. cubes were machined with three different orientations of the basal slip plane with respect to the load axis. Figure 7 shows the orientations of the three different specimen types all of which have a set of (10 $\bar{1}$ 0) surfaces. The 45° and 80° type specimens were oriented for experiments on the basal slip system and the c-axis specimens were oriented for experiments on the nonbasal slip system. The 80° type specimens were used only in



Fig. 6 Pyrex Mold, a Section of a Crystal and a 1/2 in. Cube Specimen Trepanned from a Section of the Crystal.

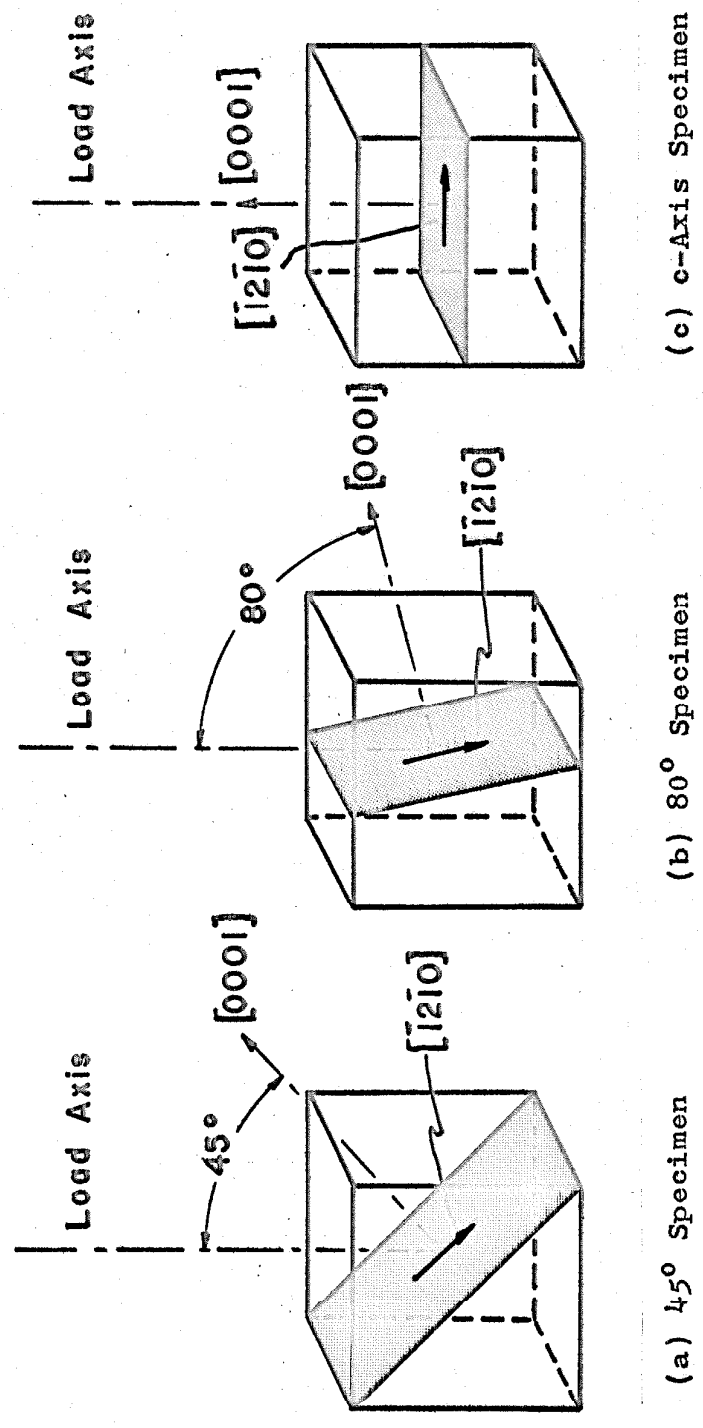


Fig. 7 Crystallographic Orientation of Test Specimens.

dislocation mobility experiments whereas the 45° and c-axis specimens were used in both stress-strain tests and mobility experiments.

Test specimens were machined from acid sawed and cleaved sections of the single crystals with the use of a Servomet Electric Spark Discharge Machine. The spark machining consisted of trepanning and planing operations at minimum spark energy settings. All spark discharge machining operations were done in oil at 200° - 210° F to prevent cleavage cracks. Spark machining at temperatures less than 190° F produced surfaces with visible cleavage cracks. Figure 6 shows a $1/2$ in. cube specimen trepanned from a section of a crystal. The machining operations resulted in specimen surfaces which were parallel to within 0.1° . The surface finish achieved by spark planing was of the order of 10μ in. r.m.s.

Uncertainty in the crystallographic orientation of the test specimens with respect to the surfaces resulted from machining operations. Table I gives the resulting uncertainty in the basal resolved shear stress from uncertainties in the orientation of the basal slip plane and slip direction with respect to the specimen surfaces on which compressive forces were to be applied. These surfaces will be designated as loading surfaces.

TABLE I

Resolved Shear Stress Uncertainty Resulting
from Orientation Uncertainty

Specimen Type	Axis Uncertainty		Resolved Shear Stress Uncertainty
	[0001]	[1210]	
45°	±1°	±1°	±0.01 per cent
80°	±0.1°	±1°	±1 per cent
c-axis	±0.1°	±1°	0.2 per cent of the normal stress (basal shear stress nominally zero)

Damage to the specimens resulting from the spark machining operations was removed chemically by polishing off approximately 0.005 in. of material and annealing at 700°F in a purified hydrogen atmosphere for 4 to 8 hr. The loading surfaces were masked with tape during the polishing to retain a flat surface. In the 45° specimens the depth of spark damage was found to extend as far as 1/8 in. below the surface. This damage occurred near only one edge of the spark planed surface. An example of the damage is shown in Fig. 8. The fan-like array of sub-boundaries indicates that kink bands consisting of edge oriented basal dislocations have formed along an unsupported edge of the specimen. Blocks of zinc of the same orientation as the specimen were cemented to most of the 45° specimens during planing operations to prevent this type of damage.

Specimen Edge,
Spark Planed Surface



[$\bar{1}2\bar{1}0$]

($10\bar{1}0$)

Specimen Edge

Fig. 8 Kink Damage from Spark Machining, 100X.

IV. EQUIPMENT AND TEST PROCEDURES

In this part of the thesis a detailed description of the various mechanical tests conducted on zinc single crystal test specimens is presented together with the procedures used in each type of test. Table II gives a summary of the tests conducted on specimens oriented for basal and nonbasal slip. The details of each type of test are presented in Table II. This part of the thesis is divided in sections which describe the static test fixture, dynamic test fixture and pulse load tests.

Static Test Fixture

Stress-strain tests on specimens oriented for basal slip were conducted in an Instron testing machine. A crosshead speed of 2×10^{-4} in./min and a load sensitivity of 10 lb full scale on a Speedomax recorder were used. Shear strain resulting from basal slip was measured with a Robertshaw Proximity Meter and parallel plate capacitors coupled to the specimen. Figure 9 illustrates the relation between the specimen and parallel plate capacitors which form one leg of a capacitance bridge. The relation between the capacitance and the plate separation of a parallel plate capacitor is given by

$$C = 0.225 \frac{KA}{d}$$

TABLE II

Summary of Tests

<u>Test</u>	<u>Slip System</u>	<u>Testing Machine</u>	<u>Test Fixture</u>	<u>Strain Measurement</u>
stress-strain	basal	Instron	static	capacitor plates
load pulse-long time	basal	Instron	static	none
stress-strain	nonbasal	Instron	dynamic	strain gages
variable strain-rate	basal	Instron	dynamic	capacitor plates
variable strain-rate	nonbasal	Instron	dynamic	strain gages
load pulse-short time	basal	rapid load	-	none
load pulse-long and short time	nonbasal	rapid load	-	none

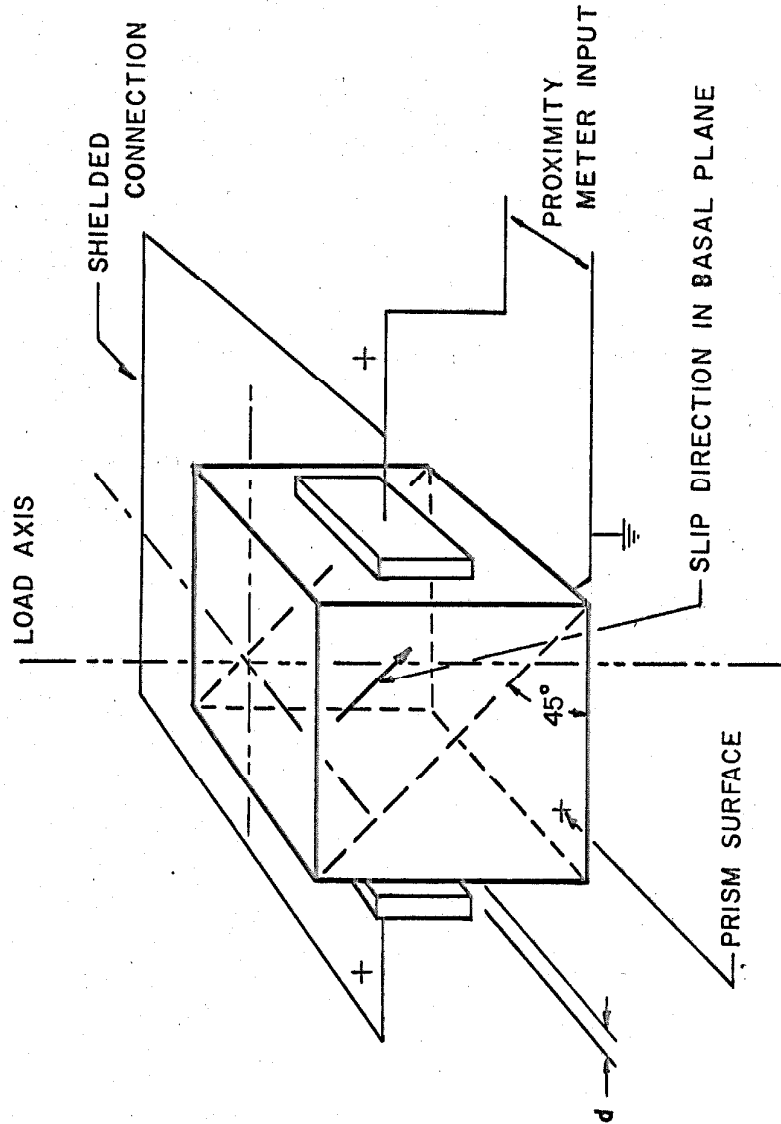


Fig. 9 Test Specimen and Parallel Capacitor Plates.

where

C = capacitance, $\mu\mu f$

K = dielectric constant

A = total plate area, in.²

d = plate separation, in.

For changes in plate separation where $\Delta d/d \ll 1$ the change in capacitance is given by

$$\Delta C = -C \frac{\Delta d}{d} .$$

The proximity meter output is proportional to the change in capacitance. Full scale sensitivity of the capacitance system is a function of the plate spacing, and the instrument sensitivity setting for a given scale range of the meter and plate area.

The instrument was calibrated for two different plate spacings. The initial plate spacing was controlled by two micrometer barrels which position the capacitor plates with respect to the specimen. For a plate spacing of 0.05 in. and a total capacitor plate area of 0.22 in.², the full scale meter reading was found to correspond to a change in plate spacing of 0.0005 in. on the most sensitive scale of the meter. A second calibration point was achieved for a plate spacing of 0.009 in. by measuring the Poisson expansion of a brass compression specimen. For this case, a change in plate spacing of 13×10^{-6} in. produced the full scale meter deflection.

Figure 10 is a photograph of the static test fixture. Two micrometer heads are used to control the initial spacing of the parallel plate capacitors and to permit accurate location of the specimen with respect to the loading axis. The cylindrical rod above the test specimen is attached to the crosshead of the Instron testing machine. The specimen is supported on a cylindrical rod which passes through a guide hole in the bottom plate of the fixture to allow the load on the specimen to be transmitted to the load cell of the testing machine. In this fashion, any interaction between the loaded portions of the system and the plate which holds the strain measuring probes is avoided. The cylindrical rod is guided in the fixture plate in such a way as to permit the specimen to be rotated about the load axis since the axis of the rod is accurately aligned with the load axis. The specimen is initially centered to locate the load axis along the center line of the specimen. The micrometer heads which position the plates are used for the centering operation. The specimen is rotated 90° after being centered in one direction in order to center the specimen in the transverse direction. The specimen alignment procedure is capable of limiting the error in the applied stress due to bending to less than 5 per cent of the average stress. The load is transmitted

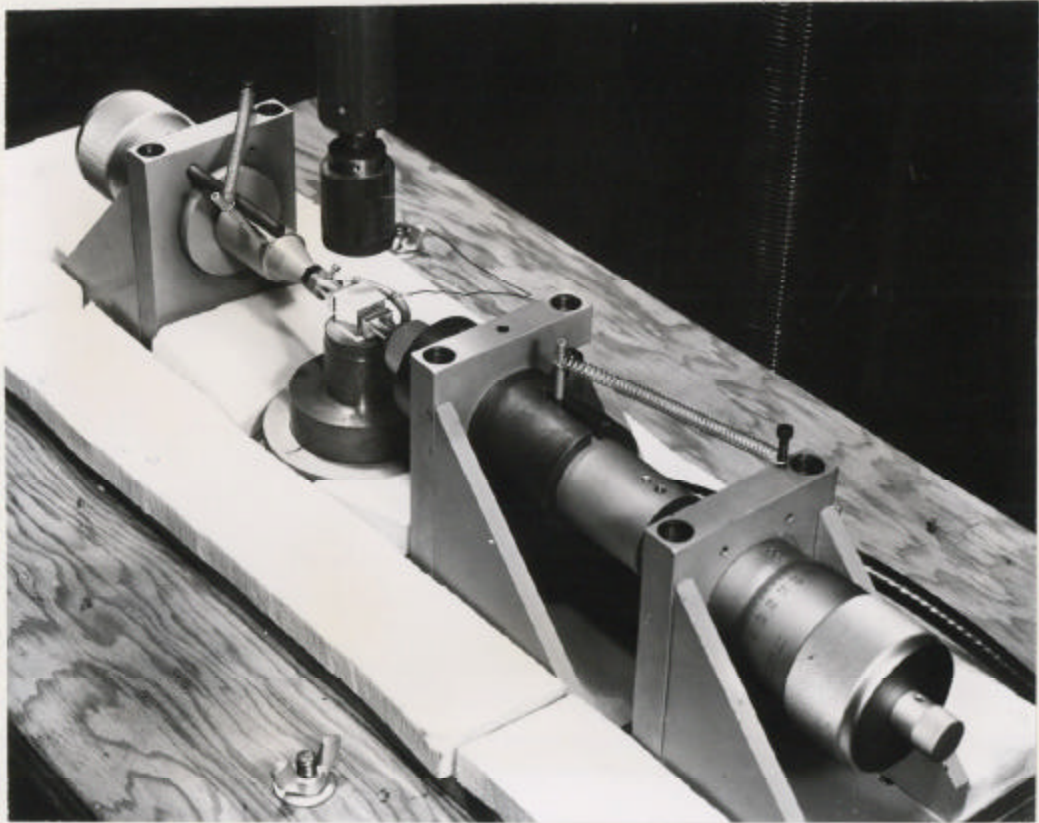


Fig. 10 Static Test Fixture.

through a spherical seat above the specimen to insure that specimens with slightly nonparallel ends are uniformly loaded.

The specimen, after being centered, was given a slight preload by manual control of the Instron cross-head. The required plate-to-specimen spacing was set after the position of the probe corresponding to zero plate separation had been found. An electrical contact gage was used in this operation to prevent surface damage to the specimen. An initial plate spacing of 0.01 in. resulted in a full scale sensitivity corresponding to a change in spacing of 60.5×10^{-6} in. at 33 per cent of the maximum meter sensitivity. The change in plate spacing is related to the elastic and plastic strain of the specimen by

$$\begin{aligned}\Delta d &= \frac{l\delta_p}{4} + \frac{l\sigma}{8} (S_{44} - 2S_{13} - S_{33} - S_{11}) \\ &= \frac{l}{4} (\delta_p + 1.4 \times 10^{-8} \sigma)\end{aligned}\tag{4}$$

where

Δd = change in plate to specimen spacing, in.

l = width of the specimen between capacitor plates, in.

δ_p = plastic basal shear strain of the specimen

σ = compressive stress applied to specimen ends, lb/in.²

S_{33} , S_{44} , S_{13} , S_{11} = coefficients of elastic compliance, in.²/lb.

Dynamic Test Fixture

Variable strain-rate tests were conducted in the Instron testing machine to determine the strain-rate sensitivity of the flow stress for the basal and non-basal slip systems. The load fixture for these tests and the methods of measuring strain in the specimens was different from that used for basal stress-strain tests.

Figure 11 is a schematic drawing of the dynamic test fixture along with the capacitor plates used to measure strain in 45° specimens oriented for basal slip. The bottom plate of the fixture was initially fixed to the Instron load cell table and the load cell was then leveled so that the plate was perpendicular to the lead screws of the machine. The top ball seat was then attached to the crosshead with Eastman 910 cement after it had been located on center with the centering pin in the bottom plate. The alignment procedure established the load axis to within 0.001 in. of the center axis of the bottom load seat. The lower ball assured that the force applied to the specimen was uniformly distributed even when the loading surfaces were not parallel. The top ball prevented small lateral translations of

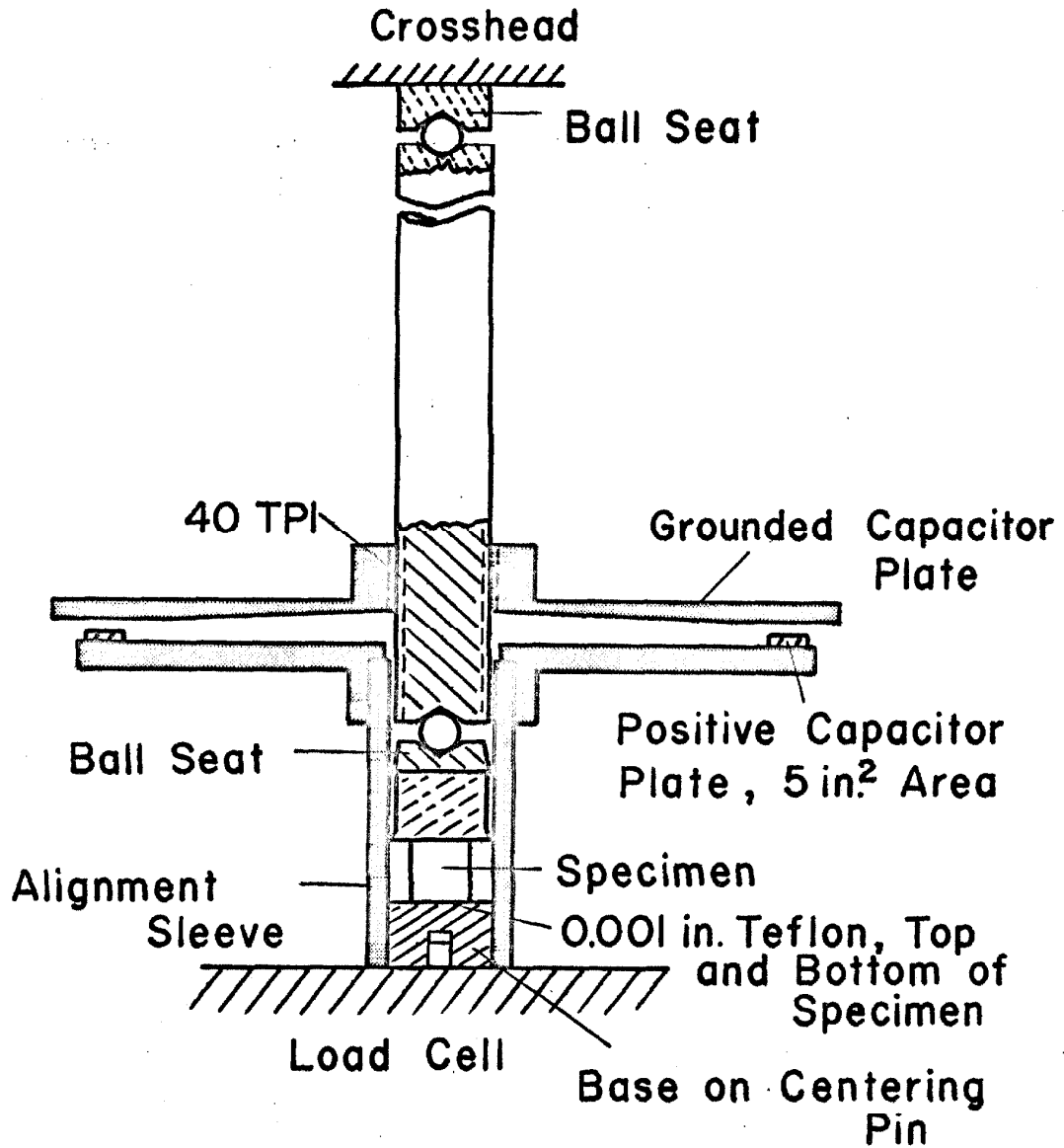


Fig. 11 Schematic of Dynamic Test Fixture.

the crosshead from being transmitted to the specimen. The line between ball centers defined the load axis.

The specimen was aligned with the axis of the bottom seat of the fixture with the aid of a cathatometer. This was done by rotating the seat and aligning the specimen so that each of the four corners coincided with a cross-hair in the focal plane of the cathatometer. The remaining parts of the fixture were then assembled without disturbing the specimen. Errors in the stress state resulting from alignment errors and the uncertainty of the load axis location were estimated to be less than 4 per cent of the resolved shear stress.

The capacitor plates shown in Fig. 11 were used in connection with the proximity meter to measure the compressive strain resulting from basal shear strain in the 45° specimens. The grounded capacitor plate is threaded onto the connecting rod so that the capacitor system can be calibrated before each test. The threaded connection permits adjustment of the plate spacing. The initial plate spacing used for strain-rate tests was 0.1 in. which together with a plate area of 5 in.² resulted in a full scale sensitivity of 0.0004 in. on the maximum sensitivity range of the proximity meter. Figure 12 is a photograph of the ^{compressive} dynamic test fixture and Fig. 13 ^{I.5} ^{II.6} shows details of the load seats and alignment sleeve.

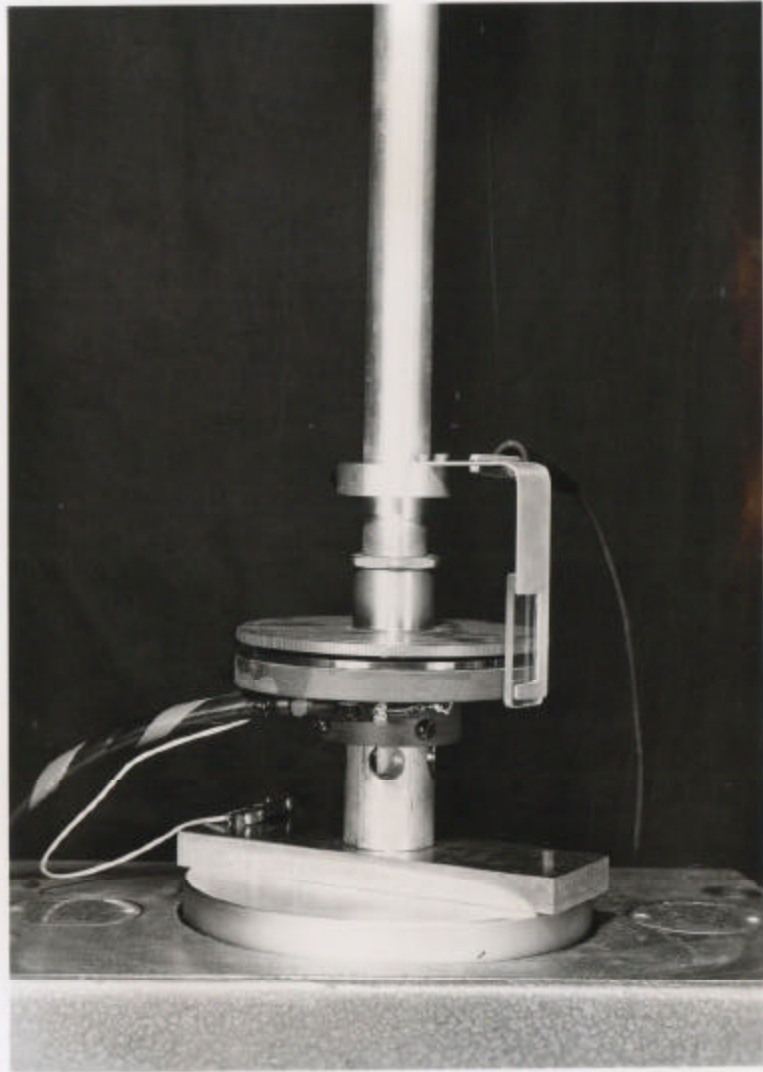


Fig. 12 ^{comp.} Dynamic Test Fixture.

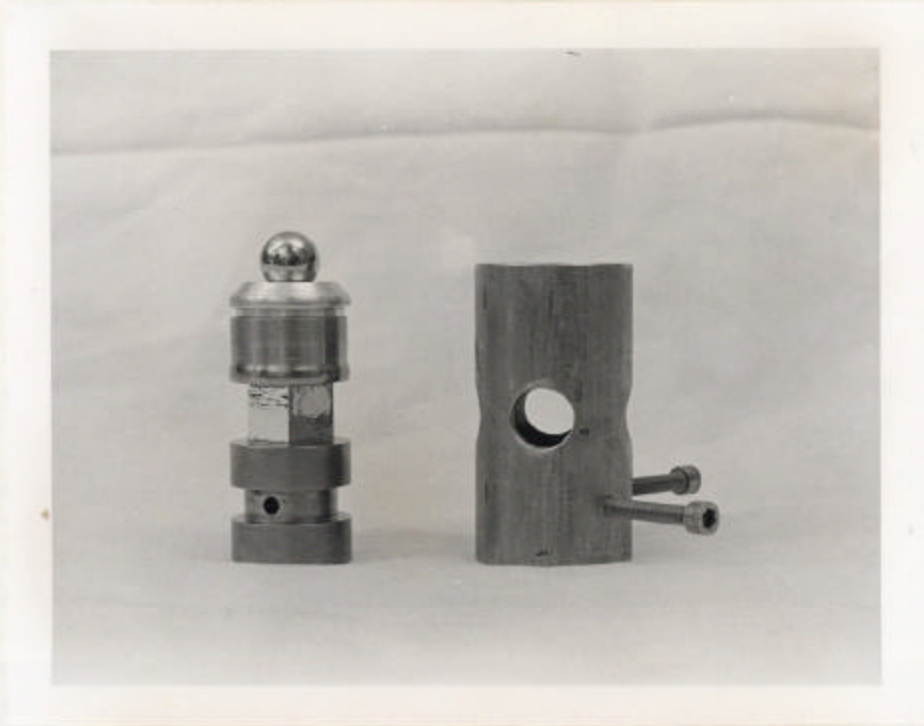
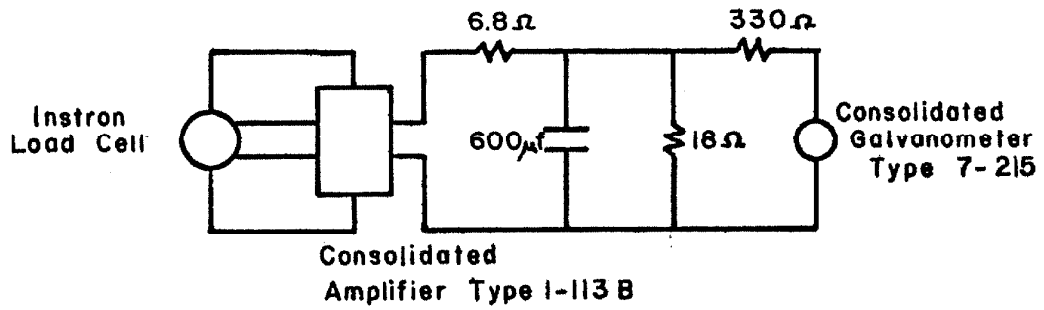


Fig. 13 Load Seats and Alignment Sleeve of Dynamic
Test Fixture.

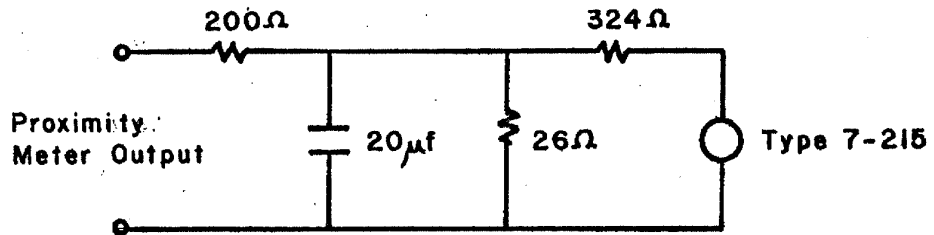
comp.

The Instron load cell and proximity meter outputs were recorded on a Consolidated Electro-dynamics oscillograph. The auxiliary circuits required to match the load cell strain gage amplifier and proximity meter output impedences to the oscillograph galvanometers and to filter out 60 cycle noise are shown in Fig. 14 along with the circuit used to provide timing marks on the oscillograph recording paper. A Consolidated Electro-dynamics Strain Gage Amplifier type 1-113B was used with the Instron load cell. The maximum load sensitivity of 10 lb full scale (7 in. of oscillograph paper) was maintained throughout the basal strain-rate tests by successively shifting the load zero point by 10 lb by means of a decade switch which shunted various resistances across one leg of the load cell bridge. A ten position decade switch effectively increased the oscillograph paper width from 7 in. to approximately 70 in. Figure 15 is a general view of the equipment.

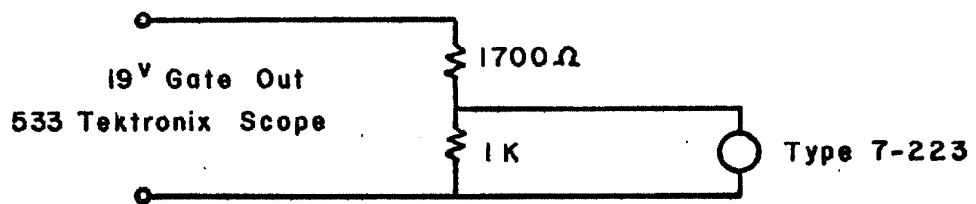
Calibration of the load cell was accomplished with dead weights after the compression fixture had been assembled. The capacitor plate system was calibrated over all sensitivity scales of the proximity meter to be used during each test. The scales used depended on the final value of strain desired in a given test and the length of the specimen in the direction of the load



(a) Load Cell Circuit



(b) Proximity Meter Circuit



(c) Timing Circuit

Fig. 14 Circuits Used in Dynamic System.

Sample No. 10 Test

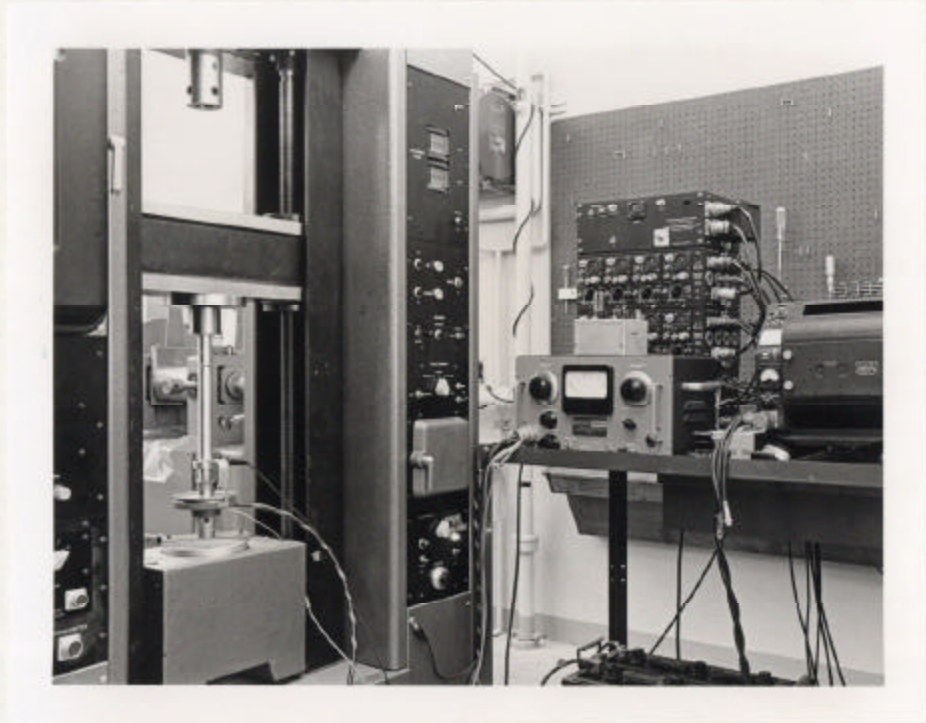


Fig. 15 General View of Test Equipment.

axis. The total sensitivity of the strain measuring system was governed by the initial plate spacing, the plate area of the capacitance gage and the sensitivity scale of the proximity meter.

Strain-rate changes were made during the tests by changing the crosshead speed of the Instron in the ratio of $1/\frac{1}{3}/\frac{1}{10}/0$. Full speed corresponded to the maximum crosshead speed of the Instron and this speed varied between 0.001 in./min and 0.005 in./min depending on the final value of strain of a test. Figure 16 is a tracing of the oscillograph record obtained with a complete sequence of crosshead speed changes. The load relaxation which occurs when the crosshead is stopped is due primarily to a characteristic of the machine as demonstrated by using a brass specimen which exhibits only elastic strain at the test loads.

The capacitance gage readings due to elastic strain in the fixture were determined using a brass specimen in place of a zinc crystal specimen. The elastic spring constant of the fixture was calculated from the measured capacitance gage readings and the loads applied to the brass specimen. The measured spring constant and the spring constant of the load cell were used to estimate the errors involved in assuming that the crosshead speed ratios were equal

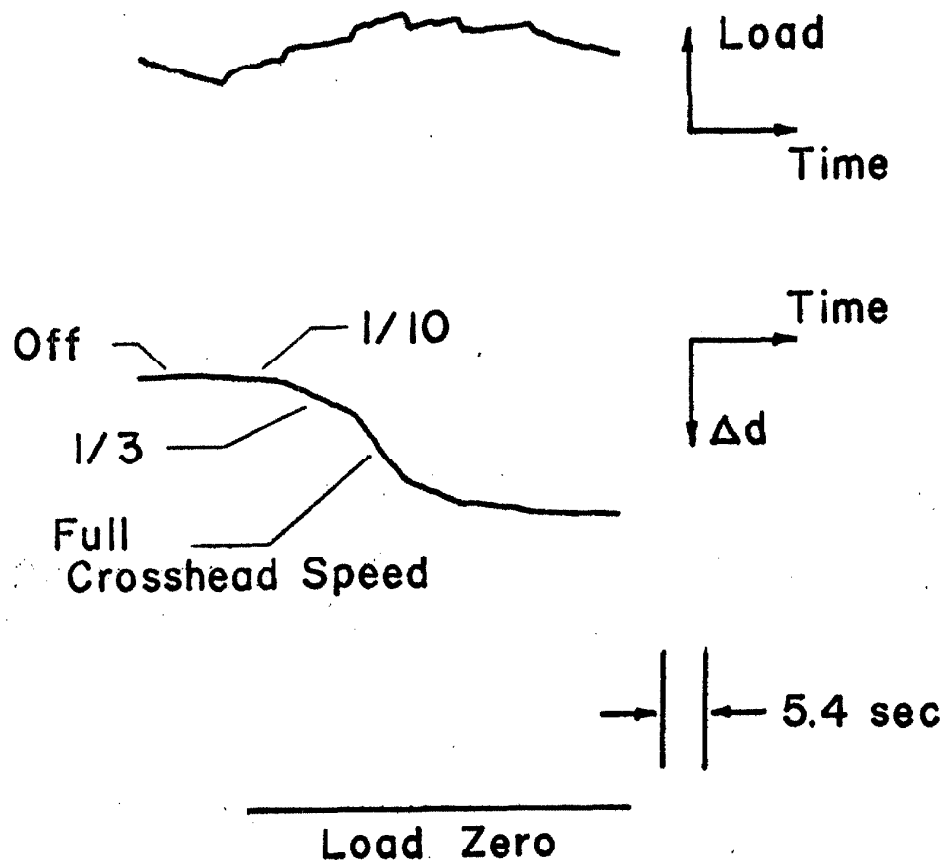


Fig. 16 Tracing of Oscillograph Record.

to the corresponding plastic strain-rate ratios in tests on zinc single crystals. This was a more accurate means of estimating the errors than measuring strain-rates directly because the load sensitivity of the system was relatively much greater than the strain sensitivity. The relation between the plastic strain-rate ratio and the crosshead speeds is given by

$$\frac{\dot{\epsilon}_{P_1}}{\dot{\epsilon}_{P_2}} = \frac{\dot{y}_1 - \dot{L}_1/K_T}{\dot{y}_2 - \dot{L}_2/K_T} \quad (5)$$

where

$\dot{\epsilon}_P$ = plastic strain rate

\dot{y} = crosshead speed

\dot{L} = load rate

K_T = total spring constant of the system including both ball seats, the load cell and the specimen.

For basal strain rate tests, the maximum error in assuming

$$\frac{\dot{\epsilon}_{P_1}}{\dot{\epsilon}_{P_2}} = \frac{\dot{y}_1}{\dot{y}_2}$$

was found to be less than 5 per cent, so no correction for elastic strain of the system was made in the analysis of the records.

Variable strain-rate tests on c-axis specimens oriented for nonbasal slip were conducted using the same test procedure and dynamic system as used for basal strain-rate tests except for strain measurement.

Specimens deformed in nonbasal slip work-harden at such a high rate that the correction term relating $\dot{\gamma}_i$ to $\dot{\epsilon}_p$, as given in Eq. 5 becomes large. To eliminate the correction term, strain gages were used to measure compressive strain directly. Type C40 foil strain gages obtained from the Budd Instrument Company were bonded to the $(\bar{1}2\bar{1}0)$ surfaces of the specimens with Duco cement and wired in the circuit shown in Fig. 17 so as to cancel bending strains. Two dummy gages were mounted on another specimen for temperature compensation. The bridge circuit output was amplified and recorded on the oscillograph along with the load. The associated circuit is shown in Fig. 17. A shunt resistor was used to calibrate the strain gage circuit. A full scale strain sensitivity of 160×10^{-6} in./in. was maintained throughout the tests by the use of a series of shunting resistors connected in one leg of the strain gage bridge measuring strain. The load sensitivity for the nonbasal tests was 100 lb full scale which was also maintained throughout the tests.

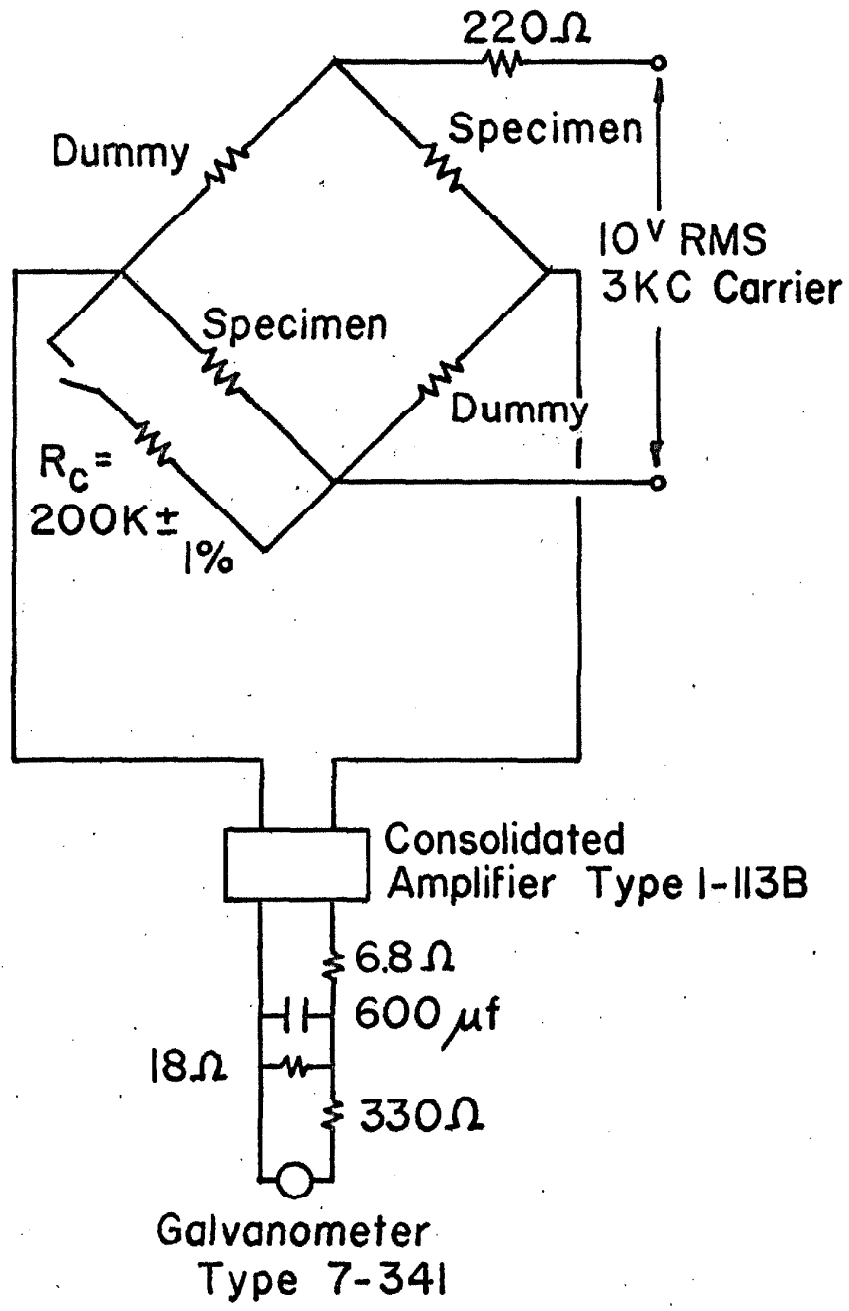


Fig. 17 Strain Gage Circuit.

Pulse Tests

The static loading system used for basal stress-strain experiments was used to apply long duration pulses to specimens oriented for basal slip (45° specimens). The pulses were applied by manually controlling the crosshead motion of the Instron testing machine. A pulse of 3 sec rise time was easily achieved with this system. Such a rise time limited the minimum pulse duration to about 30 sec because a good approximation to a square wave was desired.

Short and long duration pulses were applied to specimens oriented for basal and nonbasal slip in a rapid load testing machine (24). This machine is capable of applying pulse loads with a rise time of 2×10^{-3} sec and minimum duration of 17×10^{-3} sec. Loads were measured with a Consolidated Electrodynamics oscillograph using a four leg dynamometer bridge of high output silicon filament gages obtained from Micro Systems, Inc., Pasadena, California. Figure 18 shows the gage circuitry. Examples of load pulse records are given in Fig. 19 for loads of 13.1 lb and 491 lb.

The rapid load machine was converted from a tensile testing machine to a compression machine by means of a special fixture. The compression fixture, as shown schematically in Fig. 20 is a self-aligning system of

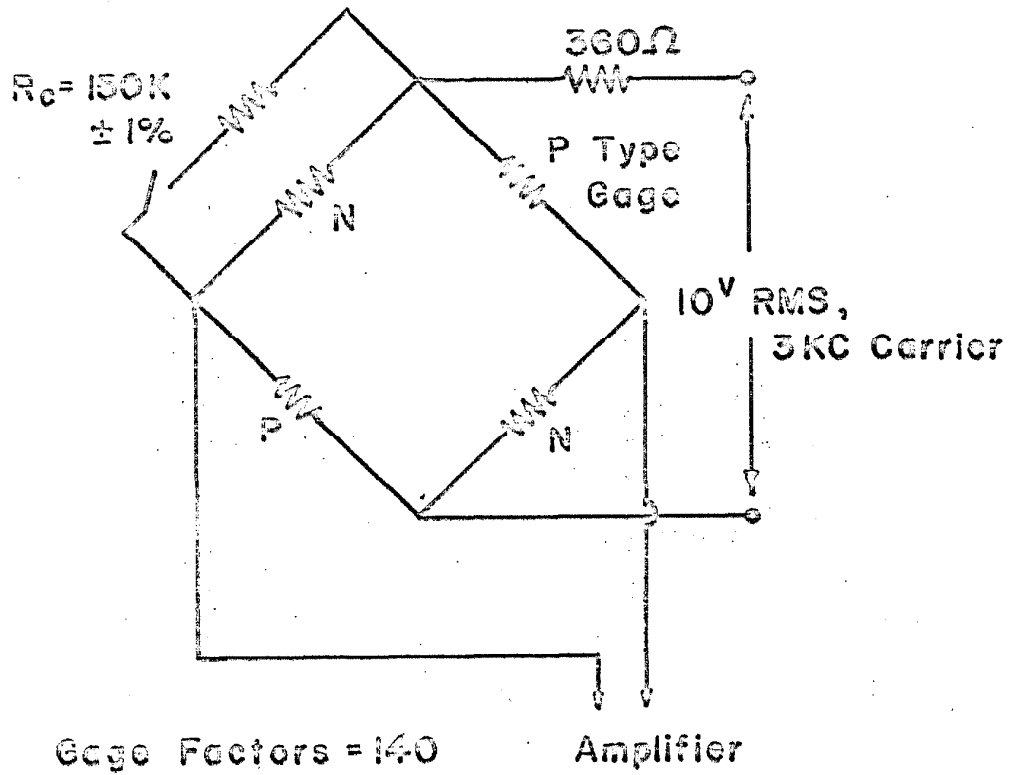


Fig. 18 Dynamometer Strain Gage Circuit.

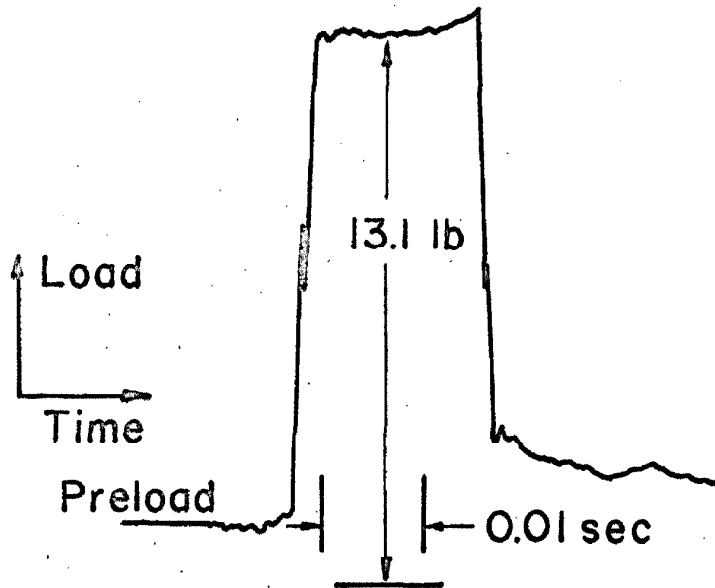
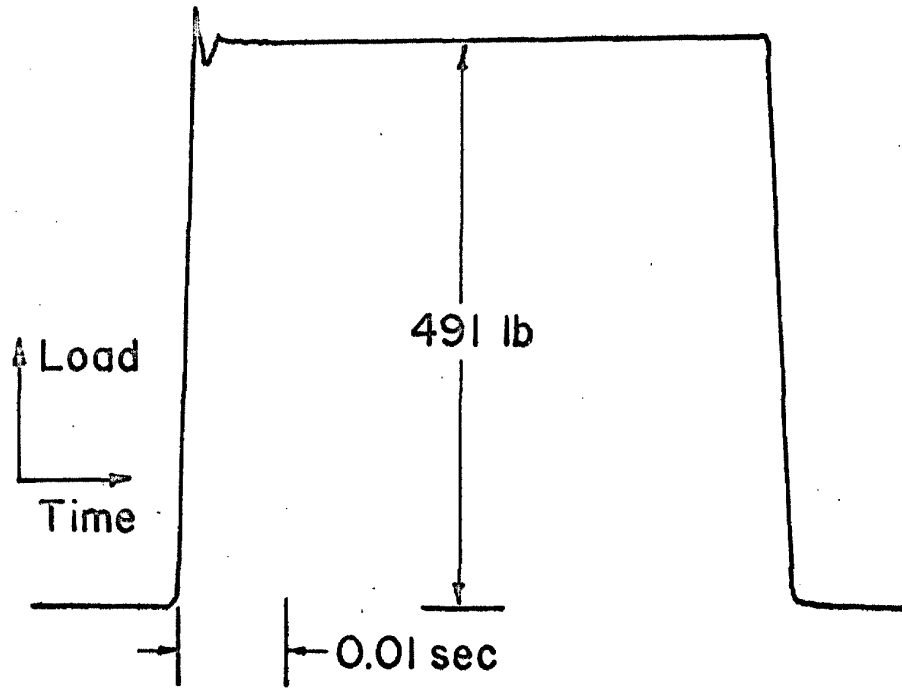


Fig. 19 Tracing of Rapid Load Records.

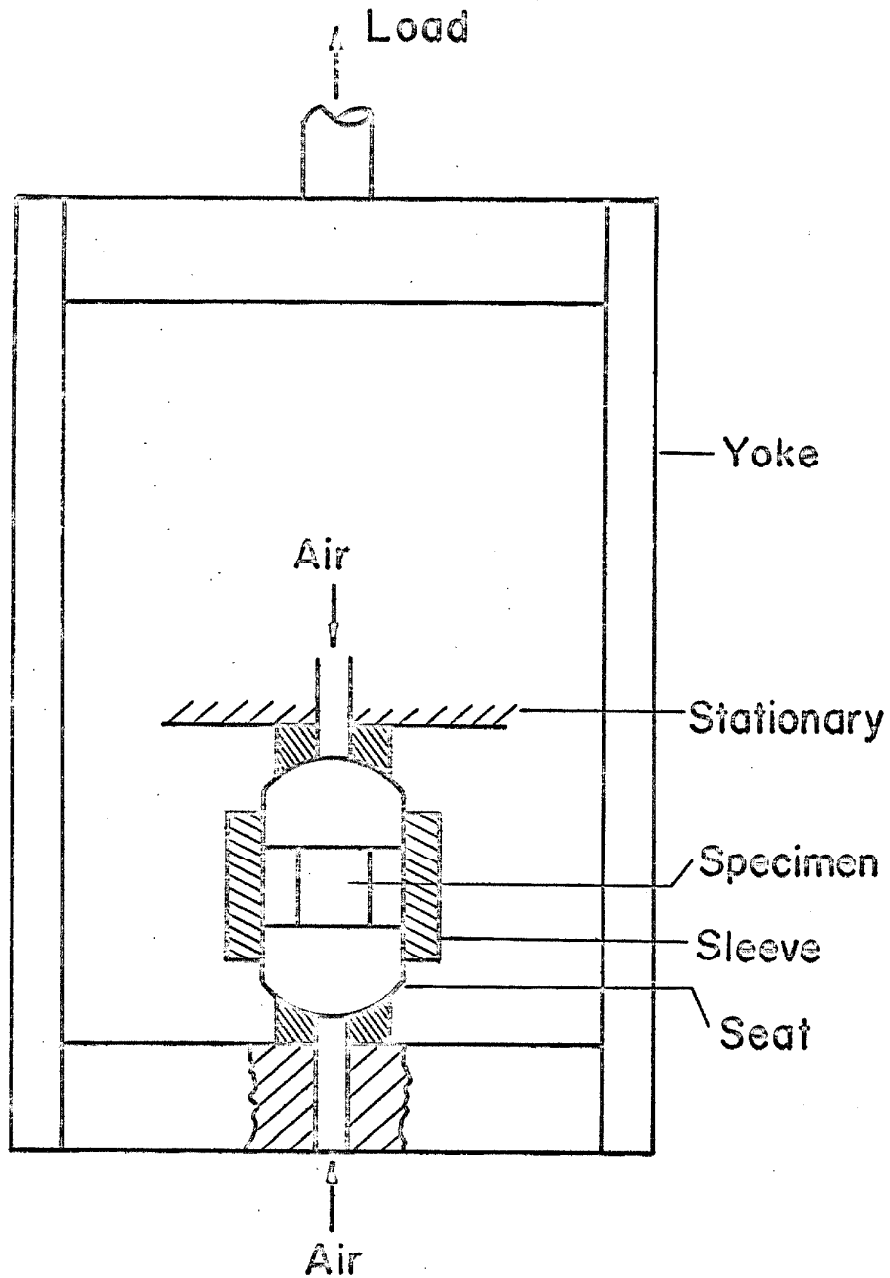


Fig. 20 Schematic of Compression Fixture for Rapid Load Machine.

spherical seats supported by air pressure. The air bearing feature minimizes alignment errors due to friction between the bearing surfaces and hence reduces the error produced when the load axis is off the centroid of the specimen. The system is stable because the spherical bearing surface centers are "crossed." A specimen 1 in. in length can be accommodated before the centers become uncrossed leading to instability.

The spherical seat end pieces were made from a 2 in. diameter chrome steel ball bearing by spark machining operations with a Servomet Electric Spark Discharge Machine. The cylindrical surface which is a reference surface for specimen alignment was finished ground in a lathe using a tool post grinder. The cylindrical axis is known to be within ± 0.0002 in. from the spherical surface radius passing normal to the plane specimen loading surface.

The specimen is aligned in the load fixture outside the testing machine. Figure 21 shows the system used to align the specimen using the cylinder surface of the seats as a reference surface. The bottom seat is placed inside the alignment sleeve which is in an inverted position on a mandrel. The seat is rotated and the specimen centered with the use of a cathatometer. The sleeve is then removed, inverted and lowered past the

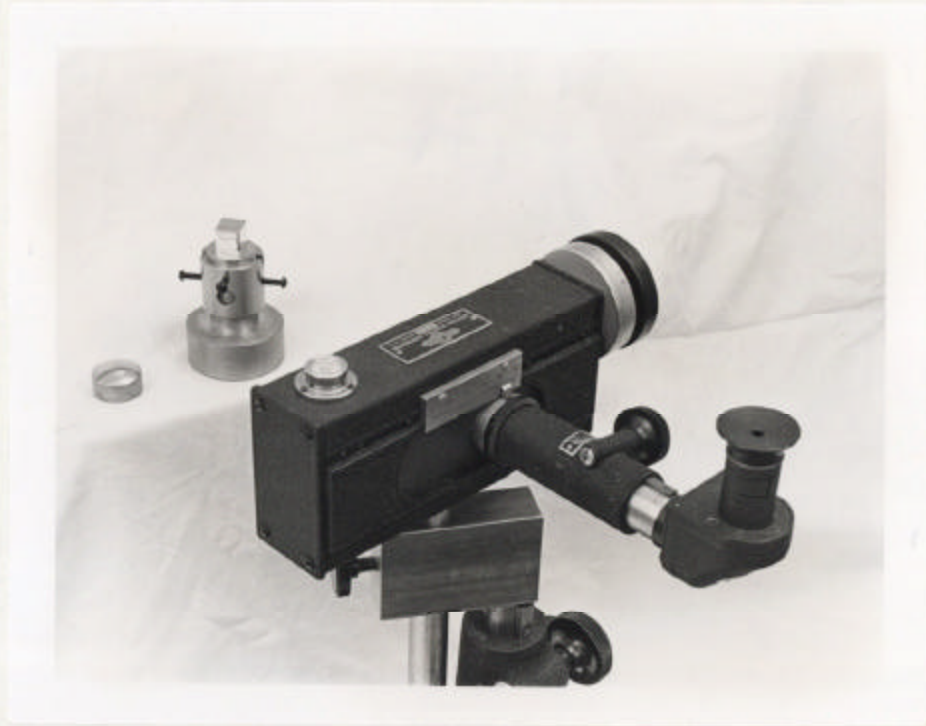


Fig. 21 Specimen Alignment Equipment.

specimen and around the lower seat. Nylon set screws are tightened against the bottom seat to keep the sleeve in place as the top seat is inserted into the sleeve. Extreme care is taken so as not to move the specimen during these operations.

The specimen-seat assembly is placed in the compression fixture of the rapid load testing machine and a preload of 1 or 2 lb is applied depending on the level of the final desired load. For a final load of less than 5 lb, a preload of 1 lb is used and for greater than 5 lb, a preload of 2 lb is used. The air supply for the seats is adjusted so as to float the specimen assembly after the alignment sleeve has been lowered to a position where the top of the sleeve is clear of the top seat. Set screws hold the alignment tube in this position during the test. Figure 22 shows the assembly in the rapid load testing machine ready for testing. Figure 23 shows details of the air bearing assembly. Figure 24 is a schematic drawing of the air supply system for the load bearing. To float the assembly while under preload, a supply pressure of 20 lb/in.² was maintained and the needle valves were adjusted to establish a flow rate of 0.08 ft³/hr of air. The calculated gap in the air bearings under these conditions and a load of 2 lb is 0.0004 in. For final

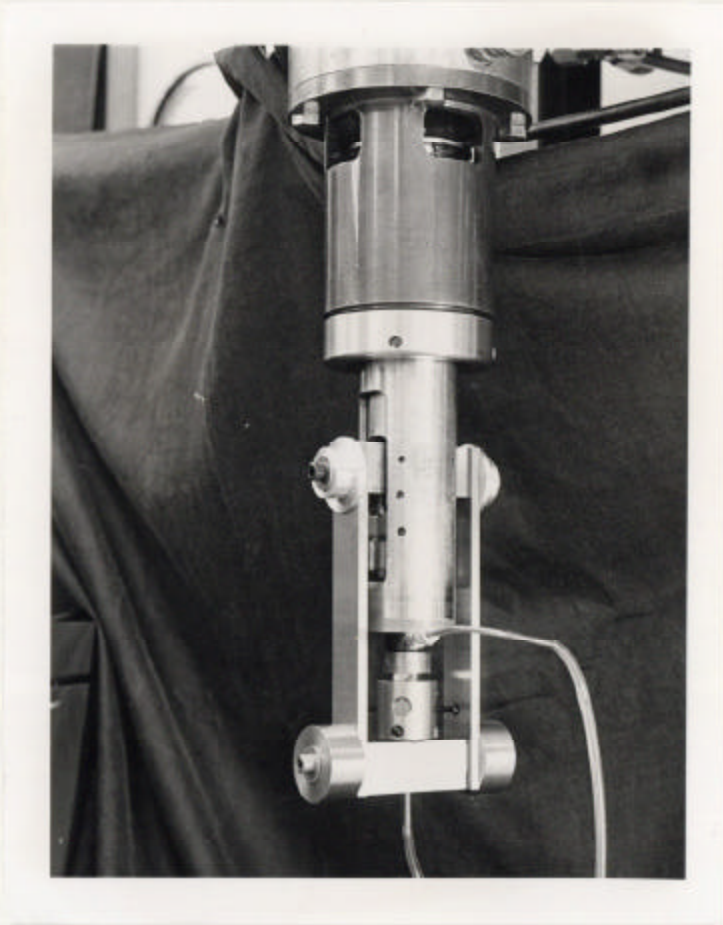


Fig. 22 Rapid Load Testing Fixture.

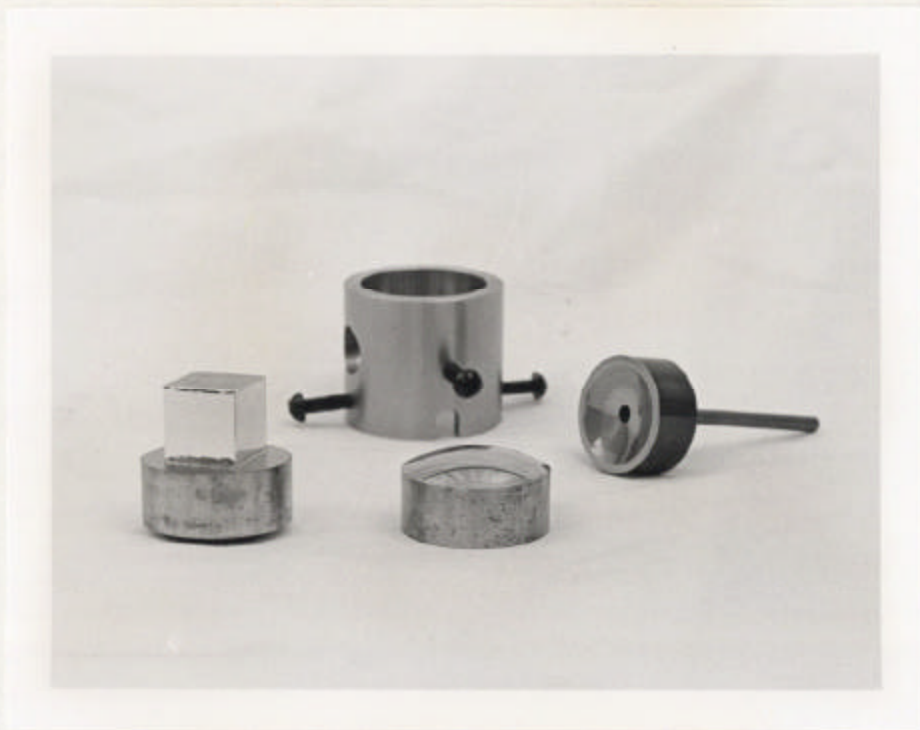


Fig. 23 Spherical Seats and Alignment Sleeve.

Air Bearings

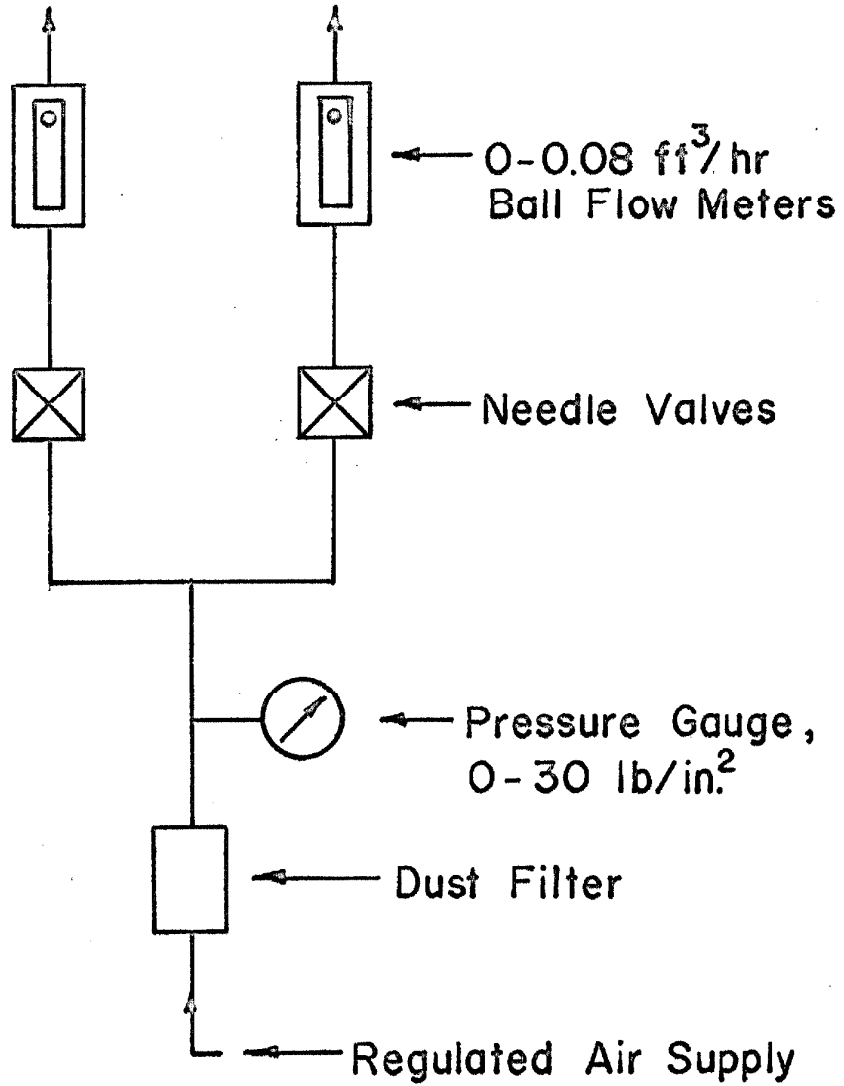


Fig. 24 Air Supply System for Bearings.

load levels less than 10 lb the air supply was shut off before loading to insure that the seat surfaces would contact under the final load. Specimen alignment errors and errors caused by friction in the load bearings were estimated to give less than a 5 per cent error in the applied stress due to bending stresses and rotation of the specimen axis with respect to the loading axis.

Both long and short duration pulses were applied to c-axis specimens oriented for nonbasal slip. The rapid load machine was used exclusively for pulse loadings of c-axis specimens. A range of loading times from 17×10^{-3} sec to 45 sec and loads from 100 lb to 500 lb were used in these tests.

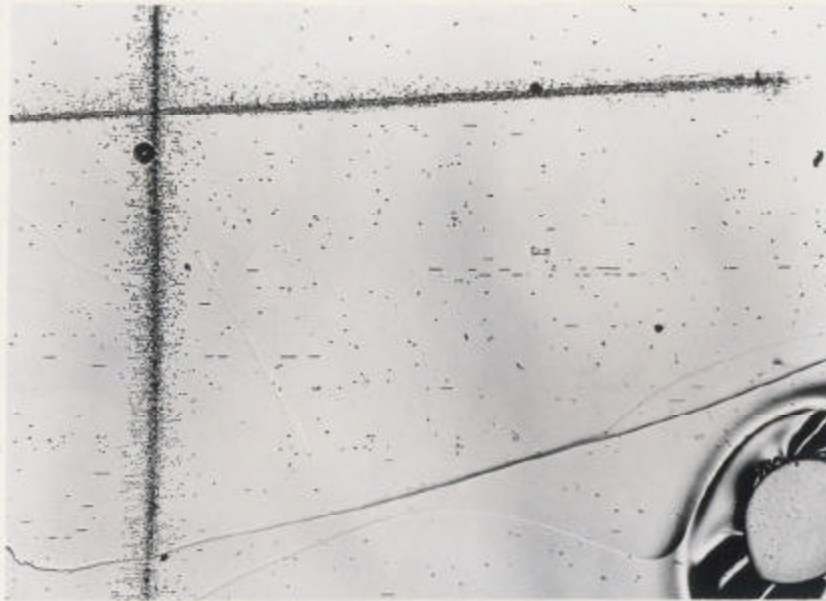
The specimens were etched prior to a pulse test and replicas of the etched surfaces were made prior to testing to record the initial dislocation density and configuration on $(10\bar{1}0)$ surfaces of the specimens. The replication technique used a solution obtained from Ladd Industries and 0.005 in. thick cellulose acetate film. Several drops of solution are applied to the specimen surface with a brush and the acetate film is placed on the liquid film and pressed against the specimen. The film is allowed to dry for about 5 min and then a piece of Mylar backing film 0.015 in. thick with double-sided Scotch Brand tape is placed on the acetate film and the film is stripped from the specimen.

After pulse testing, the specimens were re-etched and again replicated. The elapsed time between test and re-etch was usually limited to less than 3 min to minimize dislocation rearrangement. The mercury introduced during the initial etch was sufficient to cause etch pits to form during the second etch. The number of pulse tests that could be conducted before the specimen had to be annealed was determined by the amount of deformation or increase in dislocation density produced in a series of tests and by the conditions of the $(10\bar{1}0)$ specimen surfaces after several re-etching operations. In several cases, as many as twenty pulse tests were conducted on a specimen before high temperature annealing was required because the dislocation density had reached too high a level.

[The replicas of the etched surfaces were transparent and hence not suitable for optical examination. To make them reflective, a layer of aluminum was vapor deposited on the replicas at vacuum pressures of less than 5×10^{-5} mm of Hg. Optically opaque films of aluminum were sufficiently reflective for optical examination with a metallurgical microscope and were not so thick as to obscure details on the replicas at magnifications less than 500X.]

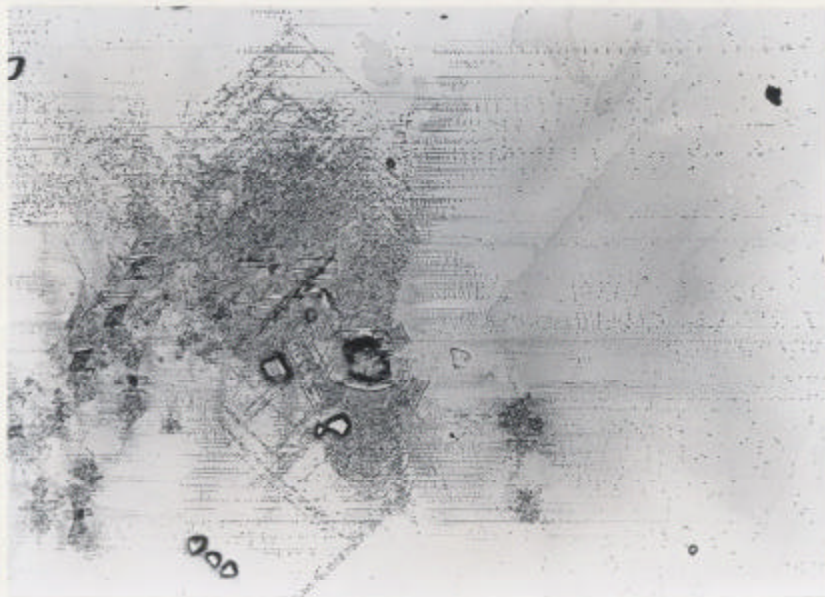
Before annealing specimens which had been previously etched, a vacuum treatment was required to remove the mercury from the surfaces. Specimens were placed in a vacuum of 10^{-6} to 10^{-5} mm of Hg for 8 hr for this purpose. Subsequent annealing was carried out in a purified hydrogen atmosphere at 700°F for 4 to 8 hr. This annealing procedure was also used after all stress-strain tests and strain-rate tests to return the specimen to as near its original pretest condition as possible.

Tests were conducted wherein "fresh" dislocations were introduced into a specimen by intentional damage prior to pulse load testing. In all such cases the specimens were etched after the introduction of the fresh dislocations in order to record the exact nature and extent of the damage. After replication of the surface, the pulse test was conducted. Various means were used to introduce damage such as scratching with a diamond phonograph stylus, razor blade, small cleavage fractures produced by spark planing below 190°F and thermal expansion damage induced with a piece of copper sheet cooled to liquid nitrogen temperature. Figure 25 shows examples of the damage produced on $(10\bar{1}0)$ planes as a result of scratches and thermal damage.



(a) Scratch Damage

$(10\bar{1}0)$



(b) Cold Tool Damage

$[\bar{1}2\bar{1}0]$

Fig. 25 Damage from Scratches and Cold Tool, 100X.

V. EXPERIMENTAL RESULTS

The results of the experimental investigation are described in this part of the thesis. The results are divided into sections covering the static tests, dynamic tests, pulse tests, strain-rate sensitivity of the flow stress, influence of purity and strain on dislocation substructure and dislocation pile-ups.

Static Tests

A. Basal Slip System

The shear stress-shear strain behavior for basal slip of 99.999 per cent purity and zone refined purity test specimens was measured in the Instron static test system at a constant crosshead speed of 2×10^{-4} in./min. The results of two tests on a zone refined specimen are shown in Fig. 26. The shear strain was taken as $\gamma = 4 \frac{\Delta d}{l} = \gamma_p + 1.4 \times 10^{-8} \sigma$ from Eq. 4 and the resolved shear stress as $\sigma/2$. The first test was conducted on the specimen after it was machined and annealed. The second test was conducted after annealing the specimen at 700°F for 2 hr following the first test. The critical resolved shear stress was taken as the stress corresponding to the first detectable deviation from linear stress-strain behavior when the strain sensitivity of the system was 1×10^{-6} in./in. The critical

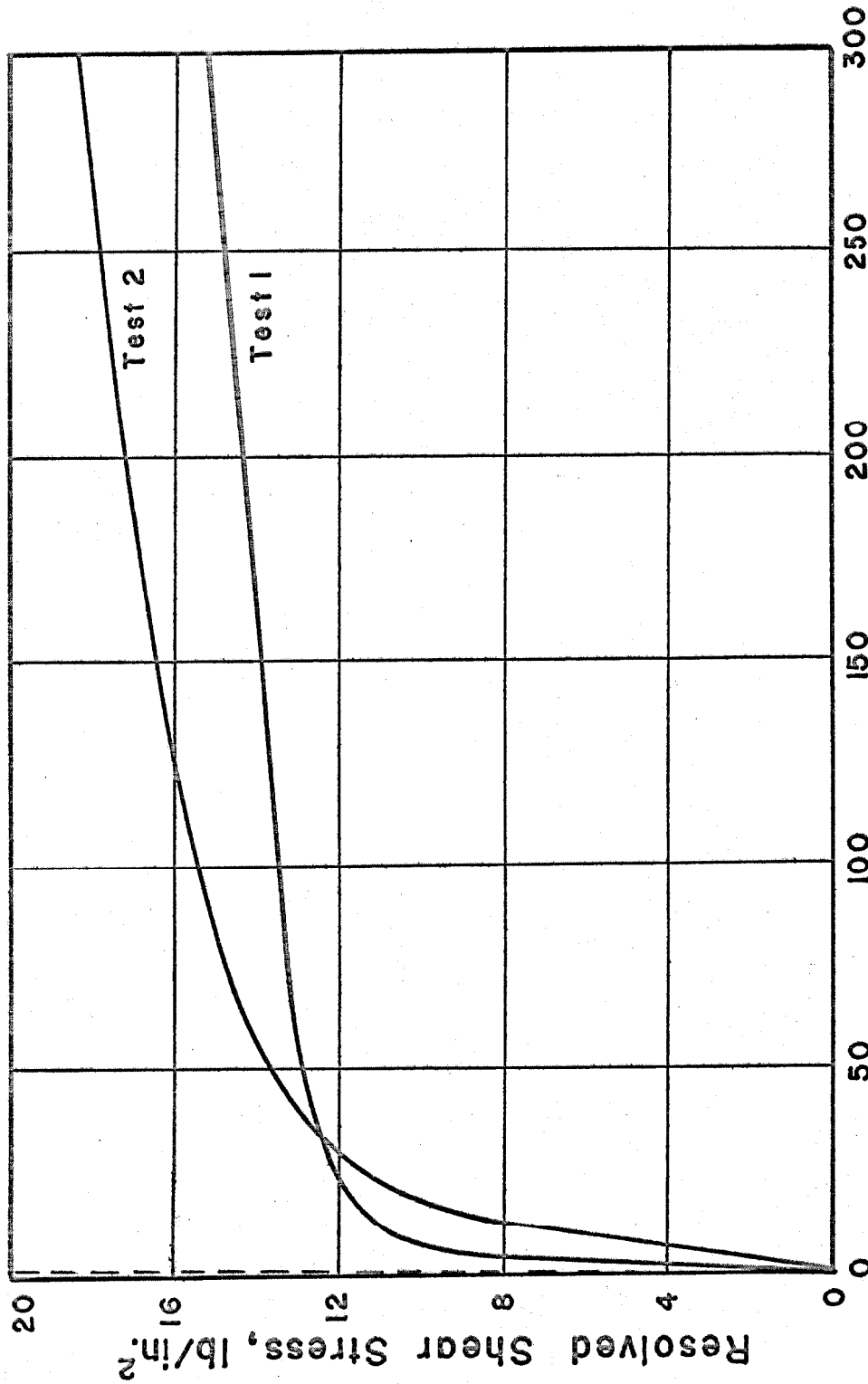


Fig. 26 Resolved Shear Stress vs. Resolved Shear Strain for Basal Slip. Specimen 17-1, Zone Refined Purity.

resolved shear stress was approximately the same for both tests. At strains greater than 200×10^{-6} in./in. the slope of the stress-strain curves was approximately the same for both tests with the curve for the second test being above the initial curve. The dashed, straight line represents the calculated elastic curve for both tests. The initial portion of the stress-strain curves did not correspond to the elastic curve. This was probably the result of translation or rotation of the compression specimen proportional to the load. A translation of approximately 0.001 in. or a rotation about the specimen base of 0.3° at 10 lb/in.^2 would give the slope observed in Test 2. A critical resolved shear stress of about 9 lb/in.^2 was observed for the zone refined specimen. A static test on a specimen of 99.999 per cent purity indicated a critical resolved shear stress of 12 lb/in.^2 .

One static test was conducted to determine the change in dislocation density with a given amount of plastic deformation. A specimen of 99.999 per cent purity was etched and replicated prior to the test to record the initial dislocation density as revealed on the $(10\bar{1}0)$ surfaces of the test specimen. The specimen was re-etched within one minute after the test to determine the final density. An increase in density from

$1 \times 10^5 \text{ cm}^{-2}$ to $5 \pm 0.8 \times 10^5 \text{ cm}^{-2}$ was found for a strain of $3.6 \times 10^{-4} \text{ in./in.}$ Dislocation densities were determined by counting the number of etch pits per unit area on photomicrographs of the replicas taken at 100X.

B. Nonbasal Slip System

The stress-strain curve for nonbasal slip was obtained on a 99.999 per cent purity c-axis specimen. The results on specimen 26-6T1 are shown in Fig. 27 where compressive stress on basal planes is plotted against compressive strain along the c-axis of the test specimen. T1 in the specimen designation means the first test on this specimen. The test was conducted in the Instron testing machine at a constant crosshead speed of 0.001 in./min. The dynamic test fixture seen in Fig. 12 was used together with a strain gage circuit to measure compressive strain along the c-axis. Type C40 strain gages were cemented to the $(\bar{1}2\bar{1}0)$ surfaces of the specimen and the gage circuit output and load were recorded on the Instron X-Y chart recorder. A strain sensitivity of $5 \times 10^{-6} \text{ in./in.}$ was achieved with this system. The stress-strain curve shows that plastic deformation first occurs at about 1500 lb/in.^2 which is taken as the point where the curve deviates from a linear stress-strain relation. The work-hardening

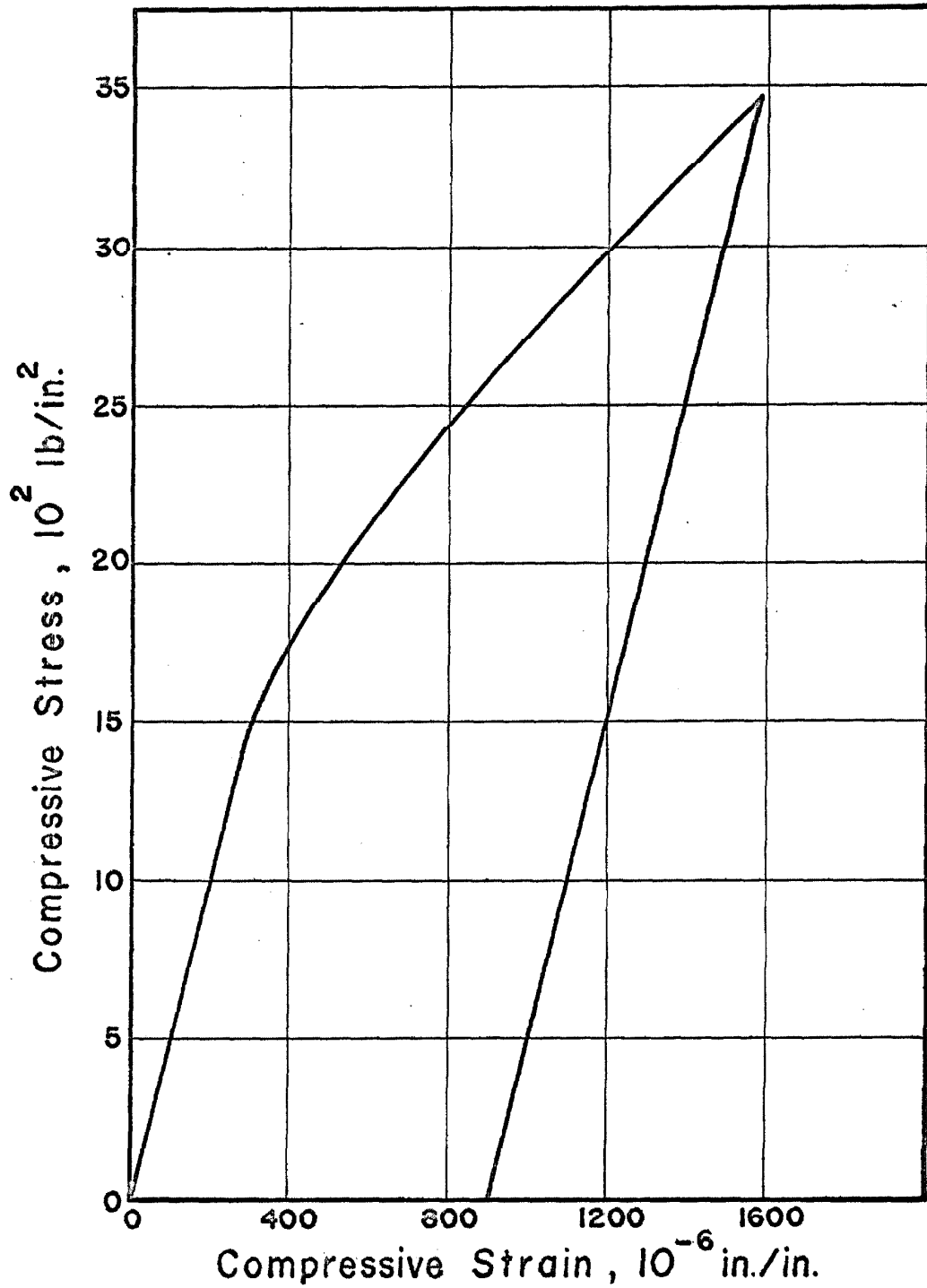


Fig. 27 Compressive Stress vs. Compressive Strain for Nonbasal Slip. Specimen 26-6T1, 99.999 Per Cent Purity.

rate in the plastic region is high relative to that in the basal slip system.

The c-axis test specimen was etched before and after the strain-rate test to determine changes in dislocation density. Figure 28 shows the dislocation density after 900×10^{-6} in./in. of permanent strain along the c-axis. The dislocation density as revealed on a $(10\bar{1}0)$ surface increased from about $1 \times 10^5 \text{ cm}^{-2}$ to $3 \pm 1 \times 10^6 \text{ cm}^{-2}$ as a result of nonbasal deformation. Only the center region in Fig. 28 is representative of the dislocation density on a $(10\bar{1}0)$ surface because the test was conducted on a $3/8$ in. diameter cylindrical test specimen.

Dynamic Tests

A. Basal Slip System

Results of variable strain-rate tests conducted in the Instron dynamic test system on specimens oriented for basal slip were analyzed to give shear stress-shear strain behavior to strain levels of about 1 per cent. The load and strain corresponding to the zero strain-rate part of the variable strain-rate cycle were used to plot the stress-strain curves shown in Fig. 29. Test results from specimens of four different purity levels are shown. The four tests were conducted at a full Instron crosshead speed of 0.001 in./min with speed changes in the ratios of $1/\frac{1}{3}/\frac{1}{10}/0$.



Compression
Axis

$[\bar{1}2\bar{1}0]$

$(10\bar{1}0)$

Fig. 28 Dislocation Density Resulting from Compressive Strain of 900×10^{-6} in./in. along c-Axis. Specimen 26-1T1, 99.999 Per Cent Purity, 50X.

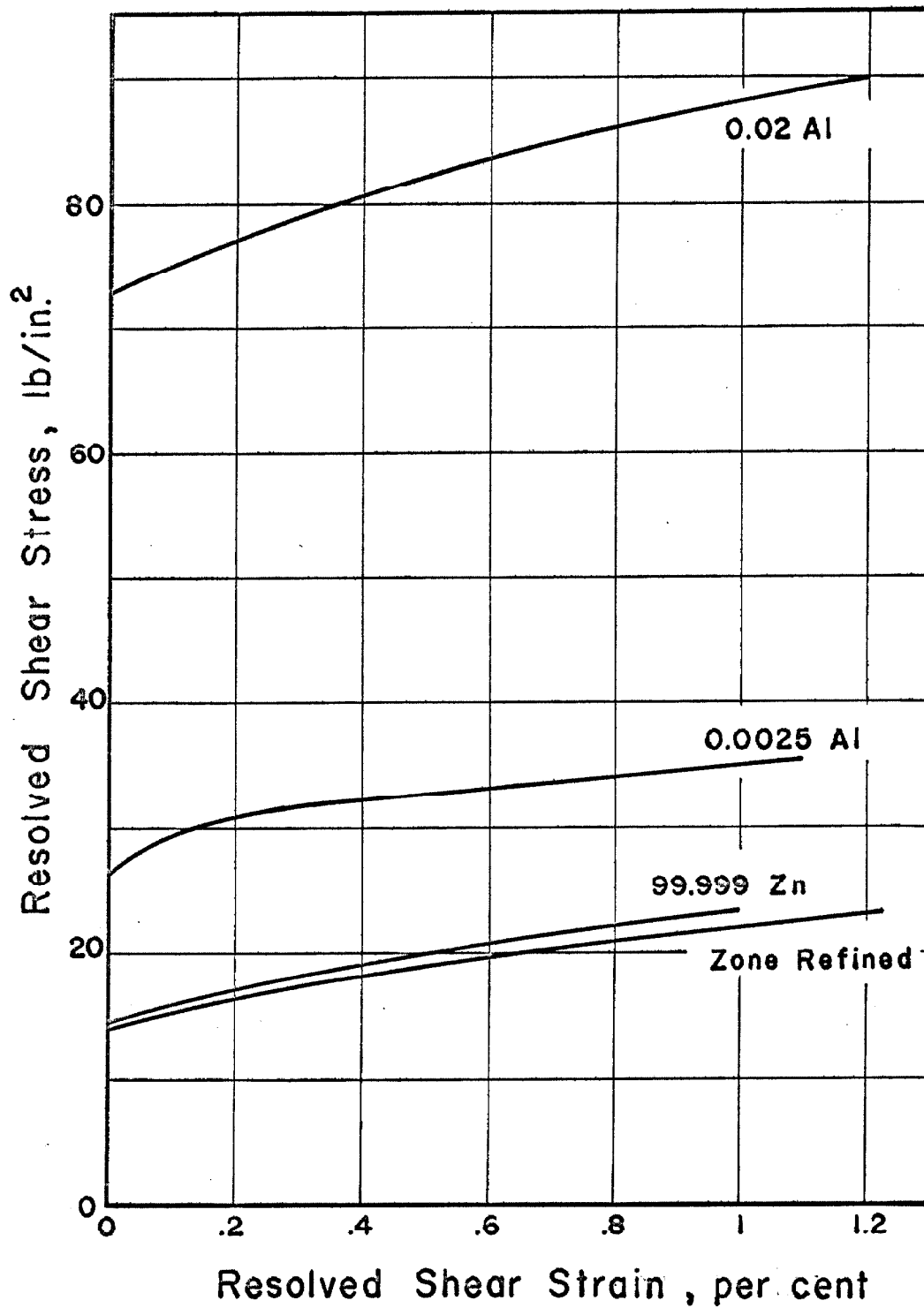


Fig. 29 Influence of Purity on Basal Stress-Strain Curves.

Graph from Fig. 29

Figure 29 shows that with increasing impurity additions the stress-strain curve is shifted to higher stress levels. Work-hardening rates are relatively unchanged although some variation in work-hardening rate can be seen. This may have been due to the fact that the strain-rate cycles were not conducted at the same frequency from one test to another. The results shown in Fig. 29 are from specimens in the annealed state that had not been previously deformed.

The influence of prior strain on the stress-strain curve for two different purities is shown in Fig. 30. Test 2 results were obtained on the previously deformed specimens after an annealing treatment. The effect of prior deformation is to shift the stress-strain curve to higher stresses without appreciably changing the work-hardening rate.

Several specimens tested under variable strain-rate conditions were etched before and after testing to determine dislocation density changes and the general nature of the dislocation arrays resulting from plastic deformation. Figure 31 shows similar areas on a specimen before and after 1 per cent shear strain. Both photographs are of random areas on a Zn-0.0025Al specimen and are generally representative of the entire specimen in terms of dislocation density and substructure.

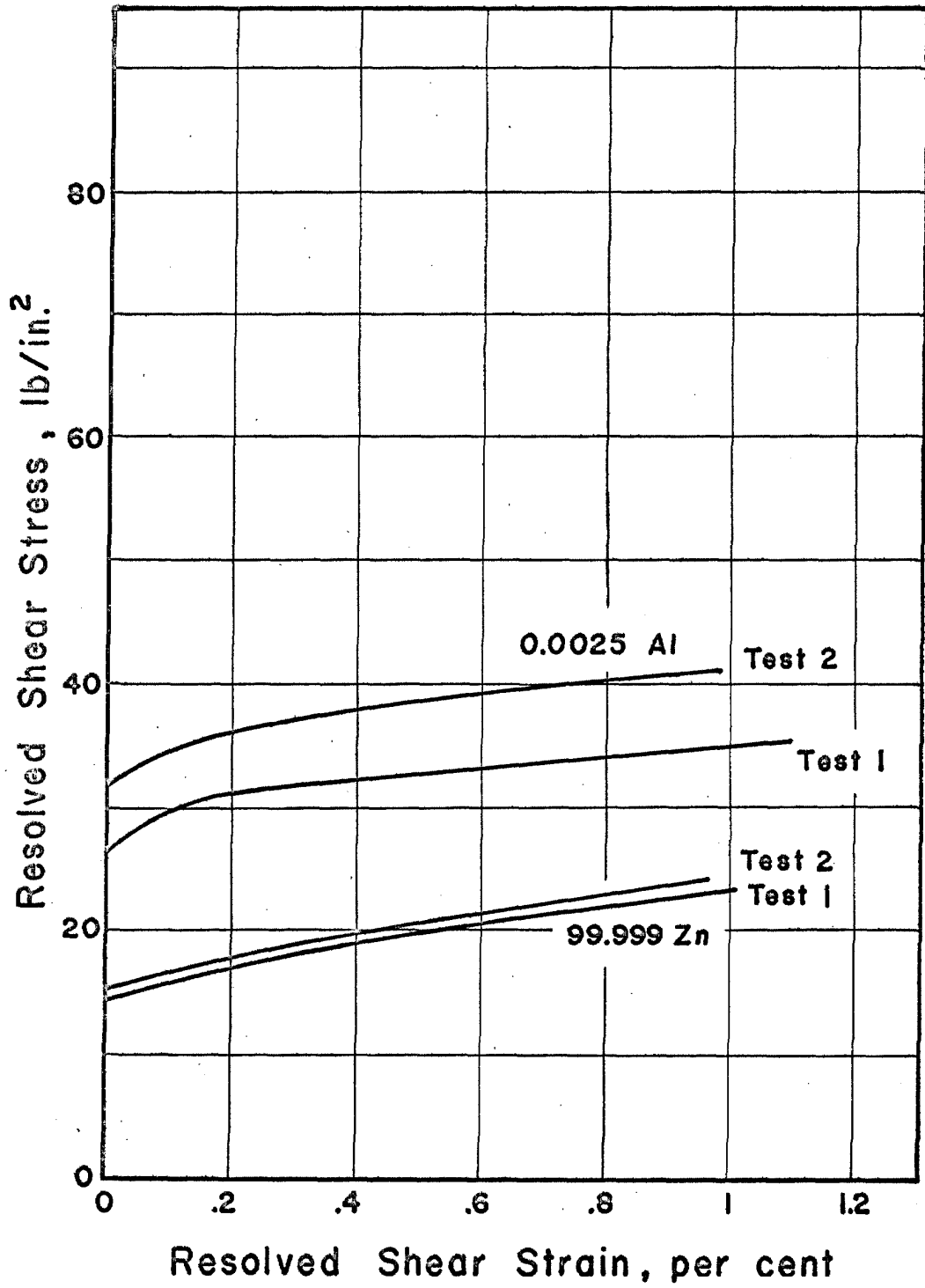
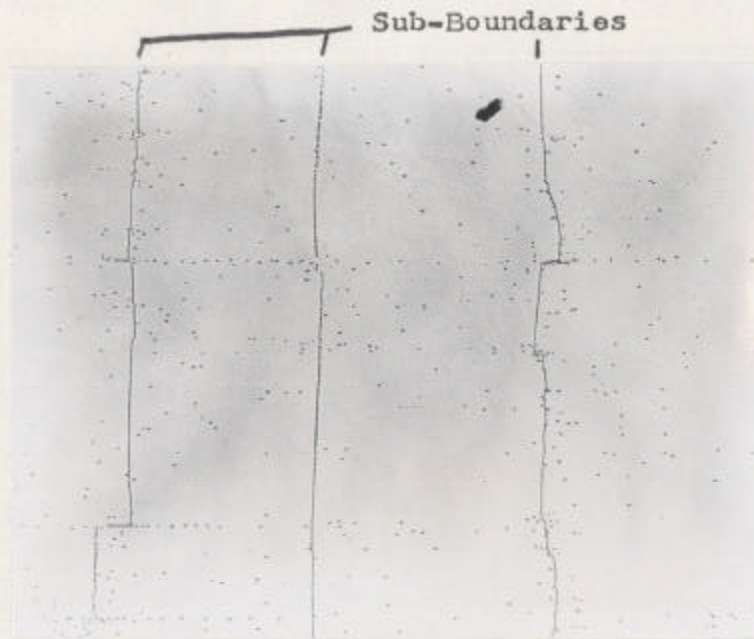
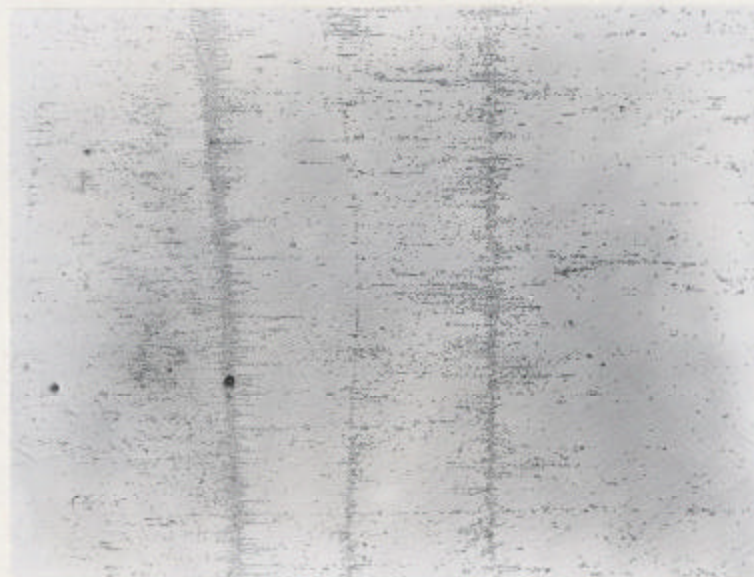


Fig. 30 Influence of Prior Strain on Basal Stress-Strain Curves.



(a) Random Area Before

(10 $\bar{1}$ 0)



(b) Random Area After

[$\bar{1}$ 2 $\bar{1}$ 0]

Fig. 31 Dislocation Density Changes Resulting from Basal Shear Strain of 1 Per Cent. Specimen 22-1T2, Zn-0.0025Al Purity, 100X.

An increase in dislocation density from $6.4 \times 10^4 \text{ cm}^{-2}$ to $1.1 \pm 0.2 \times 10^6 \text{ cm}^{-2}$ resulted from a shear strain of 1 per cent. The result on a 99.999 per cent purity specimen strained to 6.3 per cent is shown in Fig. 32. The initial dislocation density was approximately 10^5 cm^{-2} which increased to $2.7 \pm 0.3 \times 10^6 \text{ cm}^{-2}$. A distinct feature of the deformed specimens is that, in addition to an increase in density of randomly distributed dislocations, pile-ups of dislocations against substructure occur as can be seen in both Fig. 31 and 32. No significant difference in density increase for a given strain level ^{was} ~~were~~ noted between the various purities of zinc tested.

The results of measurements of changes in dislocation density produced by plastic strain are summarized in Table III. Figure 33 shows the basal slip system results plotted as the log of the dislocation density change against the log of the shear strain. The slope of the line drawn through the points is about 1/3 indicating a relation of the form

$$\Delta\rho = C \gamma_p^{\frac{1}{3}} \quad (6)$$

where

C = constant

$\Delta\rho$ = total change in density of dislocations

γ_p = plastic shear strain.



$(10\bar{1}0)$

$[\bar{1}2\bar{1}0]$

Fig. 32 Dislocation Density Resulting from Basal Shear Strain of 6.3 Per Cent. Specimen 16-1T3, 99.999 Per Cent Purity, 100X.

TABLE III

Dislocation Density Changes Produced by Plastic Strain

<u>Specimen</u>	<u>Purity per cent</u>	<u>Change in Dislocation Density, cm⁻²</u>	<u>Final Strain in./in.</u>
		<u>Basal</u>	
16-1T2	99.999	$4 \pm 0.8 \times 10^5$	3.6×10^{-4}
22-1T2	0.0025Al	$1.0 \pm 0.2 \times 10^6$	1×10^{-2}
16-4T3	99.999	$2.6 \pm 0.3 \times 10^6$	6.3×10^{-2}
		<u>Nonbasal</u>	
26-6T1	99.999	$3 \pm 1 \times 10^6$	9.0×10^{-4}

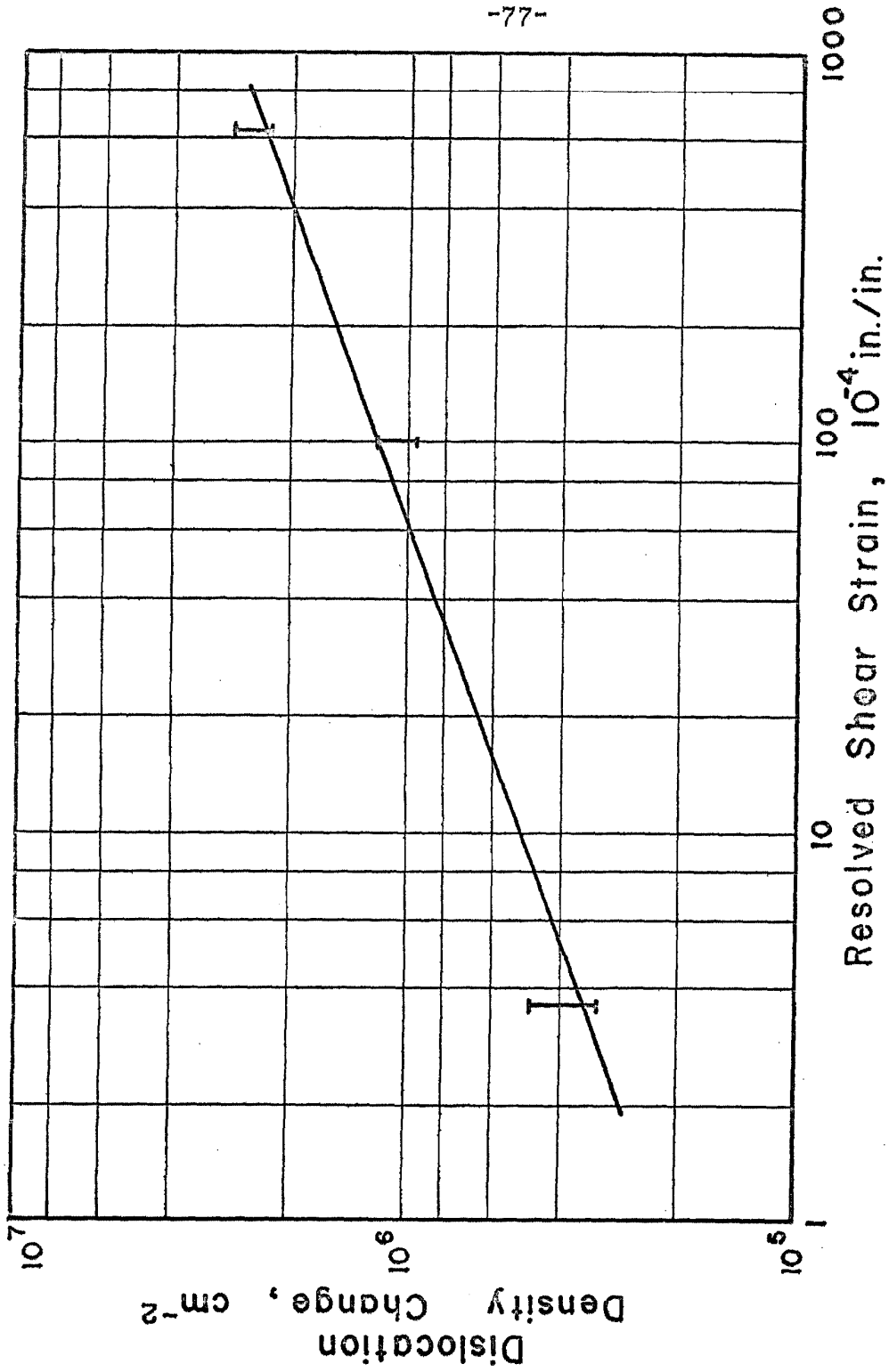


Fig. 33 Change in Dislocation Density vs. Shear Strain for Basal Slip.

Pulse Tests

A. Basal Slip System

Several test specimens of 99.999 per cent and zone refined purities were pulse loaded to determine basal dislocation mobility. The specimens were etched prior to testing to reveal the initial dislocation arrangement. Pulse load durations from 45 sec to 1 min were applied in the Instron static test system. The results on a zone refined specimen loaded to 9.9 lb/in.^2 resolved shear stress for 1 min are shown in Fig. 34. The scratch was made with a diamond phonograph stylus under 1.25 gm of contact force prior to etching and testing to introduce fresh dislocations. The dark spots are caused by bubbles in the replicas. As seen in Fig. 34, dislocations appear to have moved away from the scratched region and from the sub-boundary. A general increase in background dislocation density is seen as well as a number of long pile-ups of dislocations parallel to basal slip plane traces. These pile-ups are not associated with the deformation introduced by scratching. Several pile-ups were found to extend entirely across the prism surface of the test specimen. Mobility data could not be obtained from this test as dislocations moved too far to establish the location of the sources.

-79-

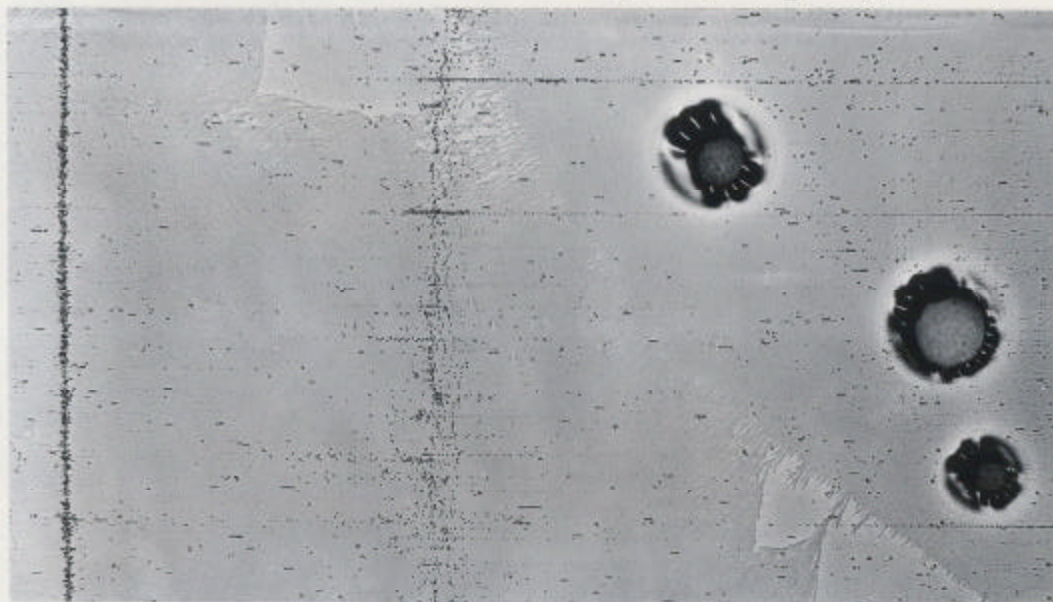
Sub-boundary



(a) Before

$(10\bar{1}0)$

$[\bar{1}2\bar{1}0]$



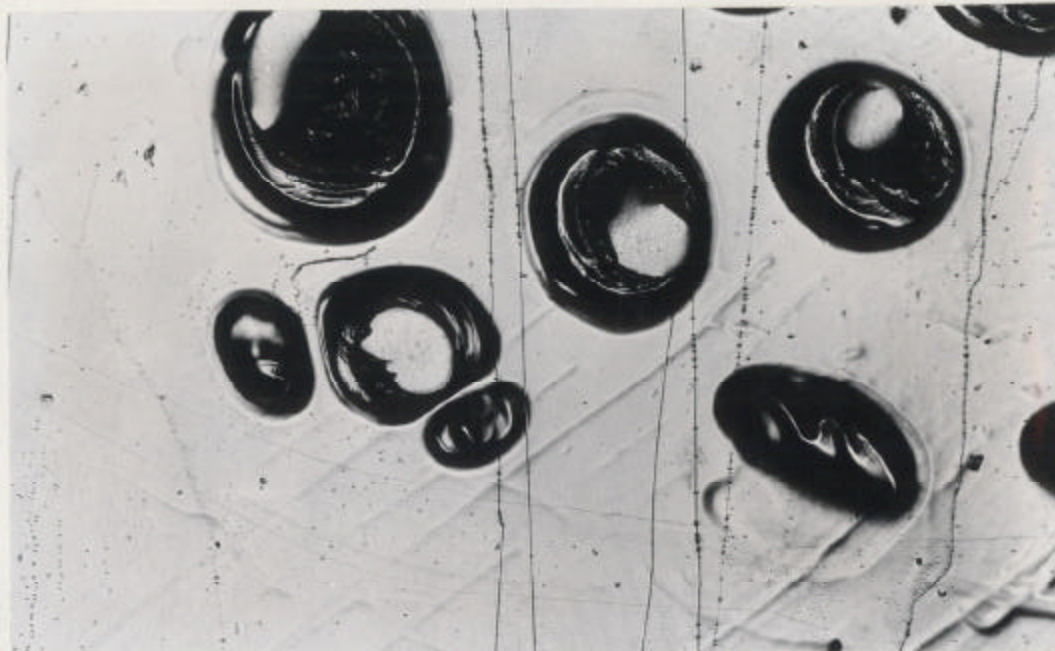
(b) After

Fig. 34 Basal Dislocations before and after a Pulse of 9.9 lb/in.². Specimen 17-3T3, Zone Refined Purity. 1 Min Pulse Duration, 100X.

Pulse tests on 99.999 per cent purity specimens were made at stresses of 7.7, 12.0, 15.4 and 20.3 lb/in.² for time durations of 45 sec. The test at 7.7 lb/in.², which is lower than the initial flow stress for 99.999 per cent purity material, indicated some local rearrangement of dislocations but no increase in dislocation density or formation of pile-ups. At progressively higher stresses, greater increases in dislocation density and numbers of pile-ups were observed. Mobility data was not obtained from the pulse tests on 99.999 per cent purity material because dislocation sources could not be established and because pile-ups were observed to extend across the entire specimen surface in all tests except the test at 7.7 lb/in.². In other words, the distance moved by an individual dislocation during the time duration of the applied stress could not be determined.

Pulse tests on specimens of 99.999 per cent and zone refined purities oriented for basal slip were conducted in the rapid load testing system. The specimens were scratched and etched before testing and re-etched within about three minutes after the pulse test. Tests were performed at resolved shear stresses from 7 to 19 lb/in.² and for times of 17, 34 or 51 x 10⁻³ sec. The same general result was found in these tests as in the

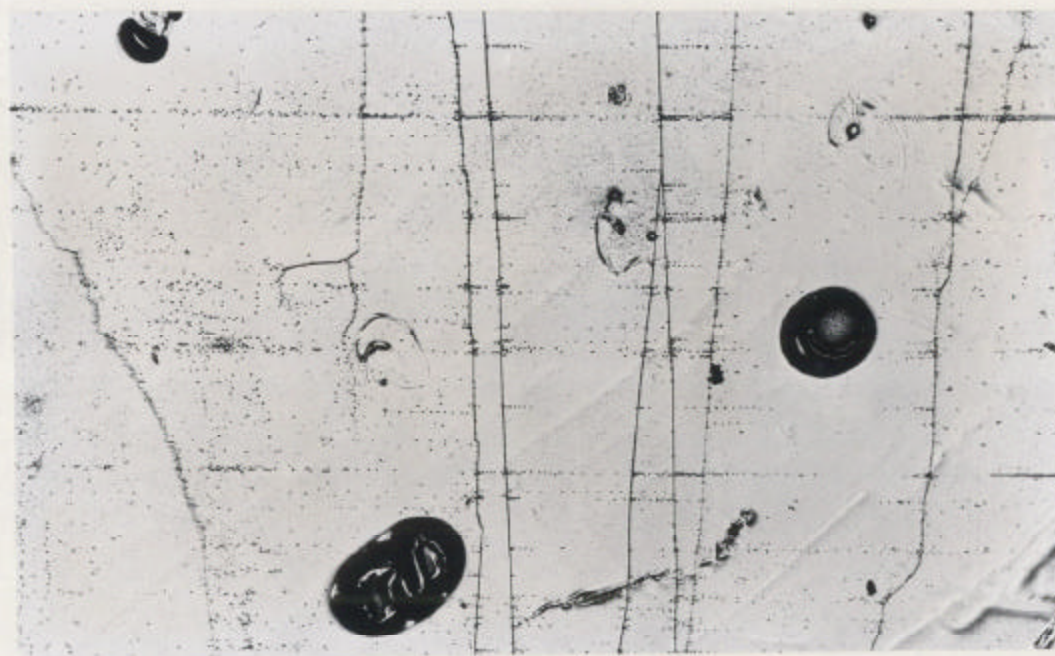
pulse tests conducted in the Instron system. Dislocation sources within the specimen or at the surfaces where the load was applied appeared to operate and cause dislocation pile-ups at the same stress levels that influenced the fresh dislocations produced by scratching or by thermal strain damage. This, in effect, prevented any one-to-one correspondence of before and after dislocation positions from being made. Long, extended pile-ups along basal slip plane traces were observed within the shear stress range of 7 to 19 lb/in.². Figure 35 shows the same region on a zone refined specimen before and after a pulse test of 15.5 lb/in.² for 17×10^{-3} sec. Pile-ups of dislocations against dislocation substructure can be seen. The longest pile-up found on either prism face is shown in Fig. 35 and is indicated by an arrow. The total length of this one pile-up was 0.78 cm with one end extending to the edge of the specimen corresponding to the surface of load application. By assuming that the dislocation source was located at the load surface and that the leading dislocation in the pile-up traversed the entire distance, a maximum dislocation velocity of 45.8 cm/sec was calculated for a shear stress of 15.5 lb/in.². A minimum velocity of 22.9 cm/sec would be obtained by assuming that the dislocation source was located at the center of the pile-up. In several



(a) Before

$(10\bar{1}0)$

$[\bar{1}2\bar{1}0]$



(b) After

Fig. 35 Basal Dislocations before and after a Pulse of 15.5 lb/in.². Specimen 17-4T1, Zone Refined Purity. 17×10^{-3} Sec Pulse Duration, 100X.

tests, dislocation pile-ups were observed on both $(10\bar{1}0)$ surfaces of the test specimen that appeared to be associated with the same basal slip plane.

The results of a series of tests on 99.999 per cent purity specimens are shown in Fig. 36. Log velocity has been plotted against log resolved shear stress. Points labelled with a caret (\wedge) are measurements on pile-up lengths that extended across the entire specimen face and hence are to be regarded as lower limits for the velocity at the corresponding stress level. The points in Fig. 36 without a caret represent pile-up lengths that extended from a load surface into the specimen. Each point represents the maximum velocity calculated for a given test and hence involves the maximum length of all the observed dislocation pile-ups.

Figure 36 shows a considerable scatter in the experimental data. A straight line has been drawn through the points representing the maximum observed velocity for a given stress level. The straight line indicates that the data can be represented by an empirical relation of the form

$$v = \left(\frac{\tau}{\tau_0} \right)^n \quad (7)$$

where

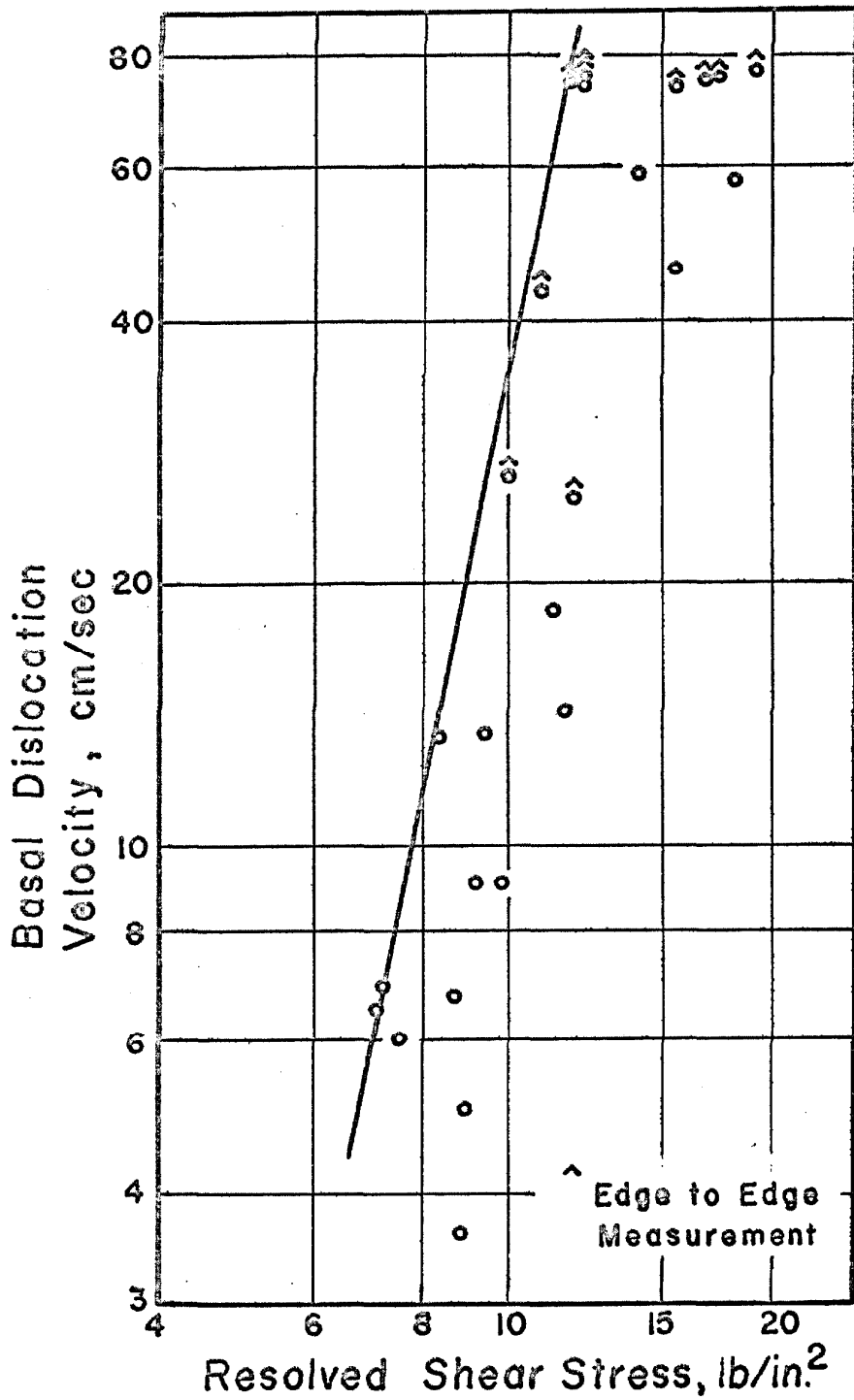


Fig. 36 Basal Dislocation Velocity vs. Resolved Shear Stress for 99,999 Per Cent Purity Specimens.

τ = applied shear stress

$n = 5$

τ_0 = the shear stress which produces a velocity of 1 cm/sec and is 5 lb/in.².

Several sources of error existed that may explain the scatter observed. One of the uncertainties was the location of the source of the dislocation pile-up and another was introduced in the process of measuring the pile-up lengths because the location of the end point of a pile-up was not always clear.

The data plotted in Fig. 36 is shown plotted as log velocity against $\tau - \tau_i$ in Fig. 37. A value of 6 lb/in.² was taken for τ_i which is the lowest stress at which any dislocation motion was observed. A straight line has been drawn through the maximum velocity points which represents a function of the form

$$v = C e^{\frac{\tau - \tau_i}{B}}$$

where

C = constant

$B = 1.45 \text{ lb/in.}^2$.

B. Nonbasal Slip System

Pulse load tests were conducted in the rapid load testing system on several 99.999 per cent purity specimens oriented for nonbasal slip to determine the

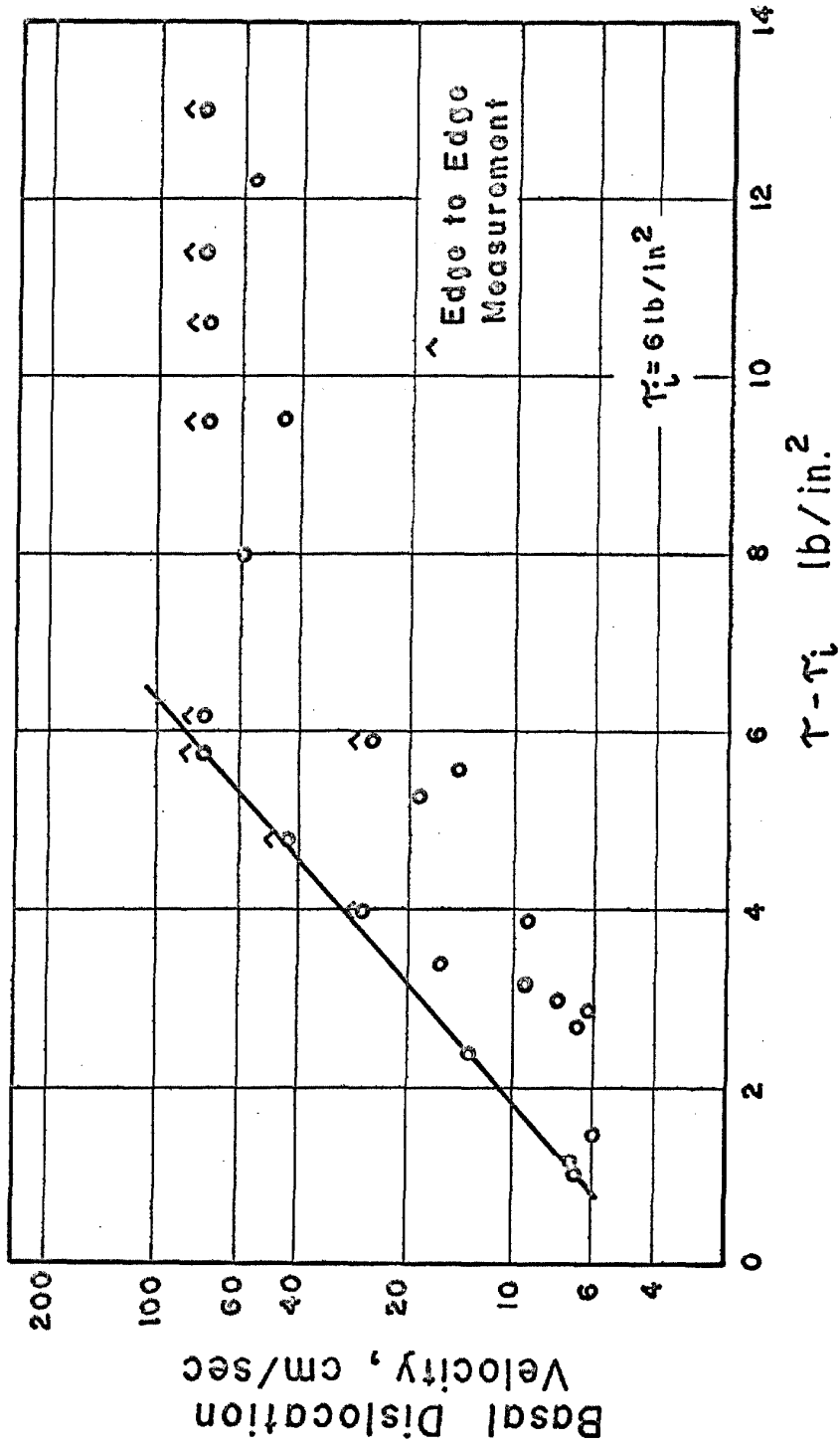
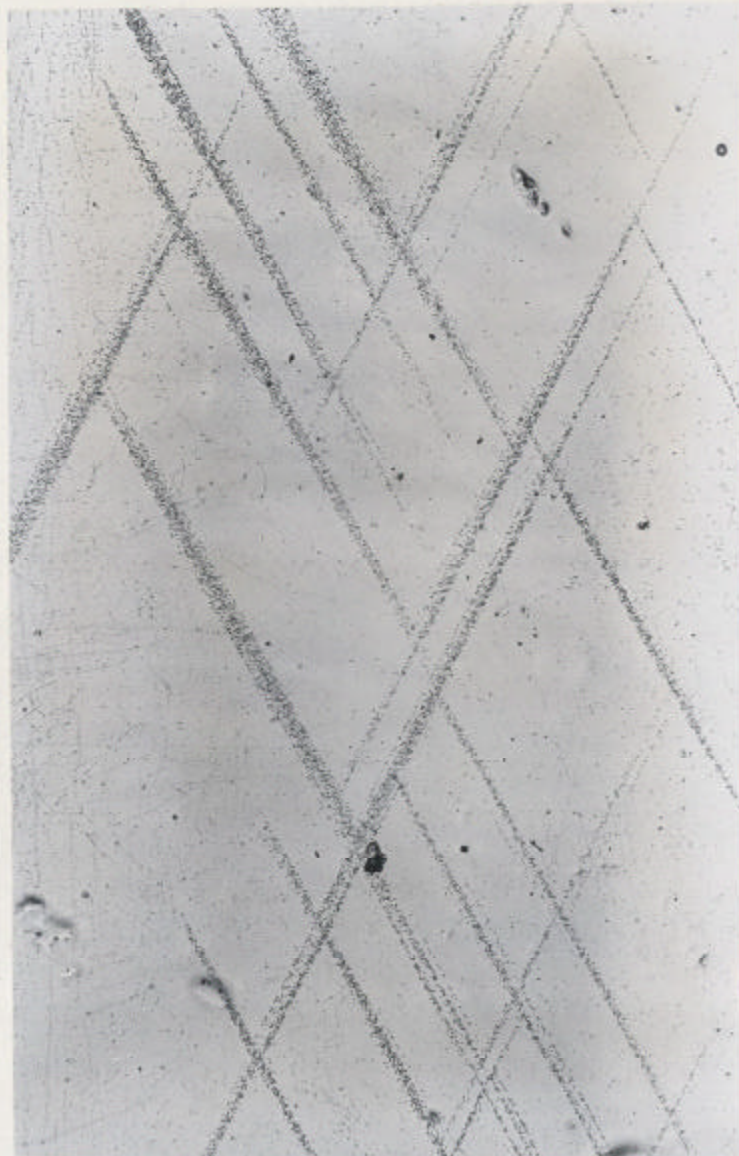


Fig. 37 Basal Dislocation Velocity vs. $\tau - \tau_i$

mobility of nonbasal dislocations in the $[\bar{1}\bar{2}1\bar{3}]$ ($1\bar{2}12$) slip system. A uniaxial stress parallel to the c-axis of the test specimens ranging from 390 to 2010 lb/in.² was applied for times ranging from 51×10^{-3} to 33 sec. The specimens were etched before and re-etched within three minutes after testing to establish any changes in background dislocation density as well as changes in regions where the specimen had been scratched to produce fresh dislocations. No significant generation of dislocations occurred near scratches in any of the tests conducted. Deformation bands occurred at compressive stresses in excess of 790 lb/in.² whereas none were found between 390 and 690 lb/in.² in load durations from 6.2 to 33 sec. Figure 38 is a photograph of the slip bands produced at a compressive stress of 970 lb/in.² or 405 lb/in.² resolved in the $[\bar{1}\bar{2}1\bar{3}]$ ($1\bar{2}12$) system. The load duration was 31.4 sec. The slip bands seen in Fig. 38 are oriented along traces of the $\{1\bar{2}12\}$ slip planes on the prism surface of the test specimen. No significant increase in background density was noted, other than the formation of slip bands containing high densities of dislocations.

The mobility of nonbasal dislocations was calculated from the longest length of new slip band produced at a given stress by assuming that the dislocations with the

Traces of $\{1\bar{2}12\}$



Compression
Axis

$(10\bar{1}0)$

$[\bar{1}2\bar{1}0]$

Fig. 38 Nonbasal Slip Bands Resulting from c-Axis
Compressive Stress of 970 lb/in.². Specimen
16-4T6, 99.999 Per Cent Purity. 31.4 Sec Pulse
Duration, 100X.

maximum velocity moved one-half the total length of the slip band during the duration of the test. This is equivalent to assuming that the dislocation sources are located at the center of the bands. The experimental data is shown in Fig. 39 plotted as log velocity against log stress resolved in the $[\bar{1}\bar{2}1\bar{3}]$ ($1\bar{2}12$) nonbasal slip system. The straight line drawn through the points corresponds to a power law relation of the form

$$v = \left(\frac{\tau}{\tau_0} \right)^n \quad (8)$$

where

$$n = 9.5$$

τ_0 = the resolved shear stress which produces a velocity of 1 cm/sec and is 790 lb/in.².

Strain-Rate Sensitivity of the Flow Stress

A. Basal Slip System

The indirect method of determining the mobility relation involves the inverse strain-rate sensitivity of the flow stress. Two different functional relations between the plastic strain rate, $\dot{\gamma}_p$, and the applied shear stress were employed in analyzing the variable strain-rate data. The first relation assumes a power law dependence of the form

$$\dot{\gamma}_p = C \tau^{n'} \quad (9)$$

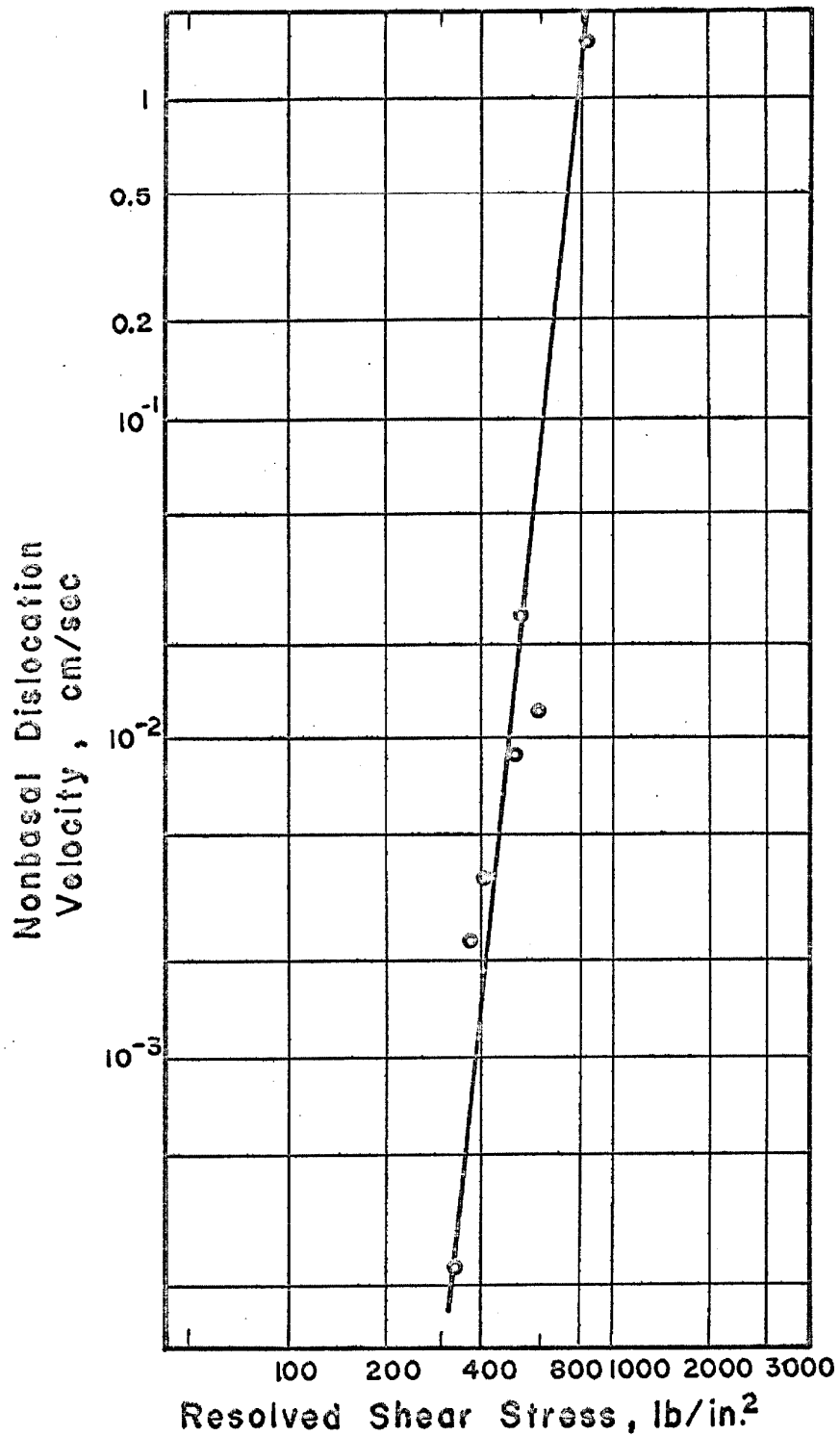


Fig. 39 Nonbasal Dislocation Velocity vs. Resolved Shear Stress for 99.999 Per Cent Purity Specimens.

where C is a constant. The inverse strain-rate sensitivity from Eq. 9 is given by

$$n' = \frac{\partial \ln \dot{\gamma}_p}{\partial \ln \tau} \quad (10)$$

or

$$n' = \frac{\ln \frac{\dot{\gamma}_{p_2}}{\dot{\gamma}_{p_1}}}{\frac{\Delta \tau}{\tau}}$$

in terms of the strain-rate after the change, $\dot{\gamma}_{p_2}$, and that imposed prior to the change, $\dot{\gamma}_{p_1}$. $\Delta \tau$ is the jump in stress accompanying the change and is much less than the shear stress, τ . The values for n' calculated from the experimental data are given in Table IV for specimens of four different purities ranging from zone refined to 0.02 wt per cent aluminum. For each test, the mean value for n' has been listed along with the standard deviation from the mean. Specimen 17-2T1 showed a somewhat linear increase in n' with strain ($n' = 50$ to 10^4) but no such variation was found for the other tests conducted. No significant difference was found between the values of n' calculated from increasing changes and decreasing changes in strain-rate and between the various purities of zinc tested.

TABLE IV

Summary of Variable Strain-Rate Data

Specimen	Purity	Synchro- nous Speed, 10^{-3} in./ min	Final Strain per cent	$n' \pm \sigma$	$m' \pm \sigma$
<u>Basal</u>					
17-2T1	Zone Refined	1	1.2	50-104*	1.71 \pm 0.28
16-4T2	99.999	1	1	77 \pm 17	1.91 \pm 0.46
16-4T3	99.999	5	6.3	90 \pm 20	2.04 \pm 0.30
22-1T1	0.0025A1	1	1.1	90 \pm 25	1.56 \pm 0.10
22-1T2	0.0025A1	1	1	136 \pm 20	1.65 \pm 0.30
19-3T2	0.02A1	1	1.2	78 \pm 20	1.06 \pm 0.23
<u>Nonbasal</u>					
25-1T1	99.999	2	800×10^{-6} in./in.	720 \pm 10	-

*Linear function of strain.

The second relation used in analyzing the strain-rate sensitivity data assumes that the strain-rate is related to the difference between the applied stress and the flow stress at zero strain-rate, τ_i , or

$$\dot{\sigma}_p = C(\tau - \tau_i)^{m'} \quad (11)$$

The exponent m' is given as

$$m' = \frac{\partial \ln \dot{\sigma}_p}{\partial \ln (\tau - \tau_i)} \quad (12)$$

or

$$m' = \frac{\ln \dot{\sigma}_{p2} / \dot{\sigma}_{p1}}{\ln \left(\frac{\tau_2 - \tau_i}{\tau_1 - \tau_i} \right)}$$

where τ_2 is the stress immediately after the strain-rate change and τ_1 is the stress immediately prior to the strain-rate change. Measurements of the load immediately before the "machine on" part and after the "machine off" part of the strain-rate cycles were used to determine the values of τ_i for a given set of strain-rate changes. Figure 40 shows schematically a typical load-time curve obtained experimentally. The load jumps resulting from increasing changes in cross-head speed, \dot{y} , are shown as δ_0 , δ_1 and δ_2 . The stress difference ratios are then given as

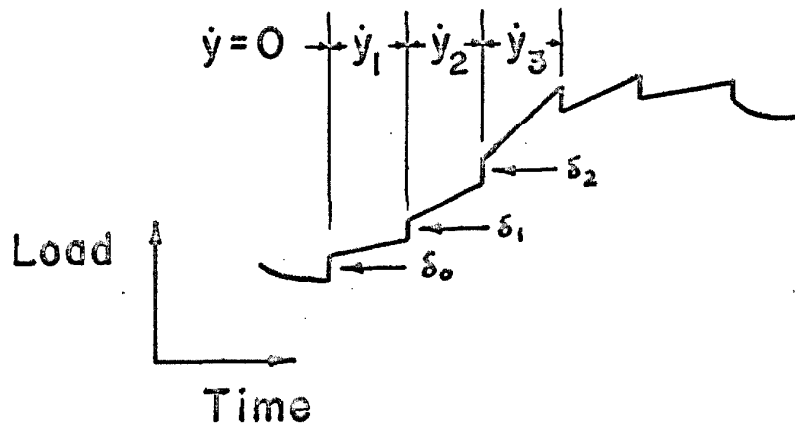


Fig. 40 Schematic Load-Time Curve.

$$\frac{\tau_2 - \tau_i}{\tau_1 - \tau_i} = \frac{\delta_0 + \delta_1}{\delta_0}$$

and

$$\frac{\tau_3 - \tau_i}{\tau_2 - \tau_i} = \frac{\delta_0 + \delta_1 + \delta_2}{\delta_0 + \delta_1}$$

The values of m' calculated from the experimental data are given in Table IV as mean values and standard deviations from the mean. [No significant differences were found in the values of m' calculated for four different purities of zinc except for the test on a specimen of Zn-0.02Al purity.]

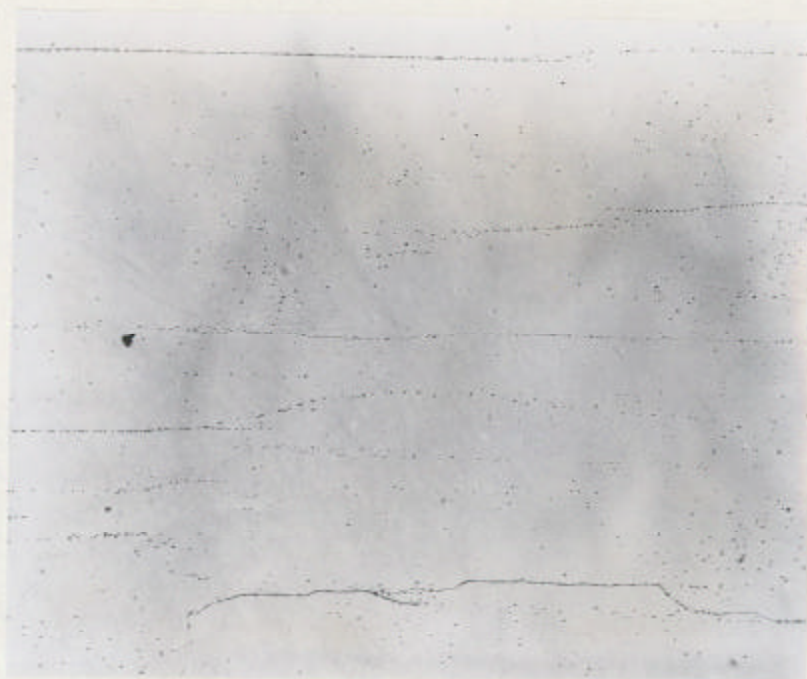
B. Nonbasal Slip System

A variable strain-rate test on a c-axis specimen was conducted at crosshead speeds in the ratio of $1/\frac{1}{10}/0$ and a maximum crosshead speed of 0.002 in./min. The strain-rate sensitivity of the flow stress for nonbasal slip was found to be considerably less than that for basal slip. The value for n' calculated from the experimental data is given in Table IV. The flow stress at zero strain-rate, τ_i , could not be determined because of a large uncertainty in the value of δ_0 which resulted from the very small strain-rate sensitivity.

Influence of Impurity and Strain on Dislocation Sub-
structure

In the course of etching and examining single crystal specimens of four different purities of zinc, several observations were made regarding the influence of aluminum impurity on the type of dislocation substructure and degree of impurity segregation found in single crystals. Figure 31 illustrates the general type and density of substructure found in single crystals of zone refined, 99.999 per cent and Zn-0.0025Al purities. The substructure is for the most part perpendicular to the basal plane trace on the etched prism surface of the specimen. Upon closer examination, the substructure is found to consist of closely spaced dislocations which are most likely basal dislocations of pure edge character as shown by Brandt, Adams and Vreeland (22). Such substructure would then be characterized as small angle tilt boundaries. The general type of substructure found in specimens of Zn-0.02Al purity differed from that found for the other purities. Figure 41 shows an etched prism surface where the substructure can be seen to be oriented more or less parallel to the basal plane trace.

Examples of macroscopic impurity segregation were found in specimens of Zn-0.02Al and Zn-0.0025Al purities.

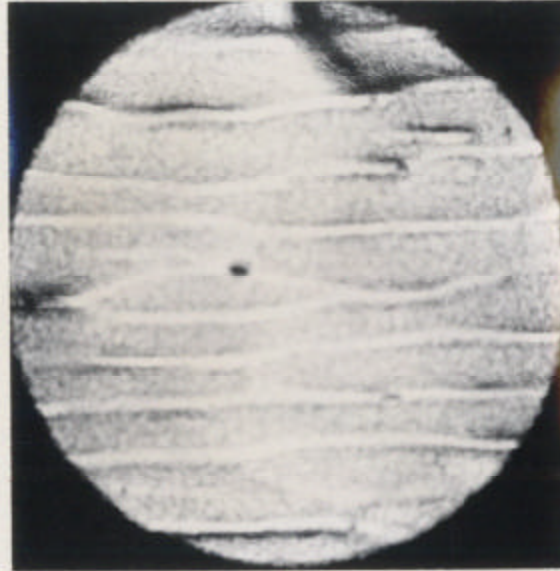


$(10\bar{1}0)$ $[\bar{1}2\bar{1}0]$

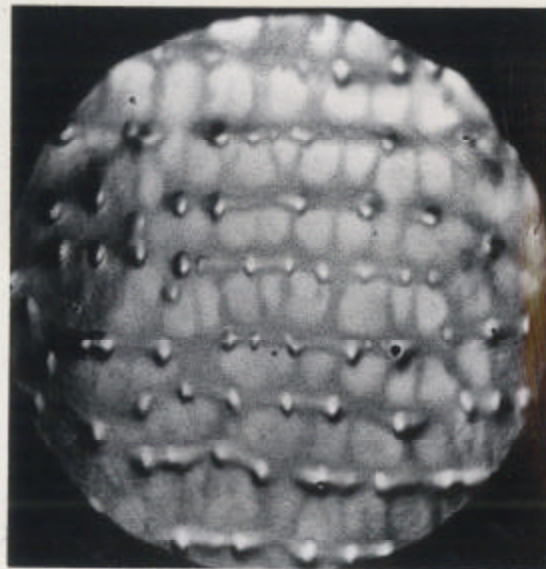
Fig. 41 Dislocation Substructure in Zn-0.02Al Specimens.
Specimen 19-1, 100X.

The segregation structure as revealed on a polished and etched prism and transverse faces of a 45° compression test specimen ^{of Zn-0.02Al} is shown in Fig. 42⁹. The growth direction for the specimen shown in Fig. 42⁹ was almost parallel to the prism surface and within about 10° to the basal plane trace. Impurities have segregated to form the elongated cellular structure with the cell axes oriented along the growth direction. Comparison of Figs. 41 and 42 illustrates the relation between impurity segregation and dislocation substructure as observed in specimens of Zn-0.02Al purity. The dislocation substructure can be seen to correspond to the cellular boundaries formed by the impurity segregation.

Figure 43¹⁰ shows the segregation substructure as revealed on a prism face of a Zn-0.0025Al specimen. A cellular structure oriented along the crystal growth direction was observed as in the case of Zn-0.02Al specimens. However, no correlation between impurity segregation and dislocation substructure was found in the Zn-0.0025Al crystal. Figure 43¹⁰ shows the characteristic tilt boundary substructure with no apparent relation to the impurity segregation substructure. Table V summarizes the observations made on impurity segregation and dislocation substructure.



(a) Prism Surface $\overline{[12\bar{1}0]}$



(b) Transverse Surface of 45° Specimen

Fig. 42 Impurity Segregation in Zn-0.02Al Specimens.
Specimen 19-3, 25X.

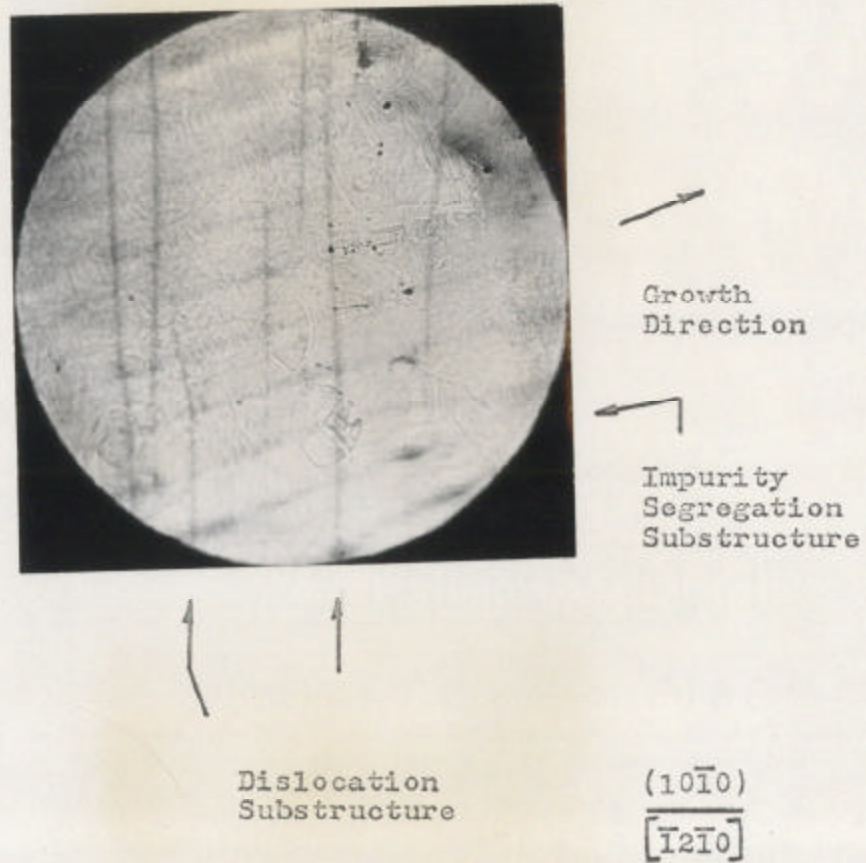


Fig. 43 Dislocation Substructure and Impurity Segregation in Zn-0.0025Al Specimens. Specimen 22-1, 25X.

TABLE V

Summary of Effect of Purity on Substructure and Nonbasal Dislocation Density

Purity per cent	Substructure Character	Impurity Segregation into Cells	Nonbasal Dislocation Density cm^{-2}
Zone Refined	Perpendicular to basal planes	No	-
99.999	Perpendicular to basal planes	No	4.2×10^3 10×10^3
Zn-0.0025Al	Perpendicular to basal planes	Yes	89×10^3
Zn-0.02Al	Parallel to basal planes	Yes	210×10^3

Several specimens of each purity were cleaved and etched with Rosenbaum's Etch (20) to reveal nonbasal dislocation intersections with the basal plane. An example of the etch pit density on a Zn-0.02Al specimen is shown in Fig. 44. The results of nonbasal etch pit counts are tabulated in Table V. An increase in nonbasal dislocation density was observed with increasing impurity levels. *the uncertainty in etch pit density is about a factor of 2, since such a variation could be found from crystal to crystal, and in different regions of a given crystal.*

Plastic strain was observed to have an effect on the density of substructure in specimens which had been strained and annealed. Figure 45 illustrates the tilt boundary density in a specimen after 30 per cent basal shear strain followed by annealing at 700°F for 4 hr. The tilt boundary density seen in Fig. 45 is about three to four times that found in undeformed specimens of the same purity.

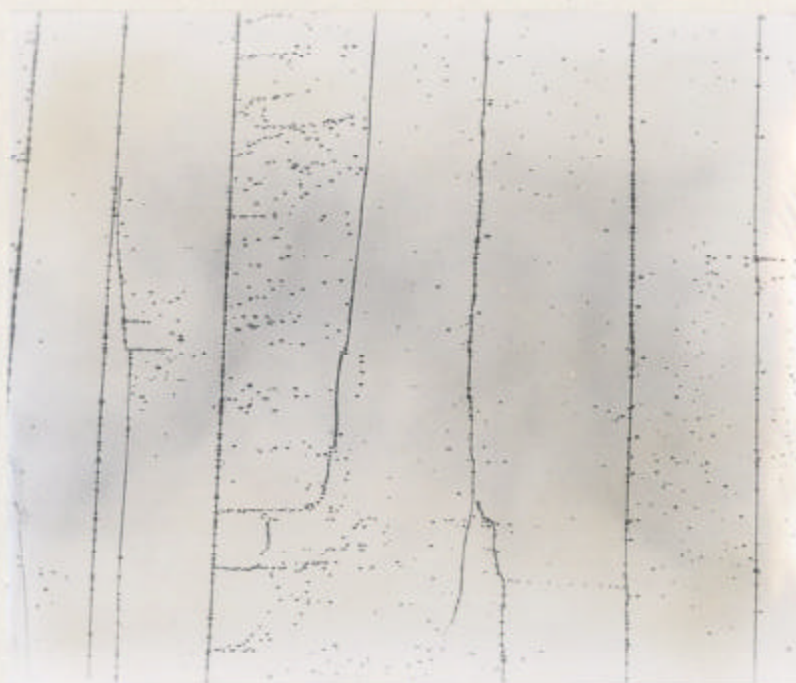
Dislocation Pile-Ups

An experiment was conducted to establish whether the dislocation pile-up configurations observed on specimens deformed in basal slip were truly representative of the deformed structure of the specimen before the stress was removed. A 99.999 per cent purity specimen was etched and replicated prior to the application of a load corresponding to a resolved shear stress of 12.1 lb/in.². The load was held constant while the



(0001) $[\bar{1}2\bar{1}0]$ |

Fig. 44 Nonbasal Dislocation Density Revealed on the Basal Plane of a Zn-0.02Al Purity Specimen. Density - $2.1 \times 10^5 \text{ cm}^{-2}$, 100X.



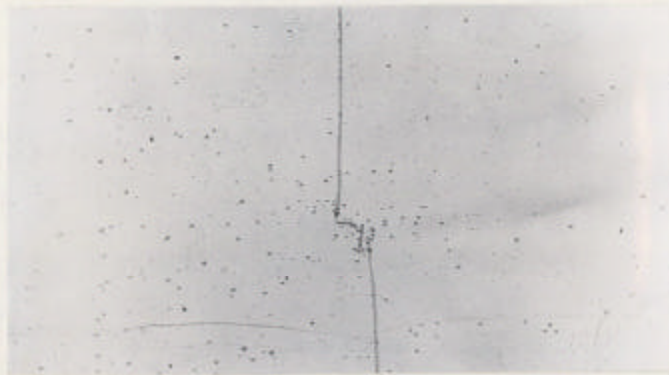
(10 $\bar{1}$ 0)

$\overline{[12\bar{1}0]}$

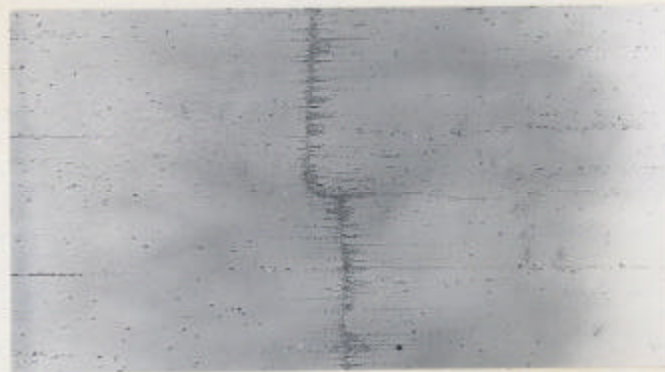
Fig. 45 Dislocation Substructure after 30 Per Cent Shear Strain and Anneal. Specimen 16-3, 99.999 Per Cent Purity, 100X.

specimen was re-etched and then the load was removed. Prism surfaces were replicated and again the specimen was re-etched and replicated. Figure 46 shows the dislocation distribution in identical regions of the specimen before application of stress, under stress and after the stress was removed. A large number of pile-ups against a tilt boundary can be seen but few changes in either the number of pile-ups or their length have occurred between the stressed and unstressed states.

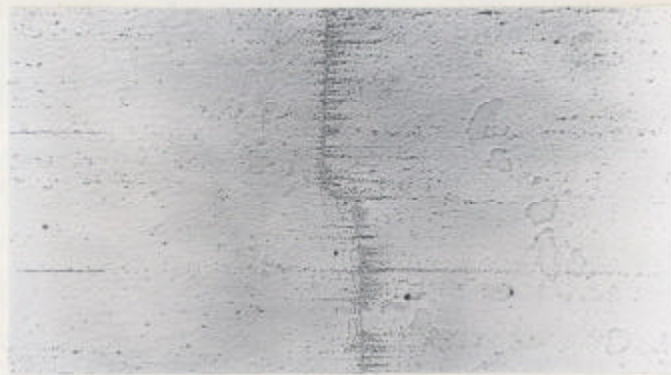
-106-



(a) Before



(b) Under Stress



(c) Unstressed

Fig. 46 Effect of Stress Unloading on Basal Dislocation Pile-Ups. Shear Stress = 12.1 lb/in.². Specimen 18-1, 99.999 Per Cent Purity, 100X.

VI. DISCUSSION OF RESULTS

The stress-strain behavior of zinc single crystals has been found to be drastically different depending on whether the crystal deforms in basal or nonbasal slip. A low critical resolved shear stress and work-hardening rate are characteristic of basal slip as compared to nonbasal slip which confirms the work of Stofel (23). The differences between basal and nonbasal slip can be understood in terms of the basic relation given by Eq. 3 if the dislocation mobility relation and rate of dislocation multiplication with strain are known for each mode of deformation. Etch pit observations can be used to establish the most likely dislocation mechanisms responsible for the observed values of flow stress and work-hardening rate.

Basal Slip System

A. Dislocation Orientations

The dislocations observed after pulse tests on specimens oriented for basal slip are most likely close to the edge orientation. The specimen orientation is such that dislocations with a Burgers vector in the $[\bar{1}2\bar{1}0]$ direction will experience a force per unit length equal to γa where a is a lattice parameter and γ is the applied shear stress. This force acts normal to the dislocation line. Dislocations with Burgers vectors

at 60° to the $[\bar{1}2\bar{1}0]$ will experience a force per unit length equal to $\frac{1}{2}\tau a$. Etch pits were observed on the $(10\bar{1}0)$ surfaces of the test specimens parallel to the $[\bar{1}2\bar{1}0]$. Therefore, edge dislocations with a $[\bar{1}2\bar{1}0]$ Burgers vector make a perpendicular intersection with etched surfaces and screw dislocations with the same Burgers vector lie parallel to the etched surfaces.

The mobility of basal screw dislocations is of the same order of magnitude as that of basal edge dislocations for the same stress levels at very low strains. This is deduced from the observation that in several pulse tests, pile-ups observed on one of the $(10\bar{1}0)$ surfaces of the test specimen were located on the same slip plane as pile-ups observed on the other $(10\bar{1}0)$ surface within the limit of measurement accuracy. This observation suggests that dislocation loops expand in a slip plane with the edge and screw dislocation components of the loop traveling at about the same rate. This result is different from that found for lithium fluoride (11) and silicon-iron (25) where edge dislocation velocities are much greater than screw velocities at the same stress level.

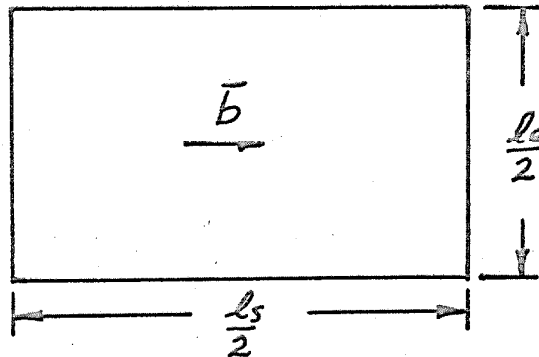
The results of the variable strain rate tests undoubtedly involve both edge and screw dislocations with $[\bar{1}2\bar{1}0]$ Burgers vectors. If this is taken into

account, Eq. 3 should be written as

$$\dot{\gamma}_p = \rho_e b v_e + \rho_s b v_s \quad (13)$$

where v_e and v_s are the velocities of edge and screw dislocations respectively.

The effect on strain-rate of different edge and screw velocities at relatively large strains may be taken into account by the following model. Assume that an infinitesimally small square dislocation loop is formed by some means and that in time t it expands to the size shown below



l_e = total length of edge dislocation

l_s = total length of screw dislocation.

The lengths of edge and screw dislocation formed in time t are

$$l_s = 4 v_e t$$

$$l_e = 4 v_s t$$

which gives the relation

$$\frac{L_s}{l_e} = \frac{v_e}{v_s} \quad \text{or} \quad \frac{\rho_s}{\rho_e} = \frac{v_e}{v_s} .$$

Equation 13 may now be written as

$$\begin{aligned} \dot{\gamma}_p &= \rho_e b v_e + \rho_s b \left(\frac{\rho_e}{\rho_s} v_e \right) \\ &= 2 \rho_e b v_e . \end{aligned}$$

This result shows that the strain-rate can be related to $\rho_e v_e$ alone even if $\rho_s \neq \rho_e$ and $v_s \neq v_e$. Therefore the indirect method may be used to determine the mobility relation for edge dislocations when both edge and screw dislocations are contributing to the strain.

B. Dislocation Multiplication and Density Changes

The results of the pulse tests indicate that basal dislocations moved long distances and, in some cases, out of the specimen at stress levels near the macroscopic flow stress as determined by stress-strain tests. Each dislocation pile-up ^{against a sub boundary} shown in Fig. 35 appears to be on a single slip plane. These individual pile-ups appear to be associated with other pile-ups on the same slip plane. These observations imply that one very active dislocation source was responsible for an entire

slip line involving hundreds of individual dislocations. Dislocation multiplication of this type would be characteristic of a Frank-Read source located at the surface or within the crystal. In almost all cases the pile-ups were observed to extend from a loaded surface of the specimen which indicates that surface sources are probably more important than volume sources. This may be due to stress concentrations on the surface where the load is applied. In addition, surface sources of a given length are able to generate dislocations at half the stress level of volume sources of the same length. This is a result of "image forces" on a dislocation near a free surface.

Figure 33 gives the results of several determinations of the change in total dislocation density accompanying shear strain. The relation $\Delta\rho = C\delta_p^{\frac{1}{3}}$ for zinc differs from the experimentally determined relations $\Delta\rho = B + C \log \epsilon_p$ for copper (26) and $\Delta\rho = C\delta_p$ for stage I deformation of silver (27), and lithium fluoride (11). The relation found for zinc is less dependent on shear strain than the relation reported for silver. This indicates a relatively high probability that a glide dislocation in zinc will reach the surface and therefore contribute to the strain but not to the etch pit density. The mean travel distance

of glide dislocations in zinc can be of the order of $1/4$ in. as determined by the pulse load tests. This is in agreement with a speculation made by Mott (28) that large numbers of basal dislocations in hexagonal close-packed crystals might be able to leave a specimen and thus would not be able to influence the flow stress by interaction with other dislocations.

The experimentally determined basal dislocation density changes given in Table III are numerically equal to the total etch pit density counts observed on the $(10\bar{1}0)$ prism surfaces of the test specimens. As explained in the derivation of Eq. 3, the number of dislocations per unit area is equal to the total length of dislocation line per unit volume if all basal dislocations are straight and perpendicular to the area of observation. A better approximation may be that that the basal dislocations are randomly oriented with respect to the observation surface. The relation between observed etch pit density and total line length of basal dislocation per unit volume, ρ , is then

$$\rho = 0.64 \Lambda$$

from equations developed by Schoeck (29).

C. Thermally Activated Dislocation Motion

Figure 37 shows the dislocation mobility data plotted as log velocity against $T - T_i$ where T_i was taken as 6 lb/in.² or the lowest stress at which dislocations were observed to move in 99.999 per cent purity crystals. The slope from Fig. 37 gives $B = 1.45$ lb/in.² where B is defined by

$$v = C e^{\frac{T - T_i}{B}} \quad (14)$$

This form for the mobility relation would be expected if the rate determining mechanism was the thermal activation for a glide dislocation to pass some obstacle in the glide plane. Seeger, Mader and Kronmuller (30) and Friedel (31) have considered this problem and both believe that the flow stress for basal glide in hexagonal close-packed crystals is determined by the stress required to overcome the "long-range internal stresses" produced by parallel glide dislocations and by the thermal activation of jogs as basal dislocations glide past forest dislocations threading the glide plane. The strain-rate resulting from thermal activation of jogs is given by Friedel as

$$\dot{\gamma}_p = \rho_m v \left(\frac{b}{l}\right)^2 A e^{-\left[\frac{\Delta U - (T - T_i) b d l}{kT}\right]} \quad (15)$$

where

ΔU = energy required to produce the jog

τ = applied shear stress

τ_i = long-range internal shear stress

d = separation of extended basal dislocations

l = forest spacing

A = area of slip plane swept over by dislocation after jog is formed

ν = Debye frequency.

The velocity of a dislocation is then given by

$$v = \nu \left(\frac{b}{l}\right)^2 A e^{-\frac{\Delta U}{kT}} e^{\frac{\tau - \tau_i}{B}} \quad (16)$$

where

$$B = \frac{kT}{bdl}$$

The forest spacing l for the crystals used in this investigation can be estimated from the etch pit density observed on basal planes and given in Table V. With a forest density of about (10^4 cm^{-2}) , the forest spacing, l , is 10^{-2} cm for 99.999 per cent purity material. B is then equal to 2.5×10^{-3} lb/in.² if d is taken as $7b$ (32). This value of B is considerably lower than the directly determined value of 1.45 lb/in.². This lack of agreement shows that a model based on the thermal

activation of jogs is incapable of explaining the observed dislocation mobility.

One reason the above model is not correct can be seen by comparing the terms ΔU and $(\tau - \tau_i) b d l$ in the exponential term of Eq. 15. For an applied shear stress of 16 lb/in.², $(\tau - \tau_i) b d l \approx 120 \text{ eV}$ for the forest spacing observed and a long-range internal stress of about 6 lb/in.² which is the lowest stress at which basal dislocations were observed to move long distances. ΔU has been estimated by Friedel (32) to be

$$\Delta U = \frac{9b^2d}{30} .$$

ΔU is then about 1eV for basal dislocations in zinc. This result means that the applied stress is more than sufficient to supply the jog energy required and thus no assistance from the thermal energy of the lattice is required.

Equation 16 predicts that in the limit as $(\tau - \tau_i) b d l$ approaches ΔU , the velocity of a dislocation will approach $v \left(\frac{b}{\rho}\right)^2 A$ which is approximately equal to $v b^2$. For basal dislocations in zinc single crystals $v b^2 \approx 7 \times 10^{-4}$ cm/sec. This velocity is much lower than the velocities measured in the present work and indicates that all thermally activated mechanisms which predict dislocation velocities of a form similar to

Eq. 16 will not explain the present results. The thermal activation of glide dislocations past impurity atoms (4) is one such mechanism and as such can be eliminated as a controlling factor in the present work.

D. Dislocation Mobility in Other Materials

Figures 36 and 39 show that the direct mobility data for zinc may be appropriately represented as $v = \left(\frac{\tau}{\tau_0} \right)^n$ where τ_0 equals the stress to move a dislocation at 1 cm/sec. Mobility data on other materials has been found to fit this same form with different values for n and τ_0 . A summary of τ_0 and n for zinc as well as other materials is given in Table VI. The large differences between the values of τ_0 are to be expected from the differences in atomic bonding and crystal structure. The materials listed in Table VI include ionic bonding (lithium fluoride and sodium chloride), covalent bonding with diamond cubic structure (germanium) and metallic bonding with body-centered cubic structure (silicon-iron and tungsten). The present results on zinc are the first direct mobility measurements reported on a metal in the so-called "soft" group which includes face-centered cubic and hexagonal close-packed metals. The conspicuous difference between basal dislocations in zinc and all the other materials

TABLE VI

Summary of τ_0 and n for Various Materials

Material	Temperature °K	τ_0 lb/in. ²	n
Silicon-Iron (12)	298	30,000	35
Tungsten (16)	298	45,000	4.8
Lithium Fluoride (11)	298	1,400	25
Sodium Chloride (15)	298	210	8
Germanium (13)	693	3.5×10^6	1.5
	973	24,000	1.5
Zinc			
Basal	298	5	5
Nonbasal	298	790	9.5

listed in Table VI is the low value of τ_0 which indicates a much lower lattice resistance to dislocation motion.

E. Lattice Resistance to Dislocation Motion

Two possible sources of lattice resistance to dislocation motion in an otherwise perfect lattice have been considered theoretically. Leibfried (2) was the first to consider the drag on a screw dislocation moving at a constant velocity caused by the scattering of phonons or sound waves and Eshelby (3) has estimated the drag caused by thermoelastic effects. Lothe (33) has recently reviewed and extended the calculations for both effects. Lothe concludes that for metals the thermoelastic effect is negligible and that Leibfried's result for the phonon drag is correct and should be about the same for a edge as well as a screw dislocation. The drag stress due to phonon scatter is given by

$$\tau_d = \frac{1}{10} \epsilon \frac{v}{c}$$

where

ϵ = thermal energy density

v = dislocation velocity

c = velocity of shear waves.

Since zinc at room temperature is above the Debye temperature (250°K)

$$\epsilon = \frac{3KT}{b^3}$$

and

$$\tau_d = \frac{0.3KTv}{b^3c}$$

where for zinc

$$b = 2.66 \times 10^{-8} \text{ cm}$$

$$c = 2.31 \times 10^5 \text{ cm/sec.}$$

The phonon drag stress on a dislocation moving at 25 cm/sec in zinc is calculated to be about 1 lb/in.² which from the present mobility results is a factor of 10 lower than the observed stress required to move a dislocation at this velocity. Seeger (34) has indicated that the damping constant for an edge dislocation should be an order of magnitude greater than that for a screw dislocation which would result in a drag stress of about 10 lb/in.² for a dislocation moving at 25 cm/sec. If this conclusion is correct the present results suggest that the drag stress should vary as the velocity to the $\frac{1}{5}$ power rather than the first power. Considering the uncertainties involved in the theoretical calculations, the possibility that the entire lattice resistance to moving dislocations may be due to phonon scattering cannot be excluded.

F. Nature of Long-Range Internal Stresses

As mentioned above, in Section C, Seeger, Mader and Kronmuller (30) consider the flow stress for zinc in basal slip to be determined by the long-range internal stresses of parallel glide dislocations and a thermally dependent term due to jog formation. The athermal or long-range stress term at room temperature has been shown to account for the major portion of the flow stress (35). All obstacles to dislocation motion which involve internal stress interactions over distances where thermal activation cannot assist in overcoming the obstacle are classed as athermal.

The present results as shown in Fig. 29 indicate that changes in crystal purity can have an appreciable effect on the flow stress with little change in the density of basal dislocations. This result along with the correlation of dislocation density change with shear strain shown in Fig. 33 and Table III for two different purities suggests that the long-range internal shear stress which must be overcome for glide to occur is not due to interaction of parallel glide dislocations.

A possible source of long-range internal stress results when glide dislocations form attractive and repulsive junctions with forest dislocations (31). Saada (36) gives the conditions required for the formation

of attractive and repulsive junctions between two dislocations with Burgers vectors \bar{b}_1 and \bar{b}_2 . If $\bar{b}_1 \cdot \bar{b}_2$ is negative, an attractive junction is formed by the dislocation reaction

$$\bar{b}_1 + \bar{b}_2 \rightarrow \bar{b}_3$$

If $\bar{b}_1 \cdot \bar{b}_2$ is positive, the dislocations repel one another and constitute a repulsive junction. If the scalar product is zero, the reaction is neutral from an energy viewpoint. These vector conditions are equivalent to a statement in terms of energy changes which accompany a dislocation reaction. Namely, a reaction occurs only if the energy per unit length of \bar{b}_3 is less than the sum of energies of \bar{b}_1 and \bar{b}_2 or

$$Gb_3^2 < Gb_1^2 + Gb_2^2 .$$

Saada has calculated the stress required to overcome attractive and repulsive junctions as

$$\tau = \frac{Gb}{\beta l} \quad (17)$$

where

b = Burgers vector (assumed to be the same for both dislocations)

l = distance between attractive or repulsive junctions

$$\beta = 2.5 \text{ (for attractive junctions)}$$
$$10 \text{ (for repulsive junctions).}$$

More detailed calculations have been made by Gale (37)¹⁹ for specific dislocation reactions in FCC and BCC structures where such junction reactions are thought to have a great effect on the flow stress.

The specific dislocation reactions in zinc which are most likely to form attractive and repulsive junctions are reactions between basal dislocations $\bar{b}_1 = \bar{a}$, and nonbasal dislocations with $\bar{b}_2 = (\bar{c} + \bar{a})$. Reactions between \bar{a} and \bar{c} type dislocations are neutral because $(\bar{a} \cdot \bar{c}) = 0$. A $(\bar{c} + \bar{a})$ dislocation is likely because from an energy standpoint this Burgers vector is the next shortest nonbasal one after a \bar{c} type dislocation and because the $(\bar{c} + \bar{a})$ dislocation has been shown by Price (38) to be responsible for nonbasal slip.

Figure 47² shows the \bar{a} and \bar{c} directions in the hexagonal cell. Possible values of \bar{a} are $\pm \bar{a}_1$, $\pm \bar{a}_2$ and $\pm \bar{a}_3$ which together with $\pm \bar{c}$ give a total of 12 possible $(\bar{c} + \bar{a})$ type dislocations. The number of possible reactions involving \bar{a} and $(\bar{c} + \bar{a})$ dislocations is then $6 \times 12 = 72$. Half of these reactions form attractive and half form repulsive junctions.

The effect of attractive and repulsive junctions in the present investigation can be estimated. The density of forest dislocations, as deduced from etch

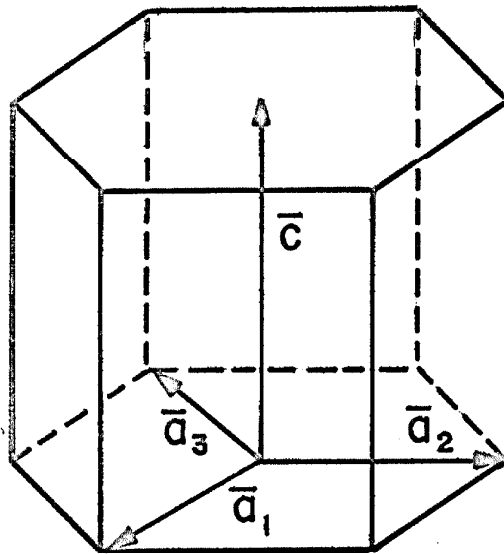


Fig. 47 Possible \bar{c} and \bar{a} Type Vectors.

pit densities on basal planes, is given in Table V for the various purities of zinc. The number of these dislocations with $(\bar{c} + \bar{a})$ type Burgers vectors is not known, but for the sake of a calculation, it will be assumed that 1/2 are dislocations with this type of Burgers vector. Taking the forest density to be about 10^4 cm^{-2} for the 99.999 per cent purity material, the density of $(\bar{c} + \bar{a})$ dislocations is $5 \times 10^3 \text{ cm}^{-2}$ and the density of $(\bar{c} + \bar{a})$ dislocations forming attractive junctions is $2.5 \times 10^3 \text{ cm}^{-2}$. Therefore, the spacing between attractive junctions as well as that between repulsive ones will be $2 \times 10^{-2} \text{ cm}$. The stress to overcome both junctions is given by the stress to overcome attractive junctions, which from Eq. 17 is

$$\tau = \frac{1}{2.5} \frac{Gb}{l}$$

where

$$G = 5.6 \times 10^6 \text{ lb/in.}^2$$

$$b = 4.13 \times 10^{-8} \text{ cm (average of } b_1 \text{ and } b_2)$$

$$l = 2 \times 10^{-2} \text{ cm.}$$

This gives a value of 4.6 lb/in.^2 for the internal stress, τ_i , due to attractive and repulsive junctions which is approximately the lowest stress at which basal dislocations were observed to move long distances

compared to the forest spacing in 99.999 per cent purity crystals. This calculation indicates that the stress required to overcome attractive and repulsive junctions is the correct magnitude to explain the lowest stress at which dislocation pile-ups were observed.

The nature of τ_i caused by attractive and repulsive junctions is such as to cause a resistance to dislocation motion in either direction of motion of the dislocation. This fact may explain why the dislocation pile-ups observed in the relaxation experiment were not observed to relax after unloading from a resolved shear stress of 12.1 lb/in.². Assuming that each dislocation in a pile-up is held in equilibrium under load by a forward applied stress of 12.1 lb/in.² and a reverse stress of 6 lb/in.² due to attractive and repulsive junctions and 6 lb/in.² from other dislocations in the pile-up. When the applied stress is removed the stress from junctions reverses sign and balances that due to the other surrounding dislocations. Additional relaxation tests would have to be conducted at different levels of applied shear stress to confirm this explanation.

Tinder (39) has recently argued in a similar way to explain the closed hysteresis loops obtained in the microstrain region for zinc single crystals. The

closed loops require a friction stress which acts in both directions which would be the case for the junction model for applied stresses below the stress level required to break attractive and repulsive junctions. Tinder found a closed hysteresis loop upon stressing a crystal to 2.25 lb/in.^2 after it had been deformed to a shear stress level of 11.4 lb/in.^2 when the 2.25 lb/in.^2 was applied in the same direction as the pre-load. When a shear stress of 2.25 lb/in.^2 was applied in the reverse direction an open loop was obtained which indicates that the friction stress was overcome. This behavior is entirely consistent with the picture envisioned to explain why pile-ups did not relax upon removal of an applied shear stress of 12.1 lb/in.^2 . According to the model, in the unloaded condition the junctions are stressed to their breaking points in the reverse stress direction so that upon application of a small reverse stress they can be overcome with ease.

The long-range internal stresses provided by attractive and repulsive junctions does not explain why work-hardening occurs once the internal stress is exceeded because the forest density and therefore the junction spacing does not increase during basal slip. Seeger, Mader, Kronmuller and Trauble (40) have concluded from observations of slip line lengths on the

surface of deformed zinc crystals that work-hardening is caused by the long-range internal stresses of dislocation pile-ups. Figures 31 and 32 of the present results illustrate the nature of the basal dislocation distribution in work-hardening specimens. A conspicuous feature of the work-hardened state is the appearance of large numbers of dislocation pile-ups. It is therefore likely that a work-hardening model based on pile-up interactions is appropriate for zinc deformed in basal slip, ~~and that~~ the increase in T_i with strain may be attributed to the stress fields of the pile-ups.

G. Strain-Rate Sensitivity of the Flow Stress

As originally suggested by Guard (9), the dislocation mobility exponent may be deduced from the strain-rate sensitivity of the flow stress providing the number of moving dislocations does not change as a result of the change in strain-rate. The shear strain-rate is related to dislocation motion by

$$\dot{\gamma}_p = \rho_M b v$$

so that

$$\frac{\partial \ln \dot{\gamma}_p}{\partial \ln \tau} = \frac{\partial \ln \rho_M}{\partial \ln \tau} + \frac{\partial \ln v}{\partial \ln \tau} \quad (18)$$

The values for $\frac{\partial \ln \dot{\gamma}_p}{\partial \ln \tau} = n'$ determined for zinc crystals of different purities are given in Table IV.

The average value of n' for two tests on a 99.999 per cent purity crystal is 83. The mobility relation determined by the direct experiments is assumed valid, so that

$$\frac{\partial \ln v}{\partial \ln \tau} = n = 5$$

and

$$\frac{\partial \ln \rho_m}{\partial \ln \tau} = n' - n = 78$$

for 99.999 per cent purity material. This discrepancy between n' and n is large and clearly shows that the number of moving dislocations changes as a result of a strain-rate change.

Similar experiments have been conducted on lithium fluoride (41), silicon-iron (41) and tungsten (16) crystals where the inverse strain-rate sensitivity n' has been found to increase with strain. When the data is extrapolated to zero strain, the resulting n' is very close to the mobility exponent, n . The validity of the strain-rate sensitivity experiment for determining mobility exponents has been argued from these results. However, no explanation for the increase in n' with strain has been proposed. The values of n' as given

in Table IV were not observed to increase with strain except for one test on a zone refined purity specimen where the extrapolated value at zero strain was about 50.

An alternative model to explain the results found for zinc is proposed where the density of moving dislocations, ρ_M , is a function of the difference between the applied shear stress and the flow stress at zero strain-rate, τ_i or

$$\rho_M = A(\delta_p)(\tau - \tau_i)^m.$$

$A(\delta_p)$ is some unknown function of the plastic shear strain and τ_i may be regarded as the long-range internal stress produced by junction reactions and dislocation pile-ups. It would therefore be a function of δ_p , that is $\tau_i = \tau_i(\delta_p)$. The velocity of a moving dislocation is still regarded as a function of τ because the average stress experienced by a moving dislocation is independent of τ_i (the internal stress τ_i must average to zero along a slip plane).

A qualitative picture of the stress difference $\tau - \tau_i$ as a function of distance along a slip plane is given in Fig. 48. Glide dislocations will be prevented from moving when $\tau - \tau_i$ is negative or equal to zero. This condition is shown for several dislocations. A slight increase in the applied stress will shift the

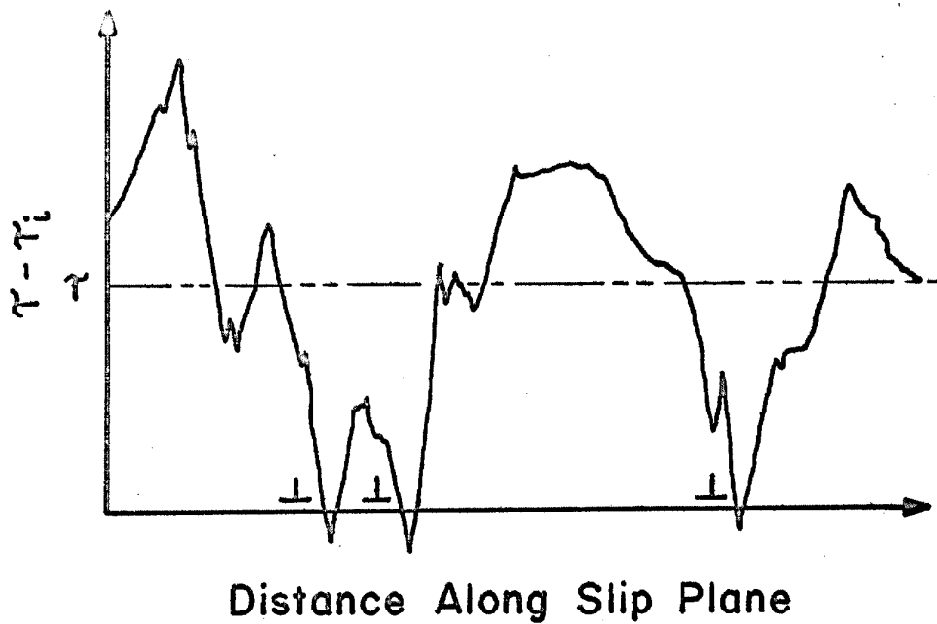


Fig. 48 Variation in Shear Stress Along a Slip Plane.

curve upwards allowing some obstructed dislocations to glide. The specific number of dislocations released in this manner would depend on the details of the internal stress variation and, in particular, the distribution of points where $T - T_i$ goes negative because this stress difference governs whether a dislocation will be released when a given stress change is imposed.

The strain rate is now given as

$$\dot{\gamma}_p = A(\dot{\gamma}_p)(T - T_i)^m \tau^n$$

and

$$\frac{\partial \ln \dot{\gamma}_p}{\partial \ln \tau} = m \frac{\partial \ln (T - T_i)}{\partial \ln \tau} + n$$

or

$$\frac{\partial \ln \dot{\gamma}_p}{\partial \ln (T - T_i)} = m + n \frac{\partial \ln \tau}{\partial \ln (T - T_i)}$$

The experimentally determined values of $\frac{\partial \ln \dot{\gamma}_p}{\partial \ln (T - T_i)} = m'$ are given in Table IV. The term $\frac{\partial \ln \tau}{\partial \ln (T - T_i)}$ is equal to the ratio m'/n' and is determined experimentally. Therefore m is given by

$$m = m' \left(1 - \frac{n}{n'} \right)$$

Since n is much less than n' , $m \approx m'$. Table IV

gives the values of m' determined for the various purity materials. For 99.999 per cent purity $m' = 2$ and is a little less for the other purities. The reason for the low value of 1.1 for the Zn-0.02Al purity is not known. An exponent of $m = 2$ would be expected if the number of dislocations released per unit length of glide plane were a linear function of the stress difference $\tau - \tau_i$.

The model proposed to explain the results for zinc may also apply to other metals of the soft metal group such as copper. Conrad (42) has measured the strain-rate sensitivity of copper single crystals at low temperature and finds that $\frac{\partial \ln \dot{\epsilon}}{\partial \ln \tau} = 100-200$ at 170°K. This result is clearly unreasonable for a mobility exponent. An alternative interpretation of the results in terms of the newly proposed model is suggested. More important, if the density of moving dislocations changes during a strain-rate change, many of the conclusions that Conrad makes regarding thermally activated mechanisms would be completely invalid.

The present model would not be expected to apply to hard type materials such as silicon-iron and lithium fluoride because in these materials the variation of the internal stress τ_i should be much less than the levels of applied stress required to cause dislocation

motion at appreciable velocities. The large value of τ_0 in these materials is responsible for this condition. In such cases the change in moving dislocation density would be small and have little effect on the nominally high mobility exponents.

H. Stress-Strain Behavior

Numerous investigations have been made on the influence of various variables on the basal stress-strain behavior of zinc single crystals. These investigations have included the effects of temperature (28), purity (28, 43), substructure (44) and nonbasal forest dislocation density (23). The present investigation has shown that the nonbasal forest dislocation density and the characteristics of the dislocation substructure are significantly influenced by the impurity level. The effect of cadmium impurity on the degree of impurity segregation and associated dislocation substructure in zinc single crystals has been shown by Damiano and Tint (45). The present observations on segregation and substructure in crystals with aluminum impurity are in essential agreement with the work of Damiano and Tint. Namely, at some impurity levels and under certain growth conditions, impurities may segregate into a cellular structure and a dislocation substructure is associated with the impurity segregation if the degree of segregation

is great enough. [This is probably due to impurity pinning of the dislocations which stabilizes the dislocation substructure. In terms of the mechanical properties of zinc single crystals, the interrelation between impurity changes and changes in dislocation substructure as well as forest densities has not generally been appreciated by previous investigators. An important point is that when the impurity changes are made, the effects on the mechanical properties may be due to resultant changes in forest densities and substructure as well as direct impurity effects. This agrees with Seeger (46) ⁶ who ^{proposed} has estimated that the primary effect of impurity changes on the stress-strain behavior of hexagonal close-packed crystals is through changes in ^{forest} dislocation densities, ~~but the relative importance of forest~~

Figure 29 shows the effect of impurity additions on the stress-strain behavior. The effect of the forest dislocation density on the initial flow stress can be estimated from the dislocation densities given in Table V and by the use of Eq. 17 which gives the stress required to overcome attractive and repulsive junctions. Following the assumptions given above, in Section F, the stress required to overcome junctions in Zn-0.0025Al and Zn-0.02Al crystals is estimated to be 14.0 and 21.2 lb/in.² respectively. The initial flow stress for

crystals of these purities is 27 and 73 lb/in.² as shown in Fig. 29. Thus a large share of the increase in flow stress over that for 99.999 per cent purity crystals can be attributed to changes in the forest density produced by impurity additions.

Impurity additions were noted to have an effect on the character of dislocation substructure as shown in Table V. These changes may have an influence on the measured stress-strain curves because certain dislocation sub-boundaries can have long-range stress fields which must be overcome by the applied stress if dislocations are to glide past the boundaries. The notable difference between the substructure in Zn-0.02Al material as compared to the other purities may account for the large difference between the initial flow stress and the stress to overcome junction reactions in the Zn-0.02Al material. A detailed knowledge of the dislocation character of the substructure would be required to estimate the specific effect of the substructure change on the flow stress.

The effect of prestraining and annealing on the stress-strain behavior is shown in Fig. 30. The stress-strain curves are shifted to higher stresses which is probably due to an increased dislocation substructure density since the density of forest dislocations undoubtedly did not change. Figure 45 shows the effect of

(the critical resolved shear stress for non-basal dislocations is considerably greater than the stresses employed in the basal stress-strain experiments)

prestraining on the substructure density. The present results are consistent with the results of Washburn (44) on the effect of tilt boundaries on the stress-strain behavior of zinc single crystals.

This effect is small compared to the effect of impurity additions.

Nonbasal Slip System

A. Dislocation Orientations and Dislocation Multiplication

The initial stages of nonbasal deformation occur in isolated slip bands as shown in Fig. 38 which shows the result of a c-axis pulse test. This mode of slip deformation is somewhat different than that found for basal slip in that the nonbasal slip bands are broad and not limited to one slip plane. The appearance of the slip bands is similar to those found in deformed single crystals of lithium fluoride (47) where dislocation multiplication has been attributed to a multiple cross-slip mechanism. Multiple cross-slip occurs when a screw dislocation segment in one slip plane glides onto another slip plane which contains the same Burgers vector. Cross-slip will be likely in cases where the screw dislocation is not extended into widely spaced partial dislocations and when a resolved shear stress occurs on the cross-slip plane. When a screw dislocation segment glides onto the cross-slip plane, it is likely to cross-slip once again onto another slip plane parallel to the original slip plane. The screw segments that

lie on the parallel slip plane can then act as a Frank-Read source because the dislocation segments on the cross-slip plane are edge dislocations which cannot glide in the same direction as the screw segment. Figure 49 shows a bowed dislocation segment on a parallel slip plane after cross-slip has occurred.

Price (38) has used electron microscopy to study the nonbasal slip system in zinc. Nonbasal slip was found to occur by the glide of screw dislocations with a $(\bar{c} + \bar{a})$ or $\frac{1}{3} [\bar{1}2\bar{1}3]$ Burgers vector. The slip plane was identified as the $\{11\bar{2}2\}$ or second order pyramidal

plane. However, extensive cross-slip was observed by Price (3) which must have occurred on $\{10\bar{1}1\}$ or first order pyramidal planes because this plane is the only other low index, nonbasal plane that contains the $\bar{c} + \bar{a}$ direction. Figure 50 shows the first and second order pyramidal planes. In addition, Price observed large dipole trails and jogs on screw dislocations and attributed these to cross-slip.

The orientation of the load axis along the c-axis in the present work causes a resolved shear stress in the first order pyramidal plane equal to about 90 per cent of that produced on the second order pyramidal plane. This produces a favorable condition for cross-slip to occur and hence the conclusion is drawn that

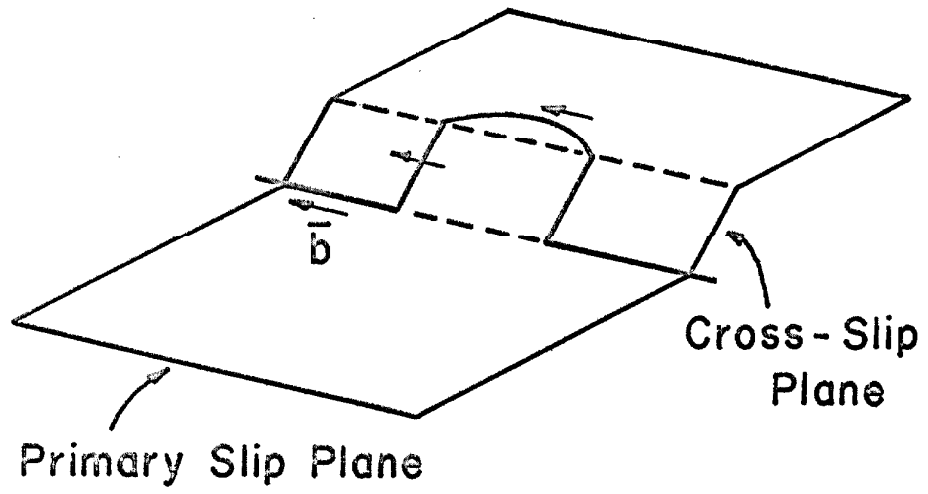
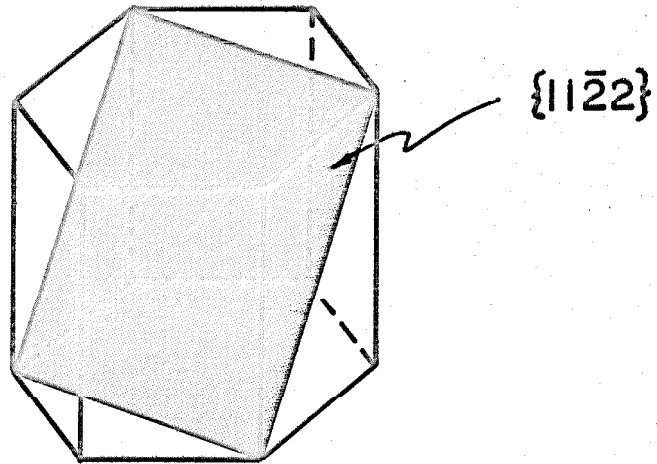
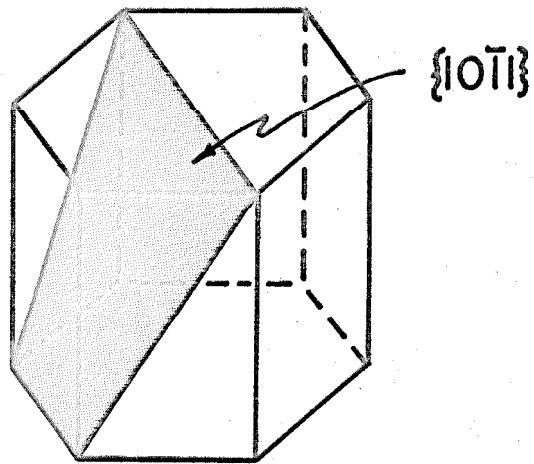


Fig. 49 Cross-Slip Mechanism.



(a) Second Order Pyramidal Plane



(b) First Order Pyramidal Plane

Fig. 50 First and Second Order Pyramid Planes.

multiple cross-slip is responsible for the nature of the observed slip bands.

The dislocations observed in the direct mobility experiment are ^{therefore} most likely close to the edge orientation with a $\frac{1}{3} [\bar{1}2\bar{1}3]$ Burgers vector. ^{two} The slip band traces, ^{most frequently observed} on the specimen prism surfaces correspond to $\{11\bar{2}2\}$ planes which make a normal intersection with the observation surface. Therefore, edge dislocations ^{on these planes} will lie perpendicular to the observation surface and screw dislocations will lie parallel to it. ←

B. Dislocation Mobility

The mobility of dislocations in the nonbasal slip system can be expressed in the form

$$v = \left(\frac{\tau}{\tau_0} \right)^n$$

where $n = 9.5$ and $\tau_0 = 790 \text{ lb/in.}^2$ from Fig. 39.

These parameters are tabulated in Table VI where they may be compared to those of other materials. Nonbasal dislocations are clearly less mobile than basal dislocations so that the mobility limiting process must not involve phonon scatter. In addition, nonbasal dislocation mobility cannot be classed with the "hard" group of body-centered cubic and diamond cubic crystals in terms of mobility. Therefore, the rate-limiting process is probably not the thermal activation of

dislocation kinks over a strong Peierls barrier which has been used to explain results in lithium fluoride (5) and germanium(48). Models based on a Peierls barrier predict that the mobility should depend on the applied stress as

$$v \propto e^{-\frac{A}{\tau}}. \quad (19)$$

Mobility data on silicon-iron (12), lithium fluoride (11) and germanium (14) have been found to satisfy this relation. The data on nonbasal mobility in zinc does not fit Eq. 19 and thus a Peierls barrier mechanism can be considered unlikely.

Models based on thermally activated events such as jog formation and thermally activated cross-slip (31) should give a mobility relation of the form

$$v \propto e^{\frac{\tau - \tau_i}{B}}$$

where τ_i is the long-range internal stress. The non-basal mobility data does not fit this form using $\tau_i = 0$ and a poor correlation is obtained by using values for τ_i greater than zero. Therefore, none of the theoretical mechanisms considered are appropriate to the present results and additional experiments over a more extended stress range and at different temperatures are suggested to better define the physical mechanism which limits the nonbasal dislocation mobility.

C. Strain-Rate Sensitivity of the Flow Stress

The dislocation mobility exponent as deduced from the variable strain-rate test is listed in Table IV as 720 ± 10 . The fact that this value is significantly above the directly measured exponent of 9.5 indicates that the assumption of a constant density of moving dislocations during a rapid change in strain-rate is incorrect. This conclusion must be correct even though the dislocation velocities measured directly were of the leading dislocations in a slip band and thus represented the maximum velocities, whereas the variable strain-rate test depends on average velocities in a specimen covered by intersecting slip bands like those seen in Fig. 28. An analysis of the strain-rate data in terms of a difference between the applied stress and the flow stress at zero strain-rate was not possible because of the very low strain-rate sensitivity. Therefore, the model proposed to describe the change in density of moving dislocations for the basal data could not be applied to the nonbasal data. However, there is some likelihood that the same model would be appropriate to the nonbasal slip system and, if so, this would explain the high value of the inverse strain-rate sensitivity in terms of the change in density of moving dislocations.

Stress-Strain Behavior as Related to Dislocation Properties

Basal slip in zinc single crystals occurs at low stresses and involves the motion of relatively small numbers of very mobile dislocations. The initial flow stress appears to be determined by the stress required to overcome attractive and repulsive junctions between basal and nonbasal dislocations. Once the initial flow stress has been exceeded, work-hardening occurs at a very low rate because the density of nonbasal dislocations does not increase and because the mobility of basal dislocations is high enough to allow many of them to leave the crystal which prevents them from contributing to work-hardening through interactions with other parallel glide dislocations. Dislocation pile-ups occur and their interactions probably determine the observed work-hardening rates.

As opposed to basal deformation, nonbasal slip involves the movement of relatively large numbers of slowly moving dislocations. Dislocations appear to multiply by a multiple cross-slip mechanism which produces slip bands. The high work-hardening rates observed for nonbasal slip are caused by dislocation pile-up interactions within individual slip bands and by the interaction of slip bands on the six equivalent slip planes which results in an increase in the density of forest dislocations with increasing strain.

VII. SUMMARY AND CONCLUSIONS

The mobility of basal dislocations in zinc single crystals of 99.999 per cent purity has been experimentally determined from observations of dislocation pile-up lengths produced by load pulse tests. The results obey the relation $v = \left(\frac{\tau}{\tau_0}\right)^n$ for $\tau \geq 6$ lb/in.², where v is the dislocation velocity in cm/sec, n is the mobility exponent and is equal to 5, and τ_0 is 5 lb/in.². The maximum velocities observed are in the range of 7 to 80 cm/sec for shear stresses between 7 and 12 lb/in.². The results are inconsistent with the predictions using theoretical models which involve the thermally activated motion of a glide dislocation past forest dislocations or impurity atoms. The drag stress on a moving dislocation caused by phonon scattering is ^{considered} found to be the most likely velocity limiting process. The minimum shear stress required to cause dislocation pile-ups is about 6 lb/in.² and this stress is shown to correspond to the stress to break attractive junctions between basal and nonbasal dislocations. Thus plastic flow in the basal slip system occurs when attractive junctions are overcome.

The strain-rate sensitivity of the flow stress for basal slip has been determined for zone refined, 99.999 per cent, Zn-0.0025Al and Zn-0.02Al specimens. A large

*The mobility of
of basal dislocation
and edge dislocation
dislocations of zinc
to be the same.*

difference is observed between the inverse strain-rate sensitivity and the directly determined mobility exponent. A dislocation model is proposed which explains the observed differences. The major part of the strain-rate sensitivity is attributed to changes in the number of moving dislocations which accommodate a change in strain-rate, rather than to the change of dislocation velocity. The model proposed for basal slip in zinc may also apply to ^{"soft" hexagonal compounds and face centered} [nonbasal slip in zinc and to copper and aluminum] crystals deformed in easy glide, in which large strain-rate changes may be made with very small changes in stress.

The mobility of dislocations in the $\langle 1\bar{2}1\bar{3} \rangle \{1\bar{2}12\}$ nonbasal slip system has been experimentally determined from measurements of the length of slip bands produced by pulse load tests. The results obey the relation $v = \left(\frac{\tau}{\tau_0} \right)^n$ where $n = 9.5$ and $\tau_0 = 790 \text{ lb/in.}^2$. Velocities between 2×10^{-4} and 2 cm/sec were measured in the stress range from 300 to 800 lb/in.^2 . The results are inconsistent with theoretical models which involve thermally activated events. The appearance of the nonbasal slip bands suggests that dislocation multiplication takes place by a double cross-slip mechanism in which segments of screw dislocations with $\bar{c} + \bar{a}$ Burgers vectors glide from second order pyramidal planes onto

first order pyramidal planes and then back onto another second order pyramidal plane.

The addition of 0.0025 and 0.02 per cent aluminum to zinc produces a segregation substructure, and increases the density of nonbasal dislocations. The raise of the basal shear stress vs. shear strain curve, which is observed to accompany the addition of aluminum, is attributed primarily to this increase in the density of nonbasal dislocations. The increased density of nonbasal dislocations produces an increase in the density of attractive junctions between basal and nonbasal dislocations. Hence, the stress required to move basal dislocations is increased.

The change in basal dislocation density, $\Delta\rho$, produced by plastic shear strain, $\delta\rho$, obeys the relation $\Delta\rho = C \delta\rho^{\frac{1}{3}}$ where C is a constant, and is independent of purity. This relation is different from the relations that have been reported for copper, silver, and lithium fluoride single crystals. The difference may be explained by the long glide distances observed for basal dislocations in zinc crystals. Glide distances of the order of the specimen size have been observed which indicates that large numbers of dislocations may glide out of the specimen and hence produce strain but do not contribute to etch pit densities.

The important results and conclusions of this investigation are:

1. The mobility of dislocations in the basal and nonbasal slip systems has been determined experimentally and the results have been evaluated in terms of current theories. The drag stress caused by phonon scattering is shown to be the most likely velocity limiting process for basal dislocations. No theory has been found which predicts the mobility relation for nonbasal dislocations.
2. The strain-rate sensitivity of the flow stress has been determined for zinc single crystals deformed in basal slip. The inverse strain-rate sensitivity differs greatly from the mobility exponent and a dislocation model is proposed to explain the difference. The model attributes the strain-rate sensitivity to changes in the number of moving dislocations. The importance of changes in the density of moving dislocations accompanying a strain-rate change has not generally been recognized by previous investigators. The model proposed may also apply to nonbasal slip in zinc and

to copper and aluminum crystals deformed in easy glide.

3. The long-range internal stress which must be overcome for basal slip to occur is attributed to attractive junctions between basal and non-basal dislocations. This source of internal stress is shown to be consistent with the following observations: (1) the stress required to cause dislocation pile-ups; (2) the effect of aluminum impurity on nonbasal dislocation densities and on the basal stress-strain behavior; and (3) dislocation pile-ups do not relax with the removal of applied stress. The importance of attractive junctions in relation to basal slip of hexagonal close-packed crystals has generally not been recognized by previous investigators.
4. The influence of aluminum impurity on the basal stress-strain behavior is due in large part to changes in the density of nonbasal dislocations which determine the spacing of attractive junctions.
5. The change in basal dislocation density with shear strain is given by the relation $\Delta\rho = C\gamma_p^{\frac{1}{3}}$ and is independent of purity. This relation

is different from the relations that have been reported for copper, silver and lithium fluoride single crystals. The difference is attributed to the long glide distances observed for basal dislocations in zinc.

REFERENCES

1. L. J. Teutonico, "Moving Edge Dislocations in Cubic and Hexagonal Materials," Physical Review (1962), Vol. 125, pp.1530-1533.
2. G. Leibfried, "Über den Einflub thermisch angeregter Schallwellen auf die plastische Deformation," Zeitschrift fur Physik (1950), Vol. 127, pp. 344-356.
3. J. D. Eshelby, "Dislocations as a Cause of Mechanical Damping in Metals," Proceedings of the Royal Society of London (1949), Vol. 197A, pp. 396-416.
4. J. Friedel, Dislocations (1964), Pergamon Press, London, p. 381.
5. J. J. Gilman, "The Plastic Resistance of Crystals," Australian Journal of Physics (1960), Vol. 13, pp. 327-346.
6. A. Seeger, "The Temperature Dependence of the Critical Shear Stress and of Work-hardening of Metal Crystals," The Philosophical Magazine (1954), Vol. 45, Seventh Series, pp. 771-773.
7. G. S. Baker, "Dislocation Mobility and Damping in Lithium Fluoride," Journal of Applied Physics (1962), Vol. 33, pp. 1730-1732.
8. K. R. King, "Dynamic Shear Deformation in Zinc Crystals," Ph.D. Thesis, California Institute of Technology, 1962.
9. R. W. Guard, "Rate Sensitivity and Dislocation Velocity in Silicon Iron," Acta Metallurgica (1961), Vol. 9, pp. 163-165.
10. A. Granato and K. Lucke, "Application of Dislocation Theory to Internal Friction Phenomena at High Frequencies," Journal of Applied Physics (1956), Vol. 27, pp. 789-805.
11. W. G. Johnston and J. J. Gilman, "Dislocation Velocities, Dislocation Densities, and Plastic Flow in Lithium Fluoride Crystals," Journal of Applied Physics (1959), Vol. 30, pp. 129-144.

12. D. F. Stein and J. R. Low, Jr., "Mobility of Edge Dislocations in Silicon-Iron Crystals," Journal of Applied Physics (1960), Vol. 31, pp. 362-369.
13. A. R. Chaudhuri, J. R. Patel, and L. G. Rubin, "Velocities and Densities of Dislocations in Germanium and Other Semiconductor Crystals," Journal of Applied Physics (1962), Vol. 33, pp. 2736-2746.
14. M. N. Kabler, "Dislocation Mobility in Germanium," Physical Review (1963), Vol. 131, pp. 54-58.
15. E. Yu. Gutmanas, E. M. Nadgornyi, and A. V. Stepanov, "Dislocation Movement in Sodium Chloride Crystals," Fizika Tverdogo Tela (1963), Vol. 5, pp. 1021-1026.
16. H. W. Schadler, "Mobility of Edge Dislocations on {110} Planes in Tungsten Single Crystals," Acta Metallurgica (1964), Vol. 12, pp. 861-870.
17. H. S. Rosenbaum, "Non-Basal Slip and Twin Accommodation in Zinc Crystals," Acta Metallurgica (1961), Vol. 9, pp. 742-748.
18. R. L. Bell and R. W. Cahn, "The Dynamics of Twinning and the Interrelation of Slip and Twinning in Zinc Crystals," Proceedings of the Royal Society of London (1957), Vol. 239A, pp. 494-521.
19. J. J. Gilman, "Etch Pits and Dislocations in Zinc Monocrystals," Transactions of the American Institute of Mining, Metallurgical and Petroleum Engineers (1956), Vol. 206, pp. 998-1004.
20. H. S. Rosenbaum and M. M. Saffren, "Dislocation Etch Pits on the Basal Plane of Zinc Crystals," Journal of Applied Physics (1961), Vol. 32, pp. 1866-1872.
21. R. C. Brandt, K. H. Adams, and T. Vreeland, Jr., "Etching of High Purity Zinc," Journal of Applied Physics (1963), Vol. 34, pp. 587-590.
22. R. C. Brandt, K. H. Adams, and T. Vreeland, Jr., "Dislocations and Etch Figures in High Purity Zinc," Journal of Applied Physics (1963), Vol. 34, pp. 591-594.
23. E. J. Stofel, "Plastic Flow and Fracture of Zinc Single Crystals," Ph.D. Thesis, California Institute of Technology, 1962.

17 of
this one
0.2
34

24. T. L. Russell, D. S. Wood and D. S. Clark, First Interim Technical Report under Office of Ordnance Research, Contract No. DA-04-495-ORD-171, California Institute of Technology, 1955.
25. J. R. Low, Jr., and R. W. Guard, "The Dislocation Structure of Slip Bands in Iron," Acta Metallurgica (1959), Vol. 7, pp. 171-179.
26. M. J. Horden, "Dislocation Density and Flow Stress of Copper," Acta Metallurgica (1962), Vol. 10, pp. 999-1007.
27. H. J. Levinstein and W. H. Robinson, "Dislocation Configurations in Deformed Silver Single Crystals," The Relation between the Structure and Mechanical Properties of Metals (1963), Her Majesty's Stationary Office, London, pp. 180-203.
28. N. F. Mott, "A Theory of Work-hardening of Metal Crystals," The Philosophical Magazine (1952), Vol. 43, Seventh Series, pp. 1151-1178.
29. G. Schoeck, "Correlation Between Dislocation Length and Density," Journal of Applied Physics (1962), Vol. 33, pp. 1745-1747.
30. A. Seeger, S. Mader and H. Kronmuller, "Theory of Work-Hardening of FCC and HCP Single Crystals," Electron Microscopy and Strength of Crystals (Editors: G. Thomas and J. Washburn) (1963), Interscience, New York, pp. 665-712.
31. J. Friedel, "On the Elastic Limit of Crystals," Electron Microscopy and Strength of Crystals (Editors: G. Thomas and J. Washburn) (1963), Interscience, New York, pp. 605-648.
32. J. Friedel, "Dislocation Interactions and Internal Strains," Internal Stresses and Fatigue in Metals (Editors: G. M. Rassweiler and W. L. Grube) (1959), Elsevier, New York, pp. 220-262.
33. J. Lothe, "Theory of Dislocation Mobility in Pure Slip," Journal of Applied Physics (1962), Vol. 33, pp. 2116-2125.
34. A. Seeger, Dislocations and Mechanical Properties of Crystals (Editors: Fisher, Johnston, Thomson and Vreeland) (1957), J. Wiley and Sons, Inc., New York, footnote p. 447.

35. A. Seeger and H. Trauble, "Die plastische Verformung von Zinkeinkristallen," Zeitschrift für Metallkunde (1960), Vol. 51, pp. 435-456.
36. G. Saada, "Dislocation Interactions and Plastic Deformation of Crystals," Electron Microscopy and Strength of Crystals (Editors: G. Thomas and J. Washburn) (1963), Interscience, New York, pp. 651-662.
37. B. Gale, "An Analysis of Some Attractive Dislocation Junctions in Metals," The Relation between the Structure and Mechanical Properties of Metals (1963), Her Majesty's Stationary Office, London, pp. 99-117.
38. P. B. Price, "Pyramidal Glide and the Formation and Climb of Dislocation Loops in Nearly Perfect Zinc Crystals," The Philosophical Magazine (1960), Vol. 5, Eighth Series, pp. 873-886.
39. R. F. Tinder, "On the Initial Plastic Behavior of Zinc Single Crystals," Acta Metallurgica (1965), Vol. 13, pp. 136-139.
40. A. Seeger, H. Kronmüller, S. Mader and H. Trauble, "Work-hardening of Hexagonal Close-packed Crystals and in the Easy Glide Region of Face-centered Cubic Crystals," The Philosophical Magazine (1961), Vol. 6, Eighth Series, pp. 639-655.
41. W. G. Johnston and D. T. Stein, "Stress Dependence of Dislocation Velocity Inferred from Strain Rate Sensitivity," Acta Metallurgica (1963), Vol. 11, pp. 317-318.
42. H. Conrad, "An Investigation of the Rate Controlling Mechanism for Plastic Flow of Copper Crystals at 90° and 170°K," Acta Metallurgica (1958), Vol. 6, pp. 339-350.
43. H. P. Stuwe, "Creep in Zinc Single Crystals at the Temperature of Liquid Nitrogen," Journal of Applied Physics (1959), Vol. 30, pp. 450-451.
44. J. Washburn, "Effect of the Structure of Dislocation Boundaries on Yield Strength," Journal of Metals (1955), Vol. 7, pp. 675-681.

45. V. V. Damiano and G. S. Tint, "Dislocations and Impurity Boundaries in Zinc Crystals Grown from the Melt," Acta Metallurgica (1961), Vol. 9, pp. 177-183.
46. A. Seeger, "The Mechanism of Glide and Work Hardening in Face-Centered Cubic and Hexagonal Close-Packed Metals," Dislocations and Mechanical Properties of Crystals (Editors: Fisher, Johnston, Thomson and Vreeland) (1957), J. Wiley and Sons, Inc., New York, pp. 243-329.
47. W. G. Johnston and J. J. Gilman, "Dislocation Multiplication in Lithium Fluoride Crystals," Journal of Applied Physics (1960), Vol. 31, pp. 632-643.
48. V. Celli, M. Kabler, T. Ninomiya and R. Thomson, "Theory of Dislocation Mobility in Semiconductors," Physical Review (1963), Vol. 131, pp. 58-72.